

Viral-templated Palladium Nanocatalysts

A thesis

submitted by

Cuixian Yang

In partial fulfillment of the requirements

for the degree of

Doctor of Philosophy

in

Chemical Engineering

TUFTS UNIVERSITY

(February, 2013)

Dissertation Committee

Prof. Hyunmin Yi, Chair

Prof. Jerry Meldon

Prof. Maria Flytzani-Stephanopoulos

Prof. Terry Haas

Dr. Byeongdu Lee

ABSTRACT

Despite recent progress on nanocatalysis, there exist several critical challenges in simple and readily controllable nanocatalyst synthesis including the unpredictable particle growth, deactivation of catalytic activity, cumbersome catalyst recovery and lack of in-situ reaction monitoring. In this dissertation, two novel approaches are presented for the fabrication of viral-templated palladium (Pd) nanocatalysts, and their catalytic activities for dichromate reduction reaction and Suzuki Coupling Reaction were thoroughly studied.

In the first approach, viral template based bottom-up assembly is employed for the Pd nanocatalyst synthesis in a chip-based format. Specifically, genetically displayed cysteine residues on each coat protein of Tobacco Mosaic Virus (TMV) templates provide precisely spaced thiol functionalities for readily controllable surface assembly and enhanced formation of catalytically active Pd nanoparticles. Catalysts with the chip-based format allow for simple separation and in-situ monitoring of the reaction extent. Examination of synthesis-structure-activity relationship of Pd nanoparticles formed on surface-assembled viral templates shows that the synthesis conditions of viral-templated Pd nanocatalysts have effect on the Pd nanoparticle size, catalyst loading density and the catalytic activity for dichromate reduction. The viral-templated Pd nanocatalysts with optimized synthesis conditions are shown to have higher catalytic activity per unit

Pd mass than the commercial Pd/C catalysts for dichromate reduction. Furthermore, tunable and selective surface assembly of TMV biotemplates is exploited to control the loading density and location of Pd nanocatalysts on solid substrates via preferential electroless deposition.

In addition, the catalytic activities of surface-assembled TMV-templated Pd nanocatalysts were also investigated for the ligand-free Suzuki Coupling reaction under mild reaction conditions. The chip-based format enables simple catalyst separation and reuse as well as facile product recovery. Reaction condition studies show that the solvent ratio played an important role in the selectivity of the Suzuki reaction, and that a higher water/acetonitrile ratio significantly facilitated the cross-coupling pathway. Meanwhile, in-depth characterizations including Atomic Force Microscopy (AFM), Grazing Incidence Small Angle X-ray Scattering (GISAXS), Inductively Coupled Plasma Optical Emission Spectrometry (ICP-OES) and X-ray Photoelectron Spectroscopy (XPS) were carried out for these chip-based viral-templated Pd nanocatalysts.

In the second approach, catalytically active TMV-templated Pd nanoparticles are encapsulated in readily exploited polymeric microparticle formats. Specifically, small (1~2 nm), uniform and highly crystalline palladium (Pd) nanoparticles are spontaneously formed along (TMV) biotemplates without external reducing agents. The as-prepared Pd-TMV complexes are integrated into the hybrid poly(ethylene glycol)(PEG)-based microparticles via replica molding (RM)

technique in a simple, robust and highly reproducible manner. The Pd-TMV complex structure was characterized by Transmission Electron Microscopy (TEM). The hybrid Pd-TMV-PEG microparticles are examined to have high catalytic activity, recyclability and stability through dichromate reduction. Combined these findings represent a significant step toward simple, robust, scalable synthesis and fabrication of efficient biotemplate-supported Pd nanocatalysts in readily deployable polymeric formats with high capacity in a well-controlled manner. These two simple, robust and readily controllable approaches for the fabrication of viral-templated Pd nanocatalysts, in both chip-based and hydrogel-encapsulated formats, can be readily extended to a variety of other nano-bio hybrid material synthesis in other catalytic reaction systems.

ACKNOWLEDGMENTS

Throughout this endeavor, I have been surrounded by special mentors, colleagues, friends, and family, who have provided inspiration, support, and guidance to make this work possible. I would like to first acknowledge my dissertation adviser, Professor Hyunmin Yi, for continuous encouragement, patience, and motivation. I would also like to acknowledge my dissertation committee members, Professor Maria Flytzani-Stephanopoulos, Professor Jerry Meldon, Professor Terry Haas, and Dr. Byeongdu Lee, for constructive criticism and guidance. I am grateful for the support of the Yi lab members, especially Amy Manocchi, Christina Lewis, Sukwon Jung, and Jaehun Lee. I would also like to acknowledge all of my family and in-laws, most importantly, my husband, Haoran Zhang, who has provided constant encouragement and demonstrated everlasting patience throughout this entire journey. Finally, I would like to acknowledge my son William Y. Zhang, for offering a new perspective in the last year of this work.

I also gratefully acknowledge financial support by the Stanley Charm Fellowship (C.Y.). Partial funding for this work was also provided by the Wittich Family Fund for Sustainable Energy and by the National Science Foundation under Grant No. CBET-0941538. GISAXS work at Argonne National Laboratory was supported by the US Department of Energy, BES-Chemical Sciences and BES-

Scientific User Facilities under Contract DE-AC-02-06CH11357 with UChicago
Argonne, LLC, operator of Argonne National Laboratory.

TABLE OF CONTENTS

ABSTRACT.....	ii
1. Introduction.....	1
1.1. Palladium Nanocatalysts	4
1.1.1. Synthesis of Palladium Nanocatalysts	7
1.1.2. Removal of Hexavalent Chromium	11
1.1.3. Suzuki Cross-coupling Reaction.....	13
1.2. Hydrogel Microparticles	17
1.2.1. Radical Chain Photopolymerization	17
1.2.2. Applications of Hydrogels in Catalysis	19
1.2.3. Replica Molding (RM) Technique.....	22
1.3. Viral-based Nanomaterial Synthesis	24
1.3.1. Icosahedral Viruses	26
1.3.2. Filamentous Viruses.....	28
1.3.3. Rod-Shaped Viruses — Tobacco Mosaic Virus (TMV)	31
1.4. Viral Template-based Nanocatalysts	38
2. TMV-templated Pd Nanocatalysts for Dichromate Reduction.....	41
2.1. Introduction.....	41
2.2. Materials and Methods.....	47
2.2.1. Materials	47
2.2.2. Synthesis of TMV-templated Pd Nanocatalysts	47
2.2.3. Catalytic Activity for Dichromate Reduction	49

2.2.4. Characterization of Pd Nanoparticles	52
2.3. Catalytic Activity and Control Study.....	54
2.4. Recycle Studies for Pd-TMV Chip and Pd Chip	58
2.5. Grazing Incidence Small-Angle X-ray Scattering (GISAXS)	61
2.6. X-ray Photoelectron Spectroscopy	65
2.7. Conclusions.....	69
3. Investigation on the Catalytic Reduction Kinetics of Hexavalent Chromium by Viral-templated Palladium Nanocatalysts.....	71
3.1. Introduction.....	71
3.2. Materials and Methods.....	72
3.2.1. Materials	72
3.2.2. Synthesis of TMV-templated Pd Catalysts	72
3.2.3. Comparison with Commercial Pd/C Catalysts	73
3.2.4. Effect of Catalyst Synthesis Conditions on the Catalytic Activity	74
3.2.5. Grazing Incidence Small Angle X-ray Scattering (GISAXS)	76
3.2.6. Inductively Coupled Plasma Optical Emission Spectrometry (ICP-OES)	76
3.2.7. Kinetics Modeling.....	76
3.3. Chip Removal Study: Heterogeneous Surface Reaction	81
3.4. Kinetics Modeling.....	82
3.5. Comparison with Commercial 5% Pd/C Catalysts	88
3.7. Effect of Synthesis Conditions on the Particle Size and Surface Loading	93
3.8. AFM and GISAXS Study of Viral-templated Pd Nanoparticles	96
3.9. Effect of Synthesis Conditions on the Catalytic Activity	100

3.10. Recyclability of Pd-TMV Chips	105
3.11. Conclusions.....	109
4. Facile Approaches to Control Catalyst Loading Density and Location by Tunable and Selective TMV Surface Assembly.....	110
4.1. Introduction.....	110
4.2. Materials and Methods.....	113
4.2.1. Materials	113
4.2.2. Methods.....	113
4.3. Control of Catalyst Loading Density and Reaction Rate by Tunable TMV Surface Assembly	115
4.3.1. Characterization of Pd-TMV Complex Surface Density by AFM ...	115
4.3.2. Dichromate Reduction Catalyzed by Chips with Different Pd-TMV Density	116
4.3.3. X-ray Photoelectron Spectroscopy Analysis	120
4.4. Control of Catalyst Location and Reaction Rate by Selective TMV Surface Assembly.....	123
4.4.1. Selective Assembly of TMV on Gold-patterned Chips	123
4.4.2. Dichromate Reduction Catalyzed by Gold-patterned Chips.....	126
4.5. Conclusions.....	129
5. TMV-templated Pd Nanocatalysts for Suzuki Coupling Reaction	131
5.1. Introduction.....	131
5.2. Materials and Methods.....	134
5.2.1. Materials	134
5.2.2. Synthesis of TMV-templated Pd Catalysts	134
5.2.3. Suzuki Reaction Studies	135

5.2.4. High-Performance Liquid Chromatography (HPLC) Analysis	136
5.2.5. Catalyst Characterization	136
5.3. Effect of Solvent Ratio on Reaction Selectivity	137
5.4. Surface Characterization by GISAXS	142
5.5. Batch Reaction Profile	145
5.6. Effect of Reactant Ratio on the Reaction Conversion	147
5.7. Reusability of Pd-TMV Catalysts.....	150
5.8. Catalytic Suzuki Reaction of Other Aryl Halides with Phenylboronic Acid	151
5.9. Preliminary Study of the Reaction Mechanism via Chip Removal during Reactions.....	153
5.10. Conclusions.....	157
6. Integration of Catalytically Active Viral-Palladium Nanostructures into Polymeric Hydrogel Microparticles via Replica Molding.....	159
6.1. Introduction.....	159
6.2. Materials and Methods.....	165
6.2.1. Materials	165
6.2.2. Spontaneous Formation of Pd Nanoparticles on TMV Biotemplates and Preparticle Solution Preparation	165
6.2.3. Fabrication of Pd-TMV-PEG Microparticles via Replica Molding	
167	
6.2.4. High-resolution Transmission Electron Microscopy (HRTEM) Characterization	169
6.2.5. Imaging Analysis	169
6.2.6. Inductively Coupled Plasma Atomic Emission Spectroscopy (ICP-OES) 169	

6.2.7. Catalytic Activity Examination of Pd-TMV-PEG Microparticles	170
6.3. Spontaneous Formation of Palladium Nanoparticles along TMV Biotemplates	171
6.4. TEM Characterization.....	174
6.5. Fabrication of Hybrid Hydrogel Microparticles with Encapsulated Pd-TMV Complexes via Replica Molding.....	184
6.6. Catalytic Activity Examination.....	188
6.7. Recyclability and Stability of Pd-TMV-PEG Microparticles	195
6.8. Conclusions.....	198
7. Conclusions and Future Prospects	200
APPENDIX.....	204
A1. Derivation of Kinetics Model	204
A1.1. Step (1) is the Rate Determining Step (RDS)	205
A1.2. Step (2) is the Rate Determining Step (RDS)	207
A1.3. Step (3) is the Rate Determining Step (RDS)	208
A1.4. Step (4) is the Rate Determining Step (RDS)	213
A1.5. Step (5) is the Rate Determining Step (RDS)	215
A1.6. Step (6) is the Rate Determining Step (RDS)	216
A2. The Calibration Curve of Potassium Dichromate	217
A3. The Effect of Stirring Speed on the Dichromate Reduction Rate.....	219

LIST OF FIGURES

Figure 1.1. Equilibria of Aqueous Pd Chloride Complexes ³⁵	9
Figure 1.2. The Typical Pd Catalytic Cycle of Suzuki Reaction ⁶⁸	14
Figure 1.3. General Reaction Mechanism for Photoinitiated Radical Chain Polymerization ⁷⁹	18
Figure 1.4. Replica Molding and Solvent-Assisted Micromolding	23
Figure 1.5. Structures of a Selection of Viruses used for Nanotechnology	25
Figure 1.6. Schematic Diagram of the M13 Structure	28
Figure 1.7. Different Forms of TMV Coat Protein ¹²⁹	32
Figure 2.1. Schematic Diagram of TMV-templated Pd Nanocatalysts for Dichromate Reduction.	46
Figure 2.2. Dichromate Reduction Reaction by Pd-TMV Chips and Control Studies.....	57
Figure 2.3. Recyclability Study	59
Figure 2.4. Particle Size and Distribution Analysis by GI-SAXS.	62
Figure 2.5. XPS Analysis of Gold Chip, TMV Chip and Pd-TMV Chips before and after Reaction	67
Figure 3.1. Surface Reaction Confirmation by Simple Chip Removal Study	81
Figure 3.2. Langmuir-Hinshelwood Kinetics of Dichromate Reduction.....	84
Figure 3.3. Comparison of Predicted [A] with the Experimental [A] over the Time Course	86

Figure 3.4. TEM Images of Commercial 5% Pd/C Catalysts	90
Figure 3.5. Pd Particle Size Distribution of Commercial 5%Pd/C Catalyst	90
Figure 3.6. The Activation Energy of Pd-TMV Chip and Pd/C Catalysts	92
Figure 3.7. Effect of Catalyst Synthesis Conditions on Catalyst Properties.....	94
Figure 3.8. AFM Images of Pd-TMV Chips.....	97
Figure 3.9. GISAXS Study of TMV-templated Pd Nanoparticles.....	98
Figure 3.10. Catalytic Activity (based on the surface area) vs. Pd Nanoparticle Size and Loading Density of TMV-templated Pd Nanocatalysts.	104
Figure 3.11. Recyclability Study of TMV-templated Pd Nanocatalysts	105
Figure 3.12. X-ray Photoelectron Spectroscopy	108
Figure 4.1. Two Facile Approaches for the Control of Pd Loading Density and Location	111
Figure 4.2. AFM Images of TMV Surface Assembly	117
Figure 4.3. Controlled Catalytic Activity of Pd-TMV Chips for Dichromate Reduction	118
Figure 4.4. High Resolution XPS Spectra from Pd-TMV Chips Prepared with Different TMV Concentrations.....	122
Figure 4.5. Selective TMV Surface Assembly and Pd Nanoparticle Formation	124
Figure 4.6. Dichromate Reduction Catalyzed by Gold-patterned Chips	128
Figure 5.1. Pd-TMV Nanocatalyst Catalyzed Suzuki Reaction	133
Figure 5.2. The Effect of Solvent Ratio on Reaction Selectivity and Surface Characterization by AFM	138

Figure 5.3. Pd Particle Size Distribution of Pd-TMV Catalyst Examined by GISAXS	144
Figure 5.4. Concentration of Reactants and Products vs. Reaction Time.....	146
Figure 5.5. Effect of Reactants Ratios on Product Yields	149
Figure 5.6. Recycling Test of Pd-TMV Chip Catalyzed Suzuki Reaction of Iodoanisole with Phenylboronic Acid.....	151
Figure 5.7. Mechanism Investigation of Suzuki Reaction	154
Figure 6.1. Synthesis of Pd-TMV Encapsulated PEG Microparticles by Replica Molding(RM).....	162
Figure 6.2. Spontaneous Pd Nanoparticle Formation on TMV Biotemplates	172
Figure 6.3. TEM Images of Pd Nanoparticles Spontaneously Formed along TMV Biotemplates	176
Figure 6.4. TEM Images of Pd Nanoparticles Spontaneously Formed along TMV Biotemplates under Various Synthesis Conditions.....	177
Figure 6.5. Pd Nanoparticle Size Distribution of Samples Prepared with Various Synthesis Conditions.....	179
Figure 6.6. Effect of Incubation Time on the Pd Formation on TMV	180
Figure 6.7. Effect of Incubation Temperature on the Pd Formation on TMV	180
Figure 6.8. Microphotographs of Pd-TMV-PEG Microparticles.....	184
Figure 6.9. Effect of PEGDA% (v/v) on Particle Fabrication	186
Figure 6.10. Effects of Photoinitiator (PI) Concentration on Particle Fabrication	186

Figure 6.11. Scanning Electron Microscope (SEM) of critical point dried Pd-TMV-PEGDA microparticles	187
Figure 6.12. Catalytic Activities of Pd-TMV-PEG Microparticles Encapsulating various Amounts of Pd-TMV Complexes	189
Figure 6.13. Effect of PEGDA% (v/v) on the Microparticle Fabrication.....	193
Figure 6.14. Stability Study of Pd-TMV-PEGDA Microparticles as Catalysts for Dichromate Reduction	197

1. Introduction

The objective of the work presented in this dissertation was to examine the fabrication of novel viral-templated palladium (Pd) nanocatalysts by two readily controllable approaches (chip-based surface assembly format and hydrogel microparticle encapsulation format), and to investigate their catalytic activity for liquid phase catalytic reactions. A variety of methods have been established for the nanocatalyst synthesis based on different supports¹. Despite these advances, there still exists a critical need for robust, simple and readily-controllable routes to fabricate highly active, stable and recyclable nanocatalysts. One major drawback in the heterogeneous liquid phase catalysis is relatively rapid deactivation of the catalysts under operating conditions, mainly due to poisoning, sintering or leaching. Although supports have some advantages, including the ability to impart new selectivities as well as keeping the catalysts dispersed and stable, the reaction activity and selectivity can be interfered or even inhibited by supports. Furthermore, heterogeneous catalyst synthesis is inherently unpredictable due to harsh preparation conditions and artifacts from supports. Second, homogeneous catalysts are difficult to separate from reaction products or to recover for repeated use without further generating pollutants^{2,3}. Another catalytic system based on well-dispersed colloidal nanoparticles, so-called semi-

heterogeneous systems, is one of the most attractive alternatives. While combining the advantages of both homogeneous and heterogeneous catalysts, these systems also suffer from lack of stability and in-situ reaction monitoring.

The focus of this dissertation is to harness the unique physical and chemical properties of tobacco mosaic virus (TMV) as templates for the synthesis of novel metal nanocatalysts that possess advantages of both homogeneous and heterogeneous catalysts, including controllable particle size, location, loading density, catalytic activity and recyclability.

The synthesis of nanocatalysts with controllable particle size and recyclability is a challenge. TMV templates allow for readily controllable surface assembly and size controllable metal particle formation on the outer surface. In this dissertation, I examined a novel catalyst synthesis approach, which is chip-based bottom-up TMV assembly followed by metal decoration along TMV. This approach provides an alternative way for the fabrication of promising nanocatalysts.

(Chapter 2)

The in-depth studies of reaction mechanism and kinetics for most reactions are challenging. The nanocatalysts in surface-assembled format allows for real-time in-situ monitoring of reaction extents, fast screening of reaction conditions, and simple catalyst and product recovery. All the above advantages make the kinetics

study of dichromate reduction feasible. The study of catalyst synthesis-structure-activity relationship is also a challenge. By tuning the concentrations of Pd precursor and reducing agent during the synthesis procedure of chip-based Pd-TMV catalysts, the Pd nanoparticle size and loading density is controllable, which leads to the control of catalytic activities. (Chapter 3)

The routes to control the loading and location of metal or inorganic catalysts in small-length scale of close systems, such as micro reactors, are still lacking. TMV's surface assembly properties provide unique opportunities to control both the catalyst loading density and precise location by facile routes under mild aqueous conditions. (Chapter 4)

The design of ligand-free, green, recyclable catalysts for Suzuki Coupling reaction under aqueous solution and the mechanistic examination of the nature of the real active species in Pd catalyzed Suzuki reaction are big challenges. In this dissertation, chip-based Pd-TMV catalysts allow for the easy separation from the reaction system without product contamination and real-time monitoring of reaction extent. Meanwhile, the simple separation of chip-based catalysts enables the study of the real mechanism of Suzuki reaction. (Chapter 5)

Integration of nanoscale functional materials into a robust and readily deployable format/platform/scaffold is needed in order to be able to harness such

functionalities. Packaging functionalized viral nanotemplates in a robust, highly reproducible format provides opportunities for improved kinetics and reactivity with the components of interest, such as metal nanoparticles. The challenge arises, in part, from aggregation and stability issues with metal and viral nanoparticles. In this dissertation, this challenge is addressed by embedding functionalized TMV nanotemplates in hydrogel microparticles with replica molding technique (Chapter 6).

The potential application of chip-based viral-templated nanocatalyst synthesis approach can be readily extended to other viral biotemplates, metals for a variety of inorganic or organic reactions under mild conditions. Meanwhile, the hydrogel encapsulated viral-templated nanocatalyst synthesis approach presented in this work can be extended to other polymeric hydrogel systems with multi-functionalities.

1.1. Palladium Nanocatalysts

Palladium (Pd) is one of the most important elements in transition metal catalysis, and has been extensively used in a wide array of reactions both in homogeneous and heterogeneous systems. Importantly, a series of palladium catalyzed C-C cross-coupling reactions⁴⁻⁷ have been studied, and represent an ongoing interest in economical and environmentally benign synthetic routes to value-added

chemicals. Another important group of Pd-catalyzed reactions include selective glycerol oxidation^{8,9} for value-added chemical synthesis from renewable sources and detoxification of chemicals for environmental cleanup, notably reduction of dichromate (Cr(VI)) to less toxic chromate (Cr(III)) for waste site treatment^{10,11} and dehalogenation of halogenated aromatic hydrocarbons¹²⁻¹⁴ for groundwater cleanup.

Generally, the Pd catalysts are in two types, either homogeneous or heterogeneous, depending on whether a catalyst exists in the same phase as the reaction system. First, homogeneous or colloidal systems suffer from stability issues in real world situations and arduous recovery of the expensive precious metal catalysts^{15,16}. Second, traditional heterogeneous catalysts are relatively inactive due to non-uniform particle size, and their reactivity strongly depends on supports, hampering efforts to understand molecular mechanisms^{15,16}. In the development of catalysis, the use of nanoparticles has built up a bridge between homogeneous and heterogeneous catalysis^{15,17}. Metal particles in nano-scale have higher activities under mild conditions because of relatively large surface-to-volume ratio, which makes them attractive catalysts. On one hand, nanoparticles can be soluble and thus act homogeneously when nanoparticles are synthesized by the bottom-up approach from molecular precursors including a metal salt, a macromolecular stabilizer, and a reducing agent¹⁷. Typical macromolecular

stabilizer can be polymers(PVP¹⁸), dendrimers¹⁹, ligands^{20,21}, and surfactants^{22,23}.

On the other hand, Pd nanoparticles can be stabilized by solid supports and act heterogeneously. Typical solid supports include all sorts of different metal oxides (oxides of Si²⁴, Al²⁵, Ti²⁶, Zr²⁷, Zn²⁸) in various forms (aerogels²⁹, sol-gels³⁰ and high surface sphere³¹), or carbon supports (charcoal⁶, activated carbons³² and carbon nanotubes^{33,34}). The solid supported Pd nanoparticles have advantages such as good reactivity due to the high surface area from small nanoparticles, good recyclability and reusability due to the heterogeneous properties.

Despite such efforts made, making heterogeneous catalysts possess more of the remarkable properties of homogeneous ones is still a challenge. The goal would be to simultaneously take advantage of the advantages of organic ligands or of the relatively rigid coordination of transition metal atoms in a solid matrix. In principle, supported organometallic catalysts could make this goal reality. Metal crystallites modified by ligands, on one hand, or by attachment to a surface, on the other hand, partially correspond to this ideal picture. Rather than electronic interaction with the catalytically active metal, grafting, or more precisely a tethering, of organometallic molecules by one of their side chains (so-called immobilization) contributes more to the great success of supported organometallic catalysis. For most of the cases, silica is the main substrate for the attachment of the organometallic catalysts, leading to remarkable scientific developments and

useful applications. However, there are still some limitations of silica substrate, including poor electronic interaction, lack of adequate ligand field or a rigid, electronically active coordination. Other supports either make tethering impossible or destroy complexes or just add an unmodified function of the support, to make a bifunctional catalyst. The ideal case would be that both organic structures and atoms belonging to the solid substrate should be involved to cooperate in a new type of activity. The approach probably pertains to surface science, with the difficulties inherent to the difference of techniques used for metals and oxides, and the enormous difficulty to attach elaborate structures on surfaces.

In the following subsections, the general Pd nanocatalyst synthesis methods and two important chemical reactions, dichromate reduction reaction and Suzuki coupling reaction, will be further introduced.

1.1.1. Synthesis of Palladium Nanocatalysts

Generally, the preparation of supported Pd nanocatalysts generally involves contacting a porous support with a Pd precursor solution and its subsequent conversion into the active component¹. The interaction between the solvated precursors and the support surface is often due to the electrostatic attraction.

The most commonly used positively charged Pd complex ion is $\text{Pd}(\text{NH}_3)_4^{2+}$, which is stable in neutral and moderately basic environments. The ligands can simply be removed from the loaded support by heating. The most widely utilized negatively charged Pd precursor is PdCl_4^{2-} , which is stable in neutral and acid solutions, provided the Cl/Pd ratio is high enough to avoid hydrolysis¹. Some researchers also make use of neutral palladium complexes that interact, generally from non-polar environment, with specific surface sites of the supports¹. Most often the acetylacetone complex of palladium, $\text{Pd}(\text{C}_5\text{H}_7\text{O}_2)_2$ or simply $\text{Pd}(\text{acac})_2$, in inert solvents like benzene and toluene is used¹. Another precursor is $\text{Pd}(\text{C}_3\text{H}_5)_2$ dissolved in pentane. This allylic complex is highly reactive towards water and hydroxylated surfaces¹.

In this dissertation, Na_2PdCl_4 is utilized as the Pd precursor. Usually, the solvation of Pd cations in water leads to the formation of partially covalent bonds between the central Pd cation and the water ligands. Charge transfer from filled orbitals of the water ligands to the central Pd ion increases the positive charge on the hydrogen atoms of the coordinated water molecules, which further increases their acid character and promotes hydrolysis. The equilibrium equations³⁵ of aqueous Pd chloride complexes are shown in Figure 1.1. The top line is due to the autohydrolysis, while the bottom line is generally due to alkaline hydrolysis or thermal hydrolysis.

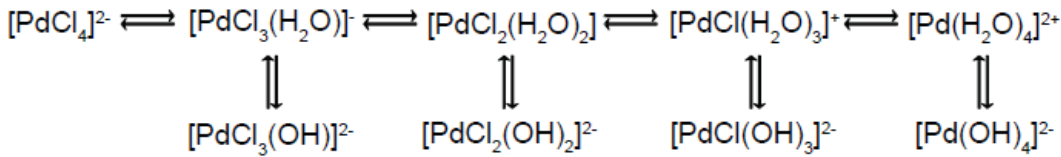


Figure 1.1. Equilibria of Aqueous Pd Chloride Complexes³⁵

As shown in Figure 1.1, the square planar PdL_4 complexes are the most favorite forms of the Pd^{2+} ion. The formation of colloidal PdO particles by hydrolysis of a palladium precursor solution has been reported³⁶⁻³⁸. These findings are of great interest for the preparation of supported catalysts with well-defined palladium particle sizes.

The $[\text{PdCl}_{4-x}(\text{H}_2\text{O})_x]^{(x-2)}$ complexes in solution are characterized by a spin-forbidden d-d transition of square-planar Pd^{II} complexes in the region between 350-500 nm³⁹. As summarized in Table 1.1 from the reported studies^{39,40}, the maximum absorption of the $\text{Pd}(\text{II})$ d-d transition band shifts to shorter wavelengths when the chloride ligands are replaced by water ligands.

Table 1.1. Literature Values of the $\text{Pd}(\text{II})$ d-d Transition Band Position for the Different $\text{Pd}(\text{II})$ Chloride Complexes in Aqueous Solution

Pd(II) chloride complex	λ/nm
$[\text{PdCl}_4]^{2-}$	474
$[\text{PdCl}_3(\text{H}_2\text{O})]^-$	431

[PdCl ₂ (H ₂ O) ₂]	420
[PdCl(H ₂ O) ₃] ⁺	406
[Pd(H ₂ O) ₄] ²⁺	378

The preparation methods of supported Pd nanoparticles have been diversified and currently include impregnation³⁴, deposition/precipitation³³, electroless deposition^{41,42}, sol-gel³⁰, sonochemical⁴³, micro-emulsion⁷, electrochemical⁴⁴, cross-linking⁴⁵ and so on. The classification is usually based on the nature of the first step in the procedure in which the Pd precursors and the support are combined. Among various types of carbons, activated carbon is still the most commonly used adsorbent and catalyst support, because of its high surface area (500–1200 m²/g) and low cost. The activated carbon contains a large range of elements, such as hydrogen, oxygen and sulfur. As an emerging support, carbon nanofibers⁴⁶ show great potential related to tailoring of surface properties, accessibility and mechanical strength. For carbon supported catalysts, the thermal treatment often is the most important factor in determining the Pd dispersion. Thermal treatment in an inert atmosphere prior to the reduction is essential in obtaining high Pd dispersion¹⁵. The direct reduction of the Pd-precursor by the carbon support gives rise to large Pd particles. As another big group of Pd nanocatalysts, oxide-supported Pd catalysts prepared via sol-gel techniques give rise to Pd particles of 1 nm at low loading⁴⁷. The ion-exchange and impregnation

are most often used for oxide-supported Pd catalysts. In general, careful washing following adsorption is beneficial for dispersion as well as is calcination prior to reduction¹⁵. High Pd dispersions call for decomposition of the precursor in an inert atmosphere. Usually, gas-phase reduction leads to higher dispersions than liquid-phase reduction. The challenge is to develop supported Pd nanocatalysts with high dispersion and low Pd loading density.

1.1.2. Removal of Hexavalent Chromium

Hexavalent Chromium Cr(VI) is prevalent in the industrial wastewater in the U.S. (listed as the second most common inorganic contaminant in water^{48,49}), and the Agency for Toxic Substances and Diseases Registry (ATSDR) classifies Cr(VI) as the top 16th hazardous substance⁵⁰. The industrial sources of Cr(VI) include leather tanning, cooling tower blowdown, plating, electroplating, anodizing baths, rinse waters and so on⁵¹.

Cr(VI) is highly mobile in the environment and is demonstrated to be hazardous to the public health due to its mutagenic and carcinogenic properties by inducing oxidative stress, DNA damage, apoptotic cell death and altered gene expression⁵². In contrast, Cr(III) is less toxic than Cr(VI) and listed as an essential element, as micronutrient, to maintain good health and helps in maintaining the normal metabolism of glucose, cholesterol, and fat in human bodies⁵³. In addition, Cr(III)

is nearly insoluble at neutral pH⁵⁴. Therefore, the reduction of Cr(VI) to Cr(III) serves as a key process for remediation of Cr(VI)-contaminated water and wastewater.

Techniques reported for the Cr(VI) removal include adsorption⁵⁵, biosorption⁵⁶, reduction⁵⁷, photoreduction⁵⁸, filtration reverse osmosis, ion-exchange, foam flotation, and electrolysis⁵¹. Conventionally, the removal of Cr(VI) includes chemical reduction of Cr(VI) to Cr(III) followed by precipitation. Commonly used inorganic reducing agents for the Cr(VI) reduction are ferrous ion⁵⁹, nano-sized zero-valent ion⁶⁰, sulphite⁶¹, and ferrous sulfate⁶². An area of expanding research toward Cr(VI) reduction is the catalytic reduction of Cr(VI) with organic reductants by applying metal catalysts, such as oxides⁶³ (TiO_2 ⁶⁴, aluminum oxide $\gamma\text{-Al}_2\text{O}_3$ ⁵⁷, goethite $\alpha\text{-FeOOH}$ ⁶⁵), nano-sized mixed metallic particles⁶⁶, palladium nanoparticles^{10,11}, mesoporous Al_2O_3 -supported⁵⁷ or TiO_2 -supported²⁶ Pd nanoparticles as catalysts.

Pd is a particularly important metal catalyst for the Cr(VI) reduction. Omole et al^{10,11} used colloidal Pd nanoparticles as catalyst and formic acid as a reducing agent to achieve an efficient reduction of Cr(VI) to Cr(III). Dandapat et al.⁵⁷ used thick Pd nanoparticle-incorporated mesoporous $\gamma\text{-Al}_2\text{O}_3$ films as reusable catalysts for Cr(VI) reduction in the presence of formic acid. Shi's group⁶⁷ recently demonstrated the catalytic reduction of Cr(VI) using Pd immobilized electrospun

polyethyleneimine (PEI)/polyvinyl alcohol (PVA) nanofibers. These studies clearly suggest that Pd nanoparticles could be used as efficient catalysts for Cr(VI) reduction. As described previously, the development of various supporting materials that are able to efficiently immobilize and disperse small amount of Pd nanoparticles and retain their catalytic activity is highly demanded for practical environmental remediation applications. Therefore, in this dissertation project, a novel synthesis approach for the fabrication of viral-templated Pd nanocatalysts has been developed and applied for dichromate reduction.

1.1.3. Suzuki Cross-coupling Reaction

One of the most useful cross-coupling reactions in organic chemistry is Suzuki-Miyaura cross-coupling reaction since it is discovered⁴. The Suzuki reaction is the cross-coupling of an aryl or vinyl-boronic acid with aryl- or vinyl-halides. Pd is the most commonly used catalyst, and the general catalytic cycle involves oxidative addition-transmetalation-reductive elimination sequences, which is shown in Figure 1.2^{4 68}. Oxidative addition is often the rate-determining step in a catalytic cycle. The relative reactivity decreases in the order of I > triflates(OTf) > Br >> Cl⁴. Aryl and 1-alkenyl halides activated by the proximity of electron-withdrawing groups are more reactive to the oxidative addition than those with donating groups⁴.

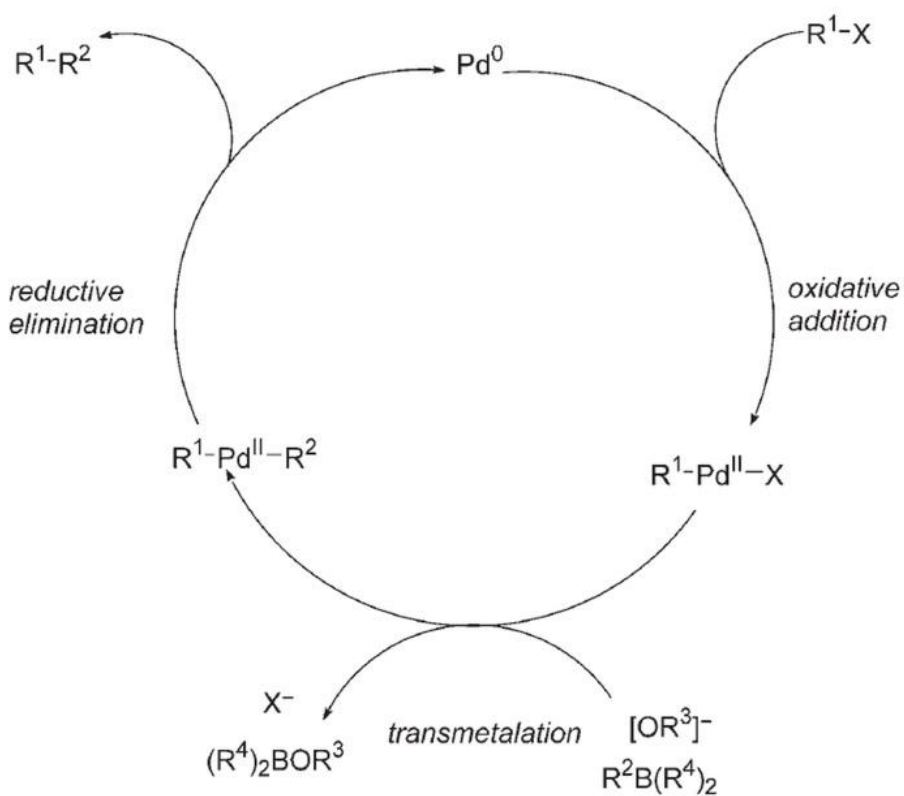


Figure 1.2. The Typical Pd Catalytic Cycle of Suzuki Reaction⁶⁸

In the past few decades, various forms of palladium have been utilized as precatalysts for the Suzuki coupling reactions. All forms of palladium⁶⁸, including discrete soluble palladium complexes, solid-supported metal ligand complexes, supported palladium nano- and macroparticles, soluble palladium nanoparticles, soluble ligand-free palladium, and palladium-exchanged oxides have been used. Conventionally, most Pd catalysts are in homogeneous form^{20,69,70}, which provides excellent activity and selectivity, and allows for the

establishment of structure-activity relationships and ligand selection⁷¹. For example, phosphine ligand based Pd catalysts⁷¹, such as $\text{Pd}(\text{PPh}_3)_4$, $\text{PdCl}_2(\text{PPh}_3)_2$, $\text{Pd}(\text{OAc})_2$ plus PPh_3 , are most commonly used for Suzuki coupling reaction. However, homogeneous Pd catalysts suffer from many drawbacks lying in the removal, reuse of the catalyst and the contamination of products⁶⁸. From these perspectives, heterogeneous Pd catalysts immobilized on supports are necessary due to the easy removal and filtration. In the past few decades, there have emerged a number of reports regarding Pd nanoparticles immobilized on various supports, including organic (mainly organic polymers⁷² and carbon material^{7,33}), inorganic (silica⁷³, zeolites⁷⁴, metal oxides⁷⁵, etc.) and hybrid organic-inorganic supports (mainly grafted silica⁷⁶). These catalysts are also called as “ligand-free catalysts”⁷ or “green catalysts”⁷⁷.

Although a lot of achievements have been made about the Suzuki reaction catalyzed by supported-Pd catalysts, many unsolved issues remain to be tackled. One of the biggest concerns is the nature of the real active species in Pd catalyzed Suzuki reaction-homogeneous or heterogeneous catalysis⁷⁸⁻⁶⁸. Historically, researchers described different forms of Pd used as active catalytic species. Nowadays, reserachers start to narrow the scope of types of Pd that can be considered true “catalysts” in these coupling reactions, because many Pd precatalysts undergo transformations during or before the catalytic reaction.

Several methods can be utilized to assess the real active Pd species, including kinetic studies, filtration tests, and selective poisoning for catalysts⁶⁸. For most so-called “heterogeneous catalysts”, a generally accepted mechanism is considered to follow Pd leaching mechanism, where the oxidative addition of the aryl iodide to the Pd(0) surface release soluble Pd(II) species into solution. The cumulative evidence to this point indicates that most supported forms of Pd(0) metal particles are in fact precursors for soluble palladium species that are the real catalysts in C-C coupling reactions.

Due to the unsolved problems existing for Suzuki coupling reaction, the search for simple, reliable and environmentally friendly catalyst synthesis methods would open up doors for gaining deeper insights into real catalytic reaction mechanisms at the nano or molecular level. Second, the development of energy efficient and environmentally benign protocols, such as using water as solvent, will be beneficial for the down-stream treatment. Finally, the exploration of novel solid supports for active Pd nanoparticles will be a key point in the context of sustainable chemistry. Future progress in this area for Suzuki coupling reaction will focus on finding controllable, recyclable and active catalysts under mild aqueous heterogeneous conditions.

1.2. Hydrogel Microparticles

1.2.1. Radical Chain Photopolymerization

Radical chain polymerization is a chain reaction consisting of a sequence of four events: initiation, propagation, inhibition and termination. When an inhibitor is present, such as oxygen, an inhibition event should be considered. Photoinitiated polymerization reactions occur when radicals are produced by UV light irradiation of the reaction system⁷⁹. A general reaction mechanism illustrating these four sequences of events with photoinitiator, I, radical species, R, monomer or prepolymer, M, and inhibitor, Z, is shown in Figure 1.3. Each initiator molecule forms two radical species following exposure to UV light.

The initiation event involves two reactions. The first initiation reaction forms two radical species via photolysis. The second initiation reaction involves the addition of a radical species to the first monomer or prepolymer molecule to produce the chain-initiating radical, M_1^\cdot . During propagation, successive additions of monomer or prepolymer molecules form growing polymer chains identical to the previous one, but larger by one monomer unit. At termination, the propagating polymer chain stops growing. Bimolecular termination may occur by coupling, to form one chain or disproportionation, to form two chains. For coupling, propagating radical chains react with each other. For termination, a hydrogen

radical that is beta to one radical center is transferred to another radical center to form two polymer molecules, one saturated and one unsaturated⁷⁹. A second termination mechanism is primary radical termination, where a primary radical reacts with a growing polymer chain to form dead polymer.

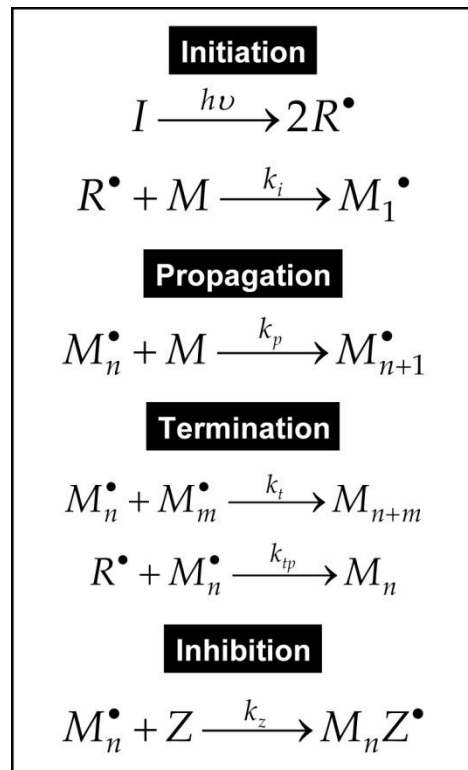


Figure 1.3. General Reaction Mechanism for Photoinitiated Radical Chain Polymerization⁷⁹.

The main advantages of photoinitiated polymerization include: (1) rapid polymerization rates (2) intense illumination (3) spatial resolution of the polymerization (4) the ability to control the initiation rates through the source of

radicals, light intensity, and temperature in addition to the regions⁸⁰. The basic polymerization mechanism for each of the three microparticle fabrication techniques presented in this dissertation is radical chain photopolymerization. In Chapter 6 of this dissertation, photoinitiated chain polymerization was used for the hydrogel microparticle fabrication.

The prepolymer solution components used for each of the hydrogel microparticle fabrication strategies presented are poly (ethylene glycol) (PEG), which is well known for its hydrophilic, biocompatible, and non-fouling characteristics⁸¹. In its prepolymer form at a molecular weight (MW) of 700, and with two double bonds per molecule, poly (ethylene glycol) diacrylate (PEG-DA) crosslinked to form the hydrogel microparticles in the presence of the photoinitiator Darocur 1173. Non-reactive PEG at a MW of 200 was also used in some of the prepolymer solutions, in part, to assist with the solubility of the photoinitiator and help disperse viral-templated metal nanostructure.

1.2.2. Applications of Hydrogels in Catalysis

Hydrogels are crosslinked materials capable of absorbing a large amount of water without dissolving. They have tunable degrees of swelling by changing the ionic strength, pH, pressure, temperature, light, electric and magnetic fields in their environment⁸². The highly porous 3D structure of hydrogel microparticles can

improve molecular interactions and offer a hydrophilic environment with more favorable solution kinetics. The ability to customize specific microparticle features, such as magnetic capabilities^{83,84}, provide an alternative means for separation from bulk solution, patterning, or self-assembly. Due to the above mentioned advantages, hydrogels have been used for a variety of applications, including water purification and separation⁸⁵, active agent delivery vehicles (drugs, protein, and gene)⁸⁶, artificial organs, chemical or biosensors and actuators⁸⁷ and catalyst carrier^{82,88-91}. Among various hydrogels, PEG is a nondegradable, hydrophilic polymer with attractive biocompatibility property, so PEG hydrogels have been widely used in biology and medicine for many years in biosensors⁹², drug delivery⁹³, tissue engineering applications⁹⁴. The polymerization of acrylated PEGs with different molecular weight yields highly cross-linked hydrogel network. The physical properties of PEG-based hydrogels can easily be controlled by varying the molecular weight of the PEG used, and the transparent nature of PEG hydrogels makes them suitable for various detection schemes in biosensing applications.

In recent years, hydrogels have also been used as a stabilizing platform for viral or metal nanoparticles, which tend to suffer from stability and aggregation problems⁹⁵. Hydrogels serve as effective templates for the in-situ synthesis of metal nanoparticles and even used as a reactor for chemical reactions. Sahiner et

al⁹⁰ synthesized 50-100 nm Ni nanoparticles inside poly(2-acrylamido-2-methyl-1-propansulfonic acid) (p(AMPS)) hydrogel and applied for 2- and 4-nitrophenols(4-NP) reduction. Lu et al⁹¹ chemically entrapped 35 nm Ag nanoparticles on the surface of poly(vinyl alcohol) based composite hydrogel for 4-NP reduction. Mohan et al.⁸⁸ fabricated smaller size (3 nm) silver nanoparticles in chemically crosslinked poly[N-isopropylacrylamide-co-(sodium acrylate)] hydrogels and tailored the size and features of silver particles in the hydrogel network architecture. Butun et al.⁸² reported the synthesis of Co, Ni, Cu and Ag nanoparticles based on acrylamidoglycolic acid (AAGA) hydrogel template, and the use of Ag-hydrogel as reactor vessel for the 4-NP reduction. Despite the above studies on the polymeric hydrogel application in catalysis, there are limited reports on the nanoparticle-encapsulated PEG based hydrogels for catalysis application. Polyethyleneglycol (PEG) with large chain length has been emerging as both reducer and stabilizer for the synthesis of Pd nanoparticles in the studies of aerobic alcohol oxidation^{96,97}, selective hydrogenation reaction^{98,99} and Heck reaction¹⁰⁰. Meanwhile, PEG is the most commonly used, relatively inexpensive, non-volatile, nontoxic and environmentally benign polymer. Therefore, here in this dissertation (Chapter 6), PEG based hydrogel was used to encapsulate the catalytically active viral-templated metal nanoparticles to prevent aggregation of metal nanostructure and meanwhile provide recyclability.

1.2.3. Replica Molding (RM) Technique

There are a variety of methods established for the fabrication of hydrogel microparticles bearing unique, and mostly customizable features, such as chemical anisotropy, complex shapes, core/shell structures, magnetic capabilities, or thermosensitivity¹⁰¹⁻¹⁰³. The methods range from batch formats, such as photolithography or template-based printing to continuous formats, such as microfluidics^{101,104}. Despite these advances, there still exists a critical need for rapid and well-controlled routes to fabricate multifunctional microparticles.

Replica Molding (RM)^{103,105,106} is an efficient soft lithography for the duplication of shape from the surface of a mold. Replica molding of an organic polymer against an elastomeric master (eg: poly(dimethylsiloxane) (PDMS)), while that master is deformed, provides a strategy for the fabrication of complex micropatterns on surfaces. As shown in Figure 1.4^{103,106,107}, Replica Molding (RM) consists of three steps: i) creating a topographically patterned master (usually by conventional techniques, such as photolithography or micromachining); ii) transferring the pattern of this master into PDMS by replica molding; and iii) fabricating a replica of the original master by solidifying a liquid precursor against the PDMS mold. Another very similar technique developed by Whitesides' group is called Solvent-Assisted Micromolding (SAMIM), which uses an elastomeric mold and an appropriate solvent to emboss polymer films.

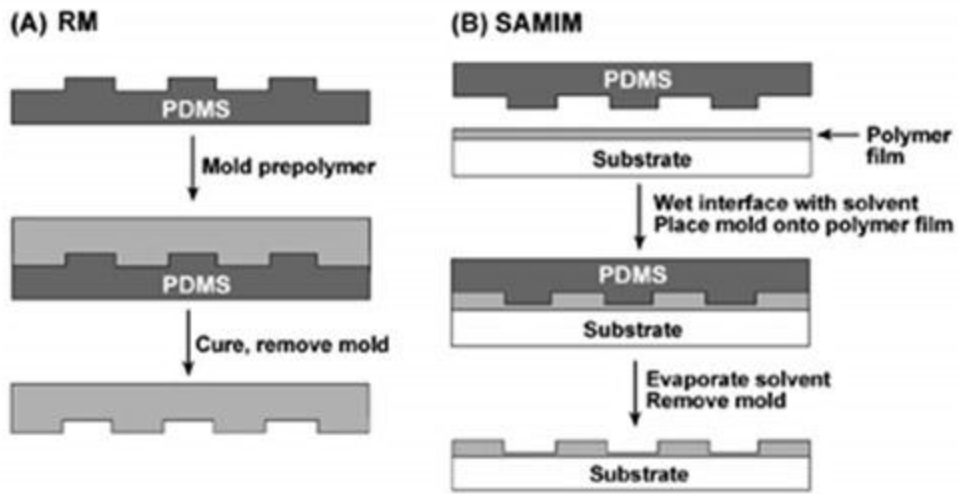


Figure 1.4. Replica Molding and Solvent-Assisted Micromolding

The value of replica molding is as a replication method: it allows duplication of three-dimensional topologies in a single step; it also enables reliable duplication of complex structures in the master in multiple copies with nanometer resolution in a simple, reliable, and inexpensive way. Due to the above advantages, Replica molding has been used for the mass-production of a variety of structured surfaces such as compact disks (CDs), diffraction gratings, holograms, and micro-tools¹⁰⁶. The capability of RM has been expanded by molding against elastomeric PDMS molds rather than against rigid molds; the use of elastomers makes it easier to release small and fragile structures. In this dissertation, the RM technique with PDMS mold was applied for the PEG hydrogel microparticle fabrication (Chapter 6).

1.3. Viral-based Nanomaterial Synthesis

Biological macro/supramolecules (e.g., DNA^{93,94},^{108,109}, peptides¹¹⁰ or proteins^{111,112}, bacteria^{113,114}) offer various chemical, structural, and genetic functionalities for the synthesis of novel nanomaterials. Particularly, viruses and virus-like protein assemblies have attracted substantial attention as biotemplates for nanomaterial synthesis in the past two decades. As shown in the schematic drawings of Figure 1.5, a variety of viruses have been used as platforms for nanomaterial synthesis. All of these viruses are composed of a proteinaceous shell that encapsulates viral genomic material and accessory structural and replication proteins. These viruses are generally in three forms: icosahedral, filamentous and rod-shape.

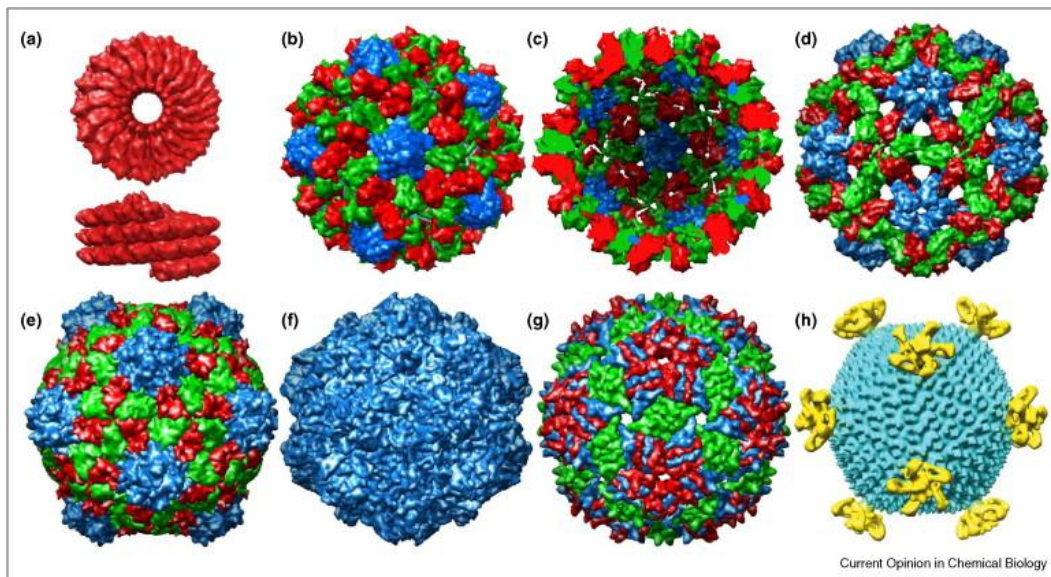


Figure 1.5. Structures of a Selection of Viruses used for Nanotechnology

(a) Tobacco mosaic virus (TMV) intermediates; 18 nm in diameter and variable in length; (b) cowpea chlorotic mottle virus (CCMV) 28 nm in diameter; (c) interior view of a CCMV VLP; (d) swollen form of CCMV; (e) cowpea mosaic virus (CPMV) 31 nm in diameter; (f) canine parvovirus (CPV) 26 nm in diameter, (g) bacteriophage MS2 26 nm in diameter, (h) *Sulfolobus* turreted icosahedral virus (STIV) 70 nm in diameter. Note not drawn to scale. All structures were rendered using Chimera or Viper, except in the case of STIV.¹¹⁵

There exists a wide range of viral based materials and related applications, including metal and metal oxide nanoparticles and nanowires for catalysis and nanoelectronics, high surface area electrodes for energy applications, and sensing/ or tissue engineering scaffolds for biomedical applications^{116,117}. Although most early studies were limited to the demonstration of the concepts, an increasing number of recent developments show performances and capabilities that are beyond or impossible to achieve by traditional materials, top-down approaches, and inorganic devices. The unique advantages that viral template can offer should be fully understood and better manipulated. First, unlike inorganic or man-made nanoscale species such as nanoparticles and carbon nanotubes, the dimensions and structures of viral assemblies are precisely controlled. Second, due to their inherent protein capsid-based nature, diverse chemical functionalities (i.e., amino acid side chains) are precisely spaced and can be readily manipulated under mild reaction conditions. Last but not the least, genetic functionalities can be readily

added for a broader application of viral templates, which is one of the most unique advantages of viral assemblies over man-made nanomaterials. Specifically, efforts to confer precisely spaced chemical functionalities⁴² by introduction of amino acids and/or peptide screening (a.k.a. biopanning) have led to drastic expansions and new possibilities. In the following subsections, the application of three types of virus in the field of nanomaterial synthesis will be introduced.

1.3.1. Icosahedral Viruses

Spheroidal plant viruses are one class of virus, where two widely listed viruses are Cowpea Mosaic Virus (CPMV) and Cowpea Chlorotic Mottle Virus (CCMV). The most unique feature of this spheroidal viruses or protein cages is their inner cavity, which have been harnessed for the synthesis of precisely controlled nanoparticles.

CPMV is an icosahedral virus with a diameter of 28 nm. The structure of CPMV is composed of a single strand positive-sense RNA enclosed by two types of coat protein subunits. Each CPMV particle consists of 60 of each type of coat protein. CPMV viral particles are stable over the pH range of 3-9 and maintain their structural integrity when heated to 60 °C for an hour. The exterior of genetically mutated CPMV was utilized as a biological template for the synthesis of silica

nanoparticle¹¹⁸. In the study, the insertion of a 12 amino acid peptide sequence previously was determined to initiate the nucleation of silica mineralization. The formed silica nanoparticles were fairly monodisperse and exhibited a diameter of ~32 nm, suggesting that the layer of silica deposited on the viral particles was about 2 nm.

Another icosahedral plant virus used as a viral template is CCMV, which has a diameter of 28.6 nm and is comprised of a coat protein shell encapsulating a single strand of positive-sense RNA. Different from CPMV, CCMV particles are stable at pH 5 but swell up to 10% in size when the pH is increased to 7. Trevor Douglas and Mark Young have employed CCMV as a host to encapsulate inorganic, metallic precursor ions at pH values >6.5, followed by lowering the pH to achieve the crystallization of either paratungstate or decavanadate within the interior of the CCMV particles¹¹⁹. The resulting metallic nanoparticles were only observed in the presence of CCMV and exhibited the same monodisperse diameter as the CCMV particles. In another study done by Douglas and coworkers, titania nanoparticles as well as amorphous titania⁸⁴ were synthesized by using anionic titanium salts in conjunction with the pH-dependent gating mechanism of CCMV. β -TiO₂ composite formed within CCMV possessed the same diameter of the viral capsid and showed photocatalytic activity in the presence of methylene blue⁸⁴. However, the TiO₂ nanoparticles show low

catalytic activity and apparent aggregation after the photocatalytic reaction due to the instability of CCMV capsid.

1.3.2. Filamentous Viruses

Another group of bacterial virus is in filament shape. The utilization of filamentous M13 bacteriophage has revolutionized the field of biotemplate-based materials synthesis. Angela Belcher and coworkers have made a series of endeavors to the M13 based nanomaterial synthesis and application. As shown in Figure 1.6¹²⁰, M13 is composed of a single strand circular DNA with 6400 nucleotides encapsulated by a coat protein shell. The diameter of the phage is 6 nm, while the length of the phage is dependent upon the length of its DNA and measures ~1μm for the native strain of M13. Five forms of coat proteins and five copies of each are present on the phase. Protein-7 and protein-9 (pVII and pIX) exist at one end of the phage while protein-3 and protein-6 (pIII and pVI) exist at the other end.

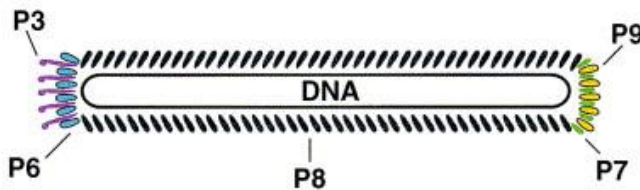


Figure 1.6. Schematic Diagram of the M13 Structure

The location and population of each coat protein subunit is shown to encapsulate a single circular strand of DNA.¹²⁰

Belcher and coworkers have selected a sequence of peptides that selectively bind to semiconductor single crystals with high affinity by employing combinatorial phage display strategy¹²¹. Five different single-crystal semiconductors: GaAs(100), GaAs(111)A, GaAs(111)B, InP(100) and Si(100) were utilized. Depending on the crystallographic orientation and composition, a single discriminatory peptide sequence was determined for each single-crystal semiconductor. This work has yielded the basis for binding organic peptides on the surface of the M13 phage virus to inorganic semiconductors for the synthesis of nanomaterials using a bottom-up approach.

Belcher and coworkers have also exploited the M13 phage as a biotemplate to synthesize quantum dot nanowires¹²². Specifically, genetically engineered M13 phage were employed to display a previously determined peptide sequence in the pVIII M13 coat protein that specifically facilitates the nucleation and growth of ZnS or CdS nanocrystals. Additionally, they also demonstrated the versatility of M13 phage to display more than one genetically engineered peptide sequence to nucleate two different quantum dots for the construction of multicomponent materials. Furthermore, Belcher and coworkers have synthesized annealed ZnS and CdS nanowires by increasing the temperature of the system to disintegrate the virus¹²³. For each distinct nanowire fabricated, the crystals comprising the

nanowires retained their preferred crystallographic alignment. In order to demonstrate the versatility of genetically engineered M13 phage for nanomaterial synthesis, a photochemical catalyst was constructed for visible light-driven water oxidation¹²⁴. Genetically mutated M13 phage displaying a peptide sequence exhibits selective binding for iridium oxide in conjunction with the chemical attachment of zinc porphyrins to the phage coat protein to act as photosensitizers. In another work done by Belcher and coworkers¹²⁵, magnetically-recoverable metal nanowire catalysts were synthesized by utilizing native M13 phage particles as biotemplates. The surface exposed anionic carboxylate functionalities on native M13 phage interact with cationic metal species to facilitate the phage-templated synthesis of rubidium, ruthenium, and palladium nanowires. Indeed, pVIII coat protein region of the M13 phage facilitated the formation of the metallic nanowires, while pIII located at the tip of the phage was modified for the binding of an additional material, such as magnetic Fe₃O₄. Constructing phage particles with modified pIII coat proteins allowed for the synthesis of a multicomponent system with both magnetic field and catalytic activity. Despite the great screening utility, M13 is not robust or stable, which spontaneously degrade in water after 2-3 days.

1.3.3. Rod-Shaped Viruses — Tobacco Mosaic Virus (TMV)

As the first discovered virus, Tobacco Mosaic Virus (TMV) is a typical rod-shaped virus. TMV has served as the main model system for nucleic acid-protein and virus-host interaction studies for many decades¹²⁶⁻¹²⁸. TMV has been extensively studied for its assembly/disassembly mechanism, chemical modification and bio-nanomaterial synthesis in the broad biology fields. The in-depth understanding of TMV's attractive properties and advantages has been widely employed for TMV-based nanomaterial synthesis.

1.3.3.1. Structure of TMV

As shown in Figure 2.1(a), the length of wild type TMV is 300 nm and the diameter is 18 nm¹²⁹. TMV is composed of a 6.4 kb positive strand mRNA enclosed around 2130 identical coat proteins with three nucleotides binding to the inner groove of each protein subunit. The RNA is helically arranged along the entire length of the virus forming an inner RNA-binding channel, whose diameter is 4 nm.

As shown in Figure 1.7, at basic pH and low ionic environment, coat protein exists in the forms of monomers or dimer, trimer, termed 4S or A-protein. The second form is in disk shape rising from the transition of coat protein monomers into aggregation of 38 coat protein subunits, termed 20S disk. The third form of

coat protein is the virion-like structure from the arrangement of coat protein monomers in the cylindrical shape of the fully assembled virus but without the presence of RNA.

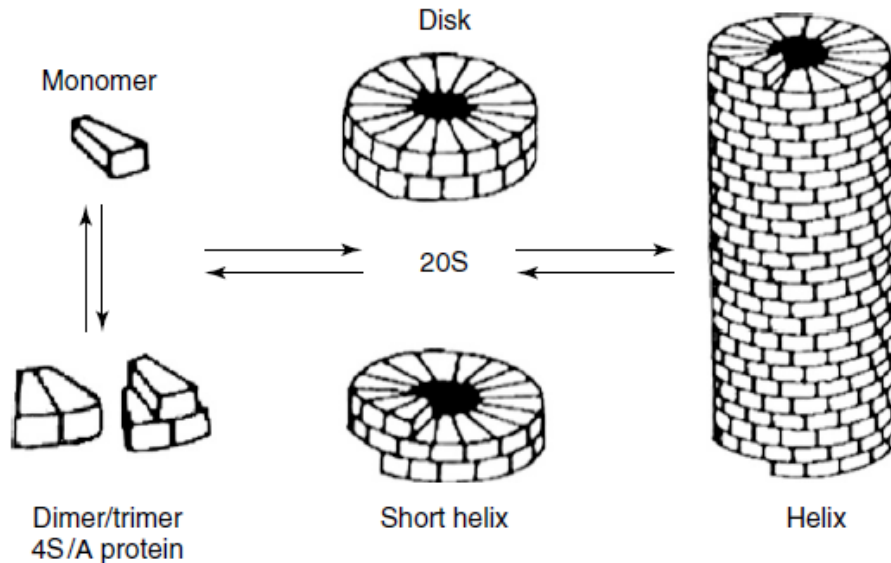


Figure 1.7. Different Forms of TMV Coat Protein¹²⁹

1.3.3.2. Physical and Chemical Properties

TMV also possesses several unique properties as nanotemplates such as extraordinary stability¹³⁰, well-defined structure^{129,131} and simple mass production¹³². For example, TMV's structure is remarkably stable in a wide range of conditions including high temperature (up to 90 °C), broad pH values (2~10) and even in non-aqueous solvents such as 80 % ethanol, methanol and

DMSO^{130,133}. Furthermore, compared to inorganic nanotubes, small genetic modification can be routinely employed to confer precisely spaced functionalities on TMV surfaces via insertion of additional amino acids or peptides¹³⁴⁻¹³⁷. For example, several amino acid side chains have been targeted for chemical modification, such as the side chains of tyrosine and glutamic acid, as well as genetically inserted cysteines¹³⁸. The Francis group has synthetically introduced functional groups to the interior and/or exterior of TMV by covalently attaching small molecules and demonstrated the exploitation of these chemical conjugated TMV in a broad range of applications, from chromophores to artificial light-harvesting systems¹³⁹. In addition, TMV is non-infectious to mammalian cells and can be mass-produced. All the above mentioned unique physical and chemical attributes make TMV become an attractive nanotemplate for the nanoparticle and nanowire synthesis toward a number of other applications¹⁴⁰⁻¹⁴⁵.

1.3.3.3. TMV Assembly

TMV has been playing an important role in the field of biological template technology. Hlady and coworkers¹⁴⁶ first reported the adsorption of TMV in the form of self-assembled and Langmuir–Blodgett monolayers on various substrates. They found that positively charged and hydrophobic surfaces have similar initial rates of TMV adsorption. Knez and coworkers¹⁴⁷ further investigated that adsorption behavior of the tobacco mosaic virus (TMV) on well-defined inorganic

surfaces, such as metal (gold (111)) as well as hydroxyl containing surfaces (mica, glass and silicon wafer). Wang's group also has done a lot of studies on the TMV surface assembly. The self-assembly of TMV in the oil/water interface has been examined¹⁴⁸ and they found that the rods were oriented parallel to the interface at low TMV concentration, while the rods were oriented normal to the interface at high TMV concentrations. Furthermore, the fabrication of two dimensional films of well-ordered, dispersed, oriented TMV has also been investigated^{149,150}. Especially, Wang's group reported the self-assembly of TMV in a glass capillary tube and on flat glass surface via controlled evaporation^{151,152}. Furthermore, TMV surface has been decorated by polymers to form one dimensional conducting polyaniline and polypyrrole nanowires via a hierarchical assembly process^{153,154}. By adjusting the pH value, the arrangement of polymerized polyaniline on the virus was tunable to be in either nonconductive, branched oligoaniline or conductive PANi nanowires. Initial preparation of the TMV-templated PANi nanowires at neutral pH resulted in the arrangement of viral particles end-to-end to form nanofibers longer than the 300 nm length of the TMV.

1.3.3.4. Metal or Metal Oxide Formation with TMV Biotemplates

The surface of TMV coat protein has abundant charged amino acid side chains with uniform intervals, which could serve as potential nucleation sites for the

controlled synthesis of metallic nanoparticles. Mann and coworkers first utilized TMV as a template for the synthesis of inorganic-organic nanotube¹⁴⁴. The incubation of wildtype TMV with metal salt solutions yield evenly dispersed coating of CdS, PbS or Fe oxide nanocrystals on the exterior of TMV. In this study, the synthesis of metallic nanoparticle was restricted to the exterior surface of the TMV because of the preferential electrostatic interaction between the metal ion precursor and the charged functionalities displayed on the TMV external surface. Building upon these initial findings, Mann and coworkers further explored various conditions for the preferential synthesis of metallic nanoparticles on the exterior or interior of the TMV¹⁴¹. By adjusting pH of the reaction conditions, the interior or exterior electrostatic charge was readily controlled due to the difference in pKa value of the exposed amino acid functionalities within the interior channel or on the exterior of TMV. Then the metal nanoparticle deposition was chemically and selectively distinguished between interior or exterior surface of TMV. The amino acid side chains on the surface of TMV are positively charged at acidic pH, so discrete platinum and gold nanoparticles form on the exterior surface of native TMV from reaction with negatively charged metal salt precursor. Similarly, at neutral or slightly alkaline pH, silver nanoparticles were observed in the inside channel of TMV owing to the

preferential interaction between the negatively charged inner channel and the positively charged silver cation precursor.

Kern and coworkers also have done a few studies on the controllable, uniform metal deposition on TMV biotemplates. After activation of TMV with the desired metal ions, chemical reduction or electroless plating produce metal nanoparticles. By employing this electroless deposition approach, nickel, silver, and cobalt nanoclusters were selectively formed on the interior or exterior of the virus by controlling the pH and metal precursor used in the reaction¹⁴³. Meanwhile, Kern and coworkers have also exploited the nucleation sites present within the inside channel of TMV to construct continuous Nickel, Cobalt and Copper nanowires^{140,155}. 3 nm Nickle nanowire was synthesized in the interior of TMV biotemplates by electroless deposition using metal activation complexes together with the reductant dimethylamine borane (DMAB).

In order to further increase the metal-binding affinity of TMV, Culver and coworkers⁴² have engineered a mutated form of TMV, termed TMV2cys, to display two additional cysteine residues at the N-terminus of the coat protein. They demonstrated improved palladium coating density on TMV2cys over TMV-wildtype. The additional sulfhydryl groups on the TMV2cys enhanced the ion uptake of the virus and provided a significant portion of the potential metal loading onto the TMV surface^{156,157}. In addition, TMV2cys efficiently enhanced

the formation of silver and gold nanoparticles⁴². Metal or alloy nanoparticles were also successfully deposited on another genetically modified TMV1cys by the biosorption of Au(III) and Pd(II) precursors and the reduction of the Au(III) and Pd(II) to their respective metals or metal alloy. Manocchi et al.¹⁵⁸ have also exploited the increased metal-binding affinity of TMV1cys to synthesize size controllable palladium nanoparticles by adjusting the concentration of the reducer sodium hypophosphite.

By far, most strategies for the metal particle formation requires the addition of reducing agent, such as dimethylamine borane (DMAB)¹⁴³, sodium borohydride (NaBH_4)¹⁴¹ and sodium hypophosphite (NaPH_2O_2)¹⁵⁸. In 2010, Lim et al.¹⁵⁹ reported a new synthetic strategy enabling highly controlled aqueous-phase palladium crystallization on TMV without the addition of external reducing agents. The TMV2cys biotemplate effectively produced the formation of palladium coating with thickness of 33.4 ± 1.1 nm, which is thicker than on TMV-wildtype. The thicker Pd coating is due to the significant improvement of the palladium precursor uptake and mineralization on the mutant TMV in comparison to TMV-wildtype. Meanwhile, they also found that the surface palladium oxide layer can be readily reduced by room temperature hydrogenation.

Our group has also done a few studies on the Pd metallization on surface-assembled TMV biotemplates and their thermal stability. Manocchi et al.¹⁶⁰

carried out in-situ grazing incidence small-angle X-ray scattering (GISAXS) to examine the thermal stability of viral-nanoparticle complexes composed of TMV and Pd nanoparticle, and found that the stability of the Pd nanoparticles synthesized on TMV is significantly enhanced in comparison to Pd nanoparticles formed on the solid substrate surface. Specifically, the degradation temperature of the Pd nanoparticles increased from 214 °C on gold chips to 240 and 279 °C for small and large Pd particles formed on TMV, respectively. Furthermore, the agglomeration of Pd nanoparticles and TMV degradation is coupled and occur simultaneously. In order to increase the bio-template's stability, Culver and coworker^{161,162} pretreated TMV with aniline before coating a uniform silica layer with thickness of >20nm. These silica shells not only enhanced the stability of TMV, but also promoted the deposition of various metal nanoparticles through conventional silica mineralization chemistries.

1.4. Viral Template-based Nanocatalysts

There are only a few reports on the fabrication and application of nanocatalysts based on virus templates^{84,117,125} or protein cages¹⁶³. Douglas and coworker⁸⁴ were the first to develop a synthetic technique involving complexed Ti(IV) ion which undergo conversion to photocatalytically active titania (TiO_2) nanoparticles inside a chemically crosslinked cowpea chlorotic mottle virus (CCMV) capsid. The size and shape of TiO_2 nanoparticles are constrained by the interior surface of

the CCMV viral capsid. Although the resultant TiO₂-CCMV nanostructure showed effectiveness in the photobleaching of methylene blue (MB), they lack stability showing the apparent agglomeration through the photocatalytic reaction.

Recombinant rotavirus VP6 nanotubes were utilized as scaffolds for the synthesis of silver, gold, platinum and palladium nanoparticles on VP6 outer surface through strong (sodium borohydride) or mild (sodium citrate) chemical reduction. Those Pt-VP6 and Pd-VP6 nanobiomaterials were demonstrated to have catalytic activity for the glucose oxidation into gluconic acid¹¹⁷. In their studies, Pt- and Pd- functionalized VP6 nanotubes as catalysts result in 34% and 40% conversion of glucose respectively after 180 min, whereas the Pt and Pd nanoparticles without VP6 templates only show 11% and 29% glucose conversion.

M13 bacteriophage was also employed for the synthesis of metal nanoparticles for the catalytic reactions. For example, Ruthenium nanoparticles on M13 bacteriophage catalyzed a complete conversion of styrene to ethylbenzene after 1 hour¹²⁵. Belcher and coworker¹⁶⁴ reported the synthesis of small nanocrystalline materials 1% Rh/10% Ni@CeO₂ as catalysts to enhance the performance in the oxidative steam reforming of ethanol into hydrogen gas, achieving 100% conversion of ethanol at 300 °C with 60% H₂ in the product stream. Those biotemplated catalysts showed improved activity and stability for the ethanol reformation reaction.

Another work by Belcher's group¹²⁴ employed a genetically engineered M13 as template to co-assemble zinc porphyrins (photosensitizer) and iridium oxide hydrosol clusters (catalyst), and integrated the nanostructure into porous polymer microgels as an immobilization matrix for visible light-driven water oxidation.

All the above reports only stay in preliminary exploration stage, especially in the catalytic reaction part. There exists lack of thorough catalytic reaction studies, such as reaction kinetics, reaction mechanism, metal surface characterization, recyclability, or synthesis-structure-activity correlation. In addition, the demonstration of potential benefits of using viruses for nanocatalysts synthesis, such as improved catalytic activity has not been reported. For example, the special viral surface assembly properties either on inorganic surface or organic materials are highly attractive. The genetic modification of TMV coat protein provides improved metal decoration. In this dissertation, I present two novel nanocatalyst synthesis approaches by making full use of TMV's advantages, which will be introduced in detailed in the following chapters.

2. TMV-templated Pd Nanocatalysts for Dichromate Reduction

2.1. Introduction

Chromium is prevalent in industrial waste solutions in the U.S. (listed as the second most common inorganic contaminant in water^{48,49}), and the Agency for Toxic Substances and Diseases Registry (ATSDR) classifies Cr(VI) as the top 16th hazardous substance⁵⁰. Cr(VI) has been demonstrated to be hazardous to the public health due to its mutagenic and carcinogenic properties by inducing oxidative stress, DNA damage, apoptotic cell death and altered gene expression⁵². Catalytic reduction of hexavalent chromium (Cr(VI))^{11,165} provides a promising alternative to the existing non-catalytic treatments such as adsorption, biosorption, membrane filtration, ion exchange, and electrochemical treatment⁵¹.

Novel nanocatalysts have been applied for the waste water clean-up processes due to the advantages of high reaction efficiency and selectivity, low mas-transfer restrictions, low cost, and environmentally benign procedures^{166,167}. There have been many reports on the catalytic reduction of Cr(VI) by organic reductants by applying oxides⁶³ (TiO_2 ⁶⁴, aluminum oxide $\gamma\text{-Al}_2\text{O}_3$ ⁵⁷, goethite $\alpha\text{-FeOOH}$ ⁶⁵), nano-sized zero-valent iron⁶⁰, nano-sized mixed metallic particles⁶⁶, palladium

nano^{10,11}, mesoporous Al₂O₃-supported⁵⁷ or TiO₂-supported²⁶ Pd nanoparticles. Palladium (Pd) nanocatalysts are particularly important catalysts for the reduction of heavy metal pollutants^{10,11}.

While catalytic methods for waste stream treatment are well-known and numerous installations are in operation¹⁶⁸, there remain several technical challenges towards facile catalytic remediation of environmental hazards. First, heterogeneous catalyst synthesis faces several drawbacks in both catalyst preparation and reaction processing^{167,169}. A major drawback of heterogeneous catalysis is rapid deactivation of the catalyst, mainly due to poisoning, sintering or leaching. Also, the reaction activity and selectivity is apparently interfered by supports. Furthermore, heterogeneous catalysis synthesis is inherently unpredictable due to harsh preparation conditions and artifacts from supports. Second, homogeneous catalysts are difficult to separate from reaction products or recover for repeated use without further generating pollutants^{2,3}. Another catalytic system based on well-dispersed colloidal nanoparticles, so-called semiheterogeneous systems, is one of the most attractive alternatives. While combining the advantages of both homogeneous and heterogeneous catalysts, these systems also suffer from lack of stability and in-situ reaction monitoring^{10,170,171}.

Biological macro/supramolecules (e.g. DNA^{108,109}, peptides¹¹⁰ or proteins^{111,112}, bacteria^{113,114} and viruses^{140,172-175}) offer alternative templating materials toward

addressing these challenges inherent to inorganic synthesis procedures. Notably, a range of icosahedral viruses and protein cages have been employed to synthesize catalytic nanoparticles^{84,163,172}. Tubular viral nanotemplates were exploited for high density synthesis of catalytically active nanoparticles. Specifically, precisely spaced thiol functionality from genetically modified tobacco mosaic virus (TMV) is harnessed to provide facile surface assembly and enhanced palladium nanoparticle synthesis in high density. As shown in the Chimera model drawing of Figure 2.1(a), TMV is a naturally occurring rigid nanotube with 300 nm length, 18 nm diameter and 4 nm inner channel^{129,176}. This simple and robust structure is defined by 2130 identical coat proteins helically wrapped around a 6.4 kb single stranded genomic mRNA¹⁷⁷. Importantly, TMV possesses many unique physical and chemical attributes that can be harnessed for facile nanocatalyst synthesis. First, TMV's structure is well-defined and remarkably stable in a wide range of conditions including high temperature (up to 90 °C), broad pH values (2~10) and even in non-aqueous solvents such as 80 % ethanol, methanol and DMSO^{130,133}. Recognizing these attributes, wildtype TMV has been extensively enlisted for nanoparticle and nanowire synthesis toward a number of applications¹⁴⁰⁻¹⁴⁵ such as nanoelectronics. Second, small genetic modification can be routinely employed to confer precisely spaced functionalities on TMV surfaces via insertion of additional amino acids or

peptides¹³⁴⁻¹³⁷. Particularly, I utilized precisely spaced (horizontal spacing 1.8 nm, vertical 2.3 nm)¹³⁹ thiol groups displayed on the outer surface of each coat protein of TMV1cys (red dots in Figure 2.1(a))^{42,178-180} for simple surface-assembly and enhanced, preferential metal nanoparticle formation. Combined with safety (infectious to a handful of plants only), simple mass production and extensive knowledge, TMV thus provides attractive and unique advantages that can be harnessed as a templating material for synthesis of nanostructured metal catalysts.

In this chapter, I examine the catalytic activity of TMV-templated palladium nanoparticles for dichromate reduction for the first time. As shown in the schematic diagram of Figure 2.1(b), I first assembled TMV templates on gold surfaces by simply dipping gold-coated chips in TMV1cys solution. AFM image of Figure 2.1(e) clearly show that this simple dipping procedure yields dense near-monolayer TMV coverage. Next, these TMV chips are exposed to aqueous Pd precursor solution containing mild reducing agent to form Pd nanoparticles on TMV templates (Pd-TMV chip). AFM image of Figure 2.1(f) clearly shows that the Pd nanoparticles preferentially form on TMV templates with high surface density, while Figure 2.1(g) shows that Pd nanoparticle formation on gold surface is minimal in the absence of TMV templates. As shown in the schematic diagram of Figure 2.1(c) and the photograph of Figure 2.1(d), these Pd-TMV chips are

then directly immersed in dichromate solution for catalytic reduction, and the reaction kinetics is examined real time, in-situ via UV/vis spectrophotometry. These reaction kinetics studies provide strong evidence of catalytic activity, optimal reaction conditions and stability of the Pd-TMV nanocatalyst-viral complexes over several recycle reactions. Further, in-depth characterization via Grazing Incidence Small Angle X-ray Scattering (GISAXS) show uniform 11-12 nm diameter particles on TMV templates with minimal alteration upon catalytic reactions. Meanwhile, X-ray Photoelectron Spectroscopy (XPS) further provided chemical evidence for the presence, oxidation state and dense loading of palladium on the surface. Combined these results demonstrate a novel and facile strategy for nanostructured Pd catalyst synthesis based on surface-assembled viral templates. I envision that this simple approach for nanocatalyst synthesis could be readily applicable to other catalysis systems.

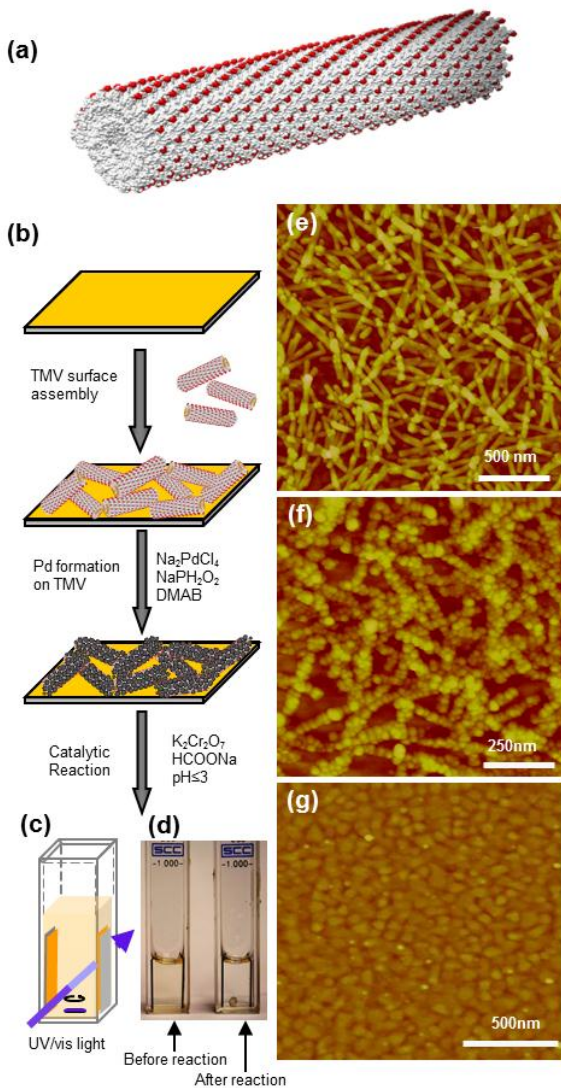


Figure 2.1. Schematic Diagram of TMV-templated Pd Nanocatalysts for Dichromate Reduction.

(a) Chimera model drawing of genetically modified Tobacco Mosaic Virus (TMV1cys). Red dots represent genetically inserted cysteine groups on the outer surface of each coat protein. (b) Schematic diagram of TMV-templated Pd Nanocatalysis. (c) Schematic diagram showing in situ monitoring of dichromate reduction in a quartz cuvette with UV/vis spectroscopy. (d) Photograph of dichromate reaction solutions before and after reaction showing the color change.

(e-g) AFM images of TMV assembled on clean gold surface (e), Pd-TMV complex on gold surface (f) and Pd chip without TMV templates (g).

2.2. Materials and Methods

2.2.1. Materials

Genetically modified TMV1cys was generously provided by Dr. James Culver, at the University of Maryland Biotechnology Institute, Center for Biosystems Research. Gold-coated silicon wafers with 1000 Å Au were purchased from Platypus Technologies (Madison, WI). Acetone, isopropanol and methanol were used for gold chip surface cleaning (all in HPLC grade, Fisher Scientific, Fair Lawn, NJ). Sodium tetrachloro-palladate (II) (Na_2PdCl_4) (99.998 %, Aldrich, St. Louis, MO) was used as the Pd precursor for Pd nanoparticle formation. Precursor reduction was conducted using sodium hypophosphite (NaPH_2O_2) (Sigma-Aldrich, St. Louis, MO). Potassium dichromate ($\text{K}_2\text{Cr}_2\text{O}_7$) (99.5%, Sigma-Aldrich) and sodium formate (HCOONa) (99 %, Fisher Scientific) were used in the dichromate reduction study.

2.2.2. Synthesis of TMV-templated Pd Nanocatalysts

(1)TMV1cys Surface Assembly on Gold Chips

The TMV drawing shown in Figure 2.1(a) were produced using the UCSF Chimera package (<http://www.cgl.ucsf.edu/chimera>) from the Resource for

Biocomputing, Visualization, and Informatics at the University of California, San Francisco¹⁸¹. The TMV structure (PDB ID: 2tmv)¹⁸² was obtained from the Research Collaboratory for Structural Bioinformatics Protein Data Bank (RCSB PDB, <http://www.pdb.org>)¹⁸³.

Gold-coated silicon wafers were cut into small chips (about 0.7 cm×2 cm) and sequentially cleaned with acetone, isopropanol and methanol each for 20 minutes, with thorough rinsing with deionized water between steps. After this organic solvent cleaning, the chips were dried under a stream of ultrapure nitrogen gas and then etched with plasma (Ernest F. Fullam Inc., Clifton Park, NY). Immediately after etching, the chips were incubated in 100 µg/ml TMV1cys in 0.01 M sodium phosphate buffer (pH 7) overnight at room temperature. After this TMV1cys binding, the chips (TMV chips) were thoroughly rinsed with deionized water, dried with N₂ gas again and stored at room temperature for further metallization.

(2) Palladium Nanoparticle Formation on TMV1cys Templates

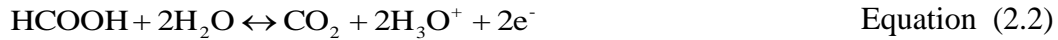
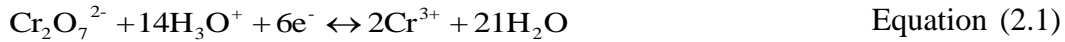
For the formation of Pd nanoparticles, TMV-assembled gold chips were immersed in freshly prepared aqueous solution containing 0.5 mM Na₂PdCl₄ precursor and 15 mM NaPH₂O₂ in dark for 20 min. The chips are thoroughly

rinsed in deionized water, dried with N₂ gas, and stored at room temperature for catalytic reactions (Pd-TMV chips).

2.2.3. Catalytic Activity for Dichromate Reduction

(1) Reaction Conditions

Potassium dichromate was the source of Cr(VI), while formic acid acted as the electron donor for dichromate reduction in an acidic environment. The coupled redox reactions are enumerated in Equations (2.1) and (2.2)¹⁸⁴. As shown in Figure 2.1(c) and (d), dichromate reduction reactions in 1 ml aqueous solutions containing K₂Cr₂O₇ (0.1 mM) and HCOONa (100 mM) were carried out in quartz cuvettes in the presence of chips fixed on the inner side walls and stirring at 600 rpm with a micro magnetic stirring bar (5 mm×2 mm, Fisher Scientific). The pH of reaction solution was adjusted to 3 by adding concentrated sulfuric acid. Dichromate reduction reactions with stirring speeds higher than 600 rpm show the same conversion rates as 600 rpm, which rule out the presence of external diffusion limitation under 600 rpm stirring speed condition, as shown in Section A3 of the Appendix. The reaction was monitored in-situ by EvolutionTM 300 UV/vis Spectrophotometer (Thermo scientific, Waltham, MA) every minute by taking the full absorbance spectra (250 nm-450 nm).



(2) Determination of Cr(VI) Conversion and Apparent First-Order Rate Constant

Cr(VI) Conversion: The characteristic absorption maximum of Cr(VI) at 350 nm was used to calculate Cr(VI) concentration, through correlating to a calibration curve constructed with absorbance of standard solutions. The calibration curve is shown in Section A2 of the Appendix. The extent of the catalytic reduction was expressed as conversion in percentage, which was calculated as Equation (2.3) shows.

$$\text{Conversion, \%} = \frac{([\text{Cr(VI)}]_0 - [\text{Cr(VI)}])}{[\text{Cr(VI)}]_0} \times 100\%$$
 Equation (2.3)

$[\text{Cr(VI)}]_0$: initial concentration

$[\text{Cr(VI)}]$: concentration at certain time point.

Apparent Rate Constants: To examine whether the dichromate reduction with excess amount of formic acid follows first-order kinetics behavior (Equation (2.4)), a linear regression of $\ln([\text{Cr(VI)}]/[\text{Cr(VI)}]_0)$ vs. reaction time (as shown in Equation (2.5) was carried out. The rate constant can be obtained from the

slope of the linear regression. With the elimination of external diffusion limitation, the observed first-order behavior reflects the kinetics behavior.

$$r = -\frac{d[Cr(VI)]}{dt} = k_1[Cr(VI)] \quad \text{Equation (2.4)}$$

$$\ln \frac{[Cr(VI)]}{[Cr(VI)]_0} = -k_1 t \quad \text{Equation (2.5)}$$

(3) Control and Recycle Study

For the comparison of catalytic activity, several controls were utilized, which are “gold chips”, “TMV chips”, “Pd chips”. “Gold chips” refer to the clean gold chips thoroughly cleaned by organic solvents and plasma etching. “TMV chips” represent the samples after TMV surface assembly on gold chips and before Pd metallization. “Pd chips” are prepared by following the same Pd metallization step on gold chips without surface-assembled TMV.

To examine the stability of the catalysts, Pd-TMV chips were recycled for two more catalytic reactions by simply immersing the used chips in the fresh reaction mixtures upon thorough rinsing by deionized water and drying without any further regeneration treatment.

2.2.4. Characterization of Pd Nanoparticles

(1) Atomic Force Microscopy (AFM)

AFM images were acquired using a Dimension 3100 series Scanning Probe Microscope (SPM) (Veeco, Woodbury, NY) in tapping mode with TAP-Al-50 AFM tips (Budget Sensors, Sofia, Bulgaria), and the images were analyzed using NanoScope software ¹⁸⁵.

(2) Grazing Incidence Small-Angle X-ray Scattering (GISAXS)

(In this chapter, the samples were prepared by me, but the data analysis was conducted by Amy K. Manocchi)

GISAXS measurements were conducted at the Advanced Photon Source (Argonne National Lab, Argonne, IL) BESSRC/XOR 12 ID-C beamline. Samples were mounted on a goniometer, and the beam irradiated on the sample at an incident angle (α_i) of 0.1°, as shown in Figure 3(a). The scattered X-rays were collected on a CCD detector (Rayonix, Mar165), with a sample to detector distance of approximately 2 m. Strong scattering and incident beam reflections in the α_f direction were blocked using a vertically mounted beamstop between the sample and detector. The beam energy was 8 keV.

For all GISAXS measurements, the scattering pattern was analyzed in terms of the scattering vector q_{xy} ¹⁸⁶. In these experiments, it was assumed that all Pd nanoparticles were spherical and dilute (meaning that the positions of individual particles are separated enough for scattering to be considered the sum of individual particle scattering). The relationship for scattered intensity, $P(q_{xy})$, for a single spherical particle of radius R , particle volume v and density ρ are given in Equation (2.6)¹⁸⁶.

$$P(q_{xy}) = \rho^2 v^2 \frac{9(\sin(q_{xy}R) - qR\cos(q_{xy}R))^2}{(q_{xy}R)^6} \quad \text{Equation (2.6)}$$

and scattering intensity, $I(q_{xy})$ of particles with size distribution, $n(R)$, reads

$$I(q_{xy}) = \rho^2 v^2 \exp\left[\frac{-(q_{xy}R_g)^2}{3}\right]^{187} \quad \text{Equation (2.7)}$$

$n(R)$ was calculated with Irena data fitting software, where the scattering curves were fit using the Maximum Entropy Method¹⁸⁸.

(3) X-ray Photoelectron Spectroscopy (XPS)

The XPS analysis was performed with XPS ESCA SSX-100 machine at the Center for Nanoscale Systems (CNS) of Harvard University (Cambridge, MA). The measurement was performed with a Al K α monochromatic X-ray source,

focused to a 600 μm diameter beam for high resolution spectra. For the individual peak energy regions, pass energy of 100 eV across the hemispheres was used. The chip samples were mounted on an aluminum cups prior to insertion into the ultrahigh vacuum chamber, and the pressure in the analysis chamber was in the range of 3×10^{-8} Torr during data collection. The peaks were fitted by a non-linear least square fitting program using a properly weighted sum of Lorentzian and Gaussian component curves¹⁸⁹.

2.3. Catalytic Activity and Control Study

As shown in Figure 2.2, I first demonstrate catalytic activity and simple in-situ reaction monitoring of TMV-templated Pd nanocatalysts for the dichromate reduction. For this, TMV-assembled gold chips (TMV chips) were coated with Pd nanoparticles via reduction of Pd precursor. The Pd-TMV chips were then immersed in reactant solution to catalyze dichromate reduction with formic acid, and the reaction was monitored by a UV/vis spectrophotometer every minute.

First, Figure 2.2(a) shows typical UV/vis absorption spectra of the reaction mixture during dichromate reduction reaction in the presence of Pd-TMV chips. Rapid decline of the Cr(VI) absorbance at 350 nm clearly indicates that reaction times of the order of 20 min ensured near-complete depletion of Cr(VI) due to the catalytic activity of Pd-TMV chips. Importantly, this result clearly illustrates

simple, real time in-situ reaction monitoring unlike in other systems where the catalysts interfere with Cr(VI) absorption spectra¹⁰. Thus, one of the advantages of this catalyst synthesis approach is that the surface assembly-based format enables in-situ monitoring.

Next, the catalytic performance of Pd-TMV chips were further examined and confirmed by comparing with several negative controls, as shown in Figure 2.2(b).

The changes in Cr(VI)'s characteristic absorption maximum at 350 nm were used to calculate conversion. As shown in the top curve with solid square symbol, the conversion of 0.2 mM Cr(VI) to Cr(III) was as high as 99.3 % after 20 min in the presence of Pd-TMV chips; 91 %, was reduced within the first 10 min. The curve with round symbols beneath the Pd-TMV curve represents the reaction with Pd chips prepared in the absence of TMV templates (AFM image of Figure 2.1(g)). Reaction in this case is clearly much slower; the conversion only reaches 40 % after 20 min. The “apparent” difference in the Pd amount between Pd-TMV and Pd chips is clearly reflected in this difference in catalytic activity. The other negative controls (TMV only chips and gold chips, represented by triangle and upside-down triangle symbol curves, respectively) which contain no Pd, show even smaller conversion rates than Pd chips. Finally, the bottom curve (with stars) shows no catalytic activity in the absence of chips; this continued to be the case

for several months (data not shown). Overall this clear difference in the conversion rate indicates the catalytic activity of Pd-TMV chips.

To further gain quantitative understanding and to explore the mechanism, linear regression analysis of the relationship between $\ln(C/C_0)$ and reaction time was conducted; the results are plotted in Figure 2.2(c). The slopes represent the first-order rate constants (see Theoretical Background). From the consistently high R^2 values for all the five cases (over 0.995), first-order reaction kinetics are clearly followed. Notably, the difference in the conversion rate between Pd-TMV chips and all the negative controls is more obvious in Figure 2.2(c). Specifically, Pd-TMV chips have the highest rate constant, 0.25 min^{-1} while Pd chips show only 0.02 min^{-1} , or 12 fold lower than that of Pd-TMV chips. TMV only chips and gold chips also showed very low rate constant, only 0.02 min^{-1} and 0.01 min^{-1} respectively.

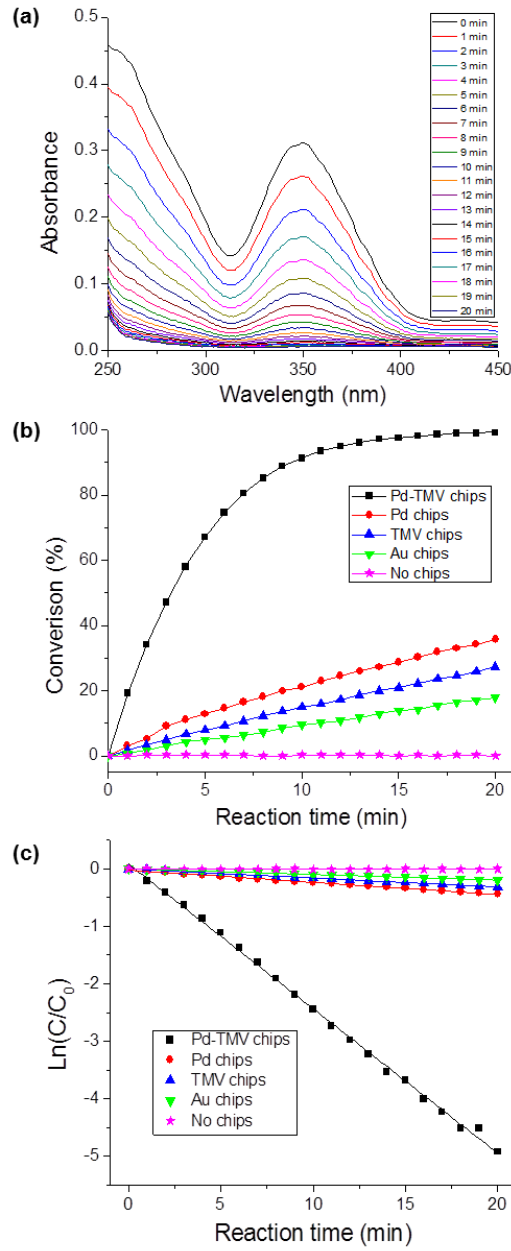


Figure 2.2. Dichromate Reduction Reaction by Pd-TMV Chips and Control Studies

(a) UV/Vis absorption spectra of dichromate reduction solution over time. (b) Comparison of catalytic activity between Pd-TMV chips and negative controls (Pd chips, TMV chips, Au chips and no chips). (c) $\ln(C/C_0)$ vs. reaction time

(symbols: experimental data; solid lines: Eqn. 2.5 with rate constant determined by results linear regression).

Both the conversion curves comparison and rate constant analysis shown in Figure 2.2 amply demonstrate the catalytic activity and several advantages of utilizing surface-assembled TMV template for Pd nanocatalyst synthesis. Combined these results clearly indicate that catalytic activity of TMV-templated Pd nanoparticles is substantially higher than any negative controls examined.

2.4. Recycle Studies for Pd-TMV Chip and Pd Chip

Next to further examine the stability and reusability of these Pd-TMV catalysts for dichromate reduction, I conducted recycle study as shown in Figure 2.3. For this, thoroughly rinsed Pd-TMV or Pd chips were directly utilized for the next reaction cycle after each batch reaction without any other regeneration treatments. The three top curves with solid symbols in Figure 2.3(a) represent recycle results of Pd-TMV chips, indicating that Pd nanoparticles on TMV templates retained most catalytic activity throughout three reaction cycles. All three cycles went to near-completion within 20 min reaction period, and the conversion rate remained almost the same. In contrast, three near-straight conversion lines with empty symbols at the bottom of Figure 2.3(a) show much slower reduction rate by Pd chips, which further decreases substantially upon repeated use. After two reaction cycles, the conversion after 20 min was only 24.5 %. Furthermore, conversion of

the third cycle was even as low as 18.8 %, similar to the gold chips (without any Pd) case.

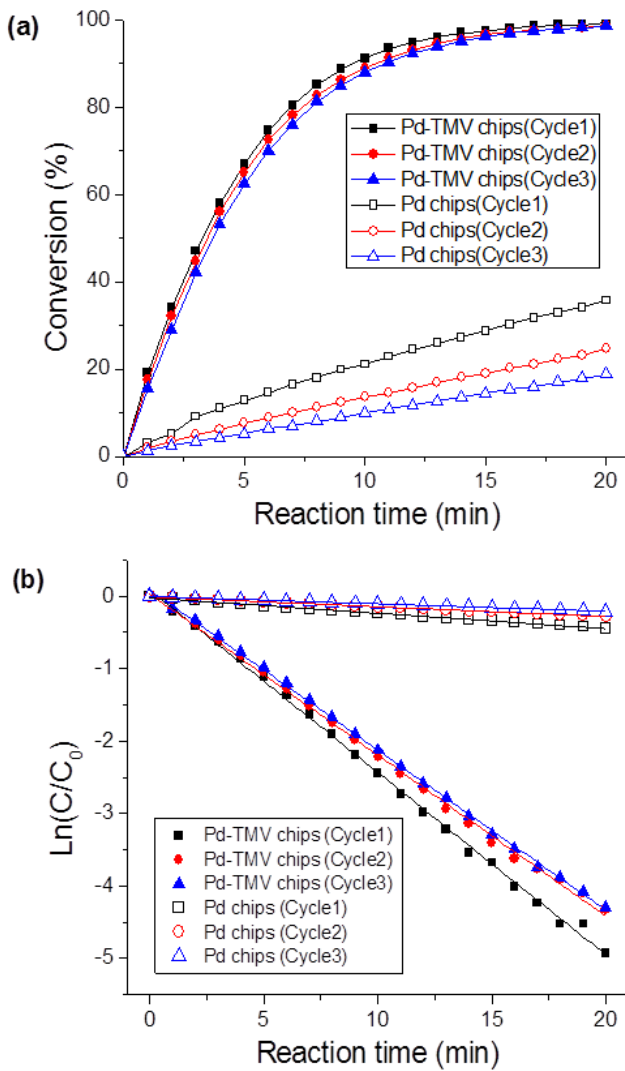


Figure 2.3. Recyclability Study

(a) Dichromate reduction conversion from three reaction cycles with Pd-TMV chip and Pd chip. (b) Linear regression plot.

In order to gain further quantitative understanding on the reaction rates, linear regression analysis was carried out again, as shown in Figure 2.3(b). Importantly, all three curves from Pd-TMV chips strictly follow first-order batch reaction kinetics again. The rate constants of three cycles were shown to be very close, where the second and third cycles decreased slightly compared to the first cycle, from 0.25 to 0.22 min^{-1} . This retention of 88 % in the reaction rate upon three batch reactions without any regeneration treatment clearly illustrates the high stability of Pd-TMV complexes for dichromate reduction under the conditions employed. Lee et al ¹⁵⁷ also found that introduction of thiol groups onto TMV surface can help enhance its metal binding ability and stability. On the contrary, the rate constant from Pd chips decreased rapidly from 0.02 min^{-1} in first cycle to 0.01 min^{-1} , a factor of two lower, in third cycle. This suggests that the Pd on gold without TMV templating is unstable.

2.5. Grazing Incidence Small-Angle X-ray Scattering (GISAXS)

(For the results presented in this section, I prepared samples, and Amy K. Manocchi carried out the sample measurement and data analysis).

As shown in Figure 2.4, an in-depth characterization of the Pd-TMV chips was carried out via Grazing Incidence Small-Angle X-ray Scattering (GISAXS) to further examine the Pd particle size and Pd-TMV complex structures. For this, thoroughly rinsed and dried TMV chips as well as Pd chips and Pd-TMV chips before and after the dichromate reduction were examined with GISAXS at the Advanced Photon Source of Argonne National Laboratory. As shown in the schematic diagram of GISAXS in Figure 2.4(a), a 8 keV X-ray beam is irradiated onto the sample at a small incident angle ($\alpha_i=0.1^\circ$) and the scattering pattern recorded at small angle ($\alpha_f < 2^\circ$) on a 2D CCD detector. The scattering patterns are analyzed by making a line-cut of the scattering pattern in the in-plane direction, as shown by a solid line in Figure 2.4(d) and plotting the intensity (I) as a function of q_{xy} (both in log scale). A data analysis is conducted on each line-cut to provide a statistically meaningful estimate of the particle size and its distribution due to the large sample area exposed to the X-ray^{145,186,187}.

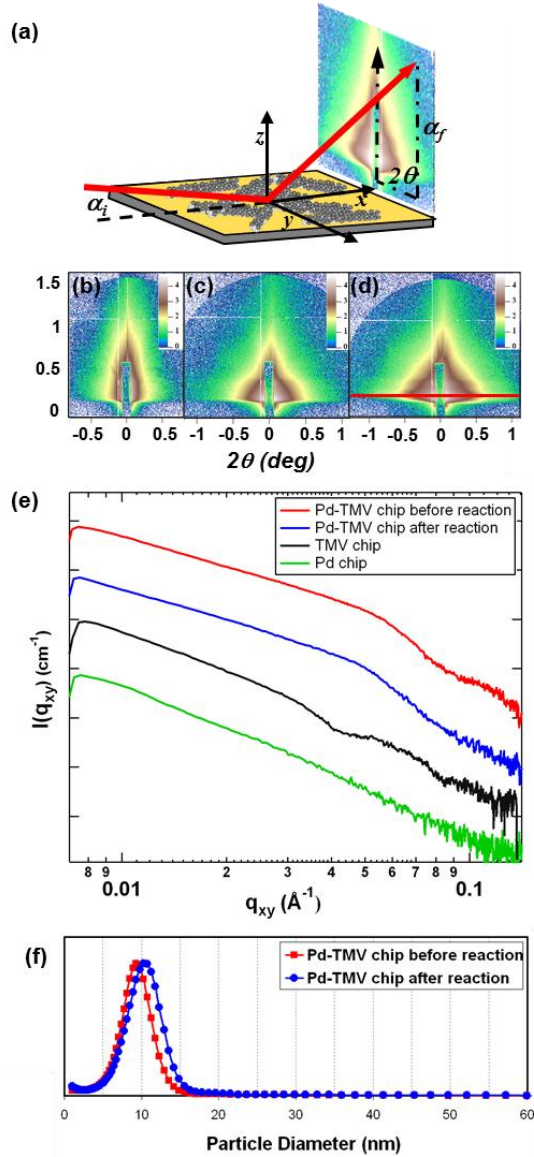


Figure 2.4. Particle Size and Distribution Analysis by GI-SAXS.

(a) Schematic diagram of GISAXS. (b-d) X ray scattering pattern of TMV only chip(b), Pd chip(c) and Pd-TMV chip(d). (e) Line-cut plots of scattering intensity vs. q_{xy} for Pd-TMV chip before and after reaction, TMV only chip and Pd chip without TMV templates. (f) Pd particle size distribution plot for Pd-TMV chip before and after reaction.

As shown in Figures 2.4(b-d), the chip samples examined via GISAXS produced substantially different scattering patterns indicating several important aspects. First, Figure 2.4(b) shows that surface-assembled TMV1cys shows strong scattering in the out-of-plane direction (at $2\theta=0$), characteristic of the rod shape of TMV¹⁴⁵. In contrast, Figure 2.4(c) for the Pd only chip shows strong isotropic scattering in a wider area, rising from spherical Pd nanoparticles. Finally, the Pd-TMV chip in Figure 2.4(d) also shows strong isotropic scattering characteristic of spherical Pd nanoparticles in addition to strong out-of-plane (vertical) scattering characteristic of TMV nanotubes. In contrast to the Pd only chip, the isotropic scattering in Figure 2.4(d) exhibits intensity oscillations in the out-of-plane direction, indicating existence of a layer composed of Pd-TMV complex with thickness of about 30 nm calculated from the period of the oscillation¹⁹⁰. Importantly, this scattering pattern indicates that the Pd nanoparticle scattering is significant, and can be distinguished from the TMV scattering for particle size calculations. In summary, these three scattering patterns attest to the utility of GISAXS in the in-depth characterization of these Pd-TMV nanocomplex structures.

As shown in Figure 2.4(e), these findings are more clearly confirmed via line-cut plots of intensity vs. q_{xy} . The two top curves show line-cuts for a Pd-TMV chip before (dash curve) and a Pd-TMV chip after (dash dot curve) the dichromate

reduction, while the third TMV curve shows oscillation at higher q_{xy} values, typical of the monodisperse TMV nanotubes¹⁴⁵. First, the two top curves look nearly identical, and exhibit a distinct Guinier knee (a sudden rise then fall in intensity) at similar q_{xy} locations, arising from Pd nanoparticles with similar sizes. As calculated through a size analysis, the average Pd particle diameter was approximately 11.5 nm before reaction, and 12.7 nm after reaction. This indicates minimal change in the Pd particle size as well as the stability of Pd-TMV complexes upon the catalytic reaction. The slight difference in average particle size may be within a sampling error: minor differences in the two chips arising from two different Pd-TMV chips for GISAXS analysis. Importantly, the clear difference in the line-cut curves between the TMV chip (dot curve) and Pd-TMV chip (dash curve and dash dot curve) illustrates the presence and retention of Pd nanoparticles upon Pd nanoparticle formation and catalytic reactions respectively. Finally, the bottom curve (solid line) representing the Pd chip shows highly polydisperse (no distinct Guinier knee) and significantly fewer and larger Pd nanoparticles, as evident by ~20 fold less initial scattering intensity as compared to the Pd-TMV chip (result not shown).

Figure 2.4(f) shows normalized particle volume distributions on the Pd-TMV chips for before and after the dichromate reduction shown in the top two curves of Figure 2.4(e). For this, only high q region ($q_{xy} = 0.03\text{-}0.09 \text{ \AA}^{-1}$) of scattering

curves were analyzed, and the small q region where the power law scattering appears is neglected because the power law scattering rise from a hierarchical structure of Pd particle assembly, or a shape of TMV. These distribution curves show that Pd particles are quite uniform in the 11 nm diameter range, and the overall average size doesn't change significantly upon the catalytic reaction. Combined these GISAXS results clearly show the substantial amount, retention and particle size distributions of palladium nanocatalysts on TMV templates.

2.6. X-ray Photoelectron Spectroscopy

As shown in Figure 2.5, I further examined the presence and oxidation states of TMV-templated Pd nanocatalysts via XPS before and after the dichromate reaction. For this, four types of chips (Au, Pd, TMV and Pd-TMV chips) were thoroughly rinsed, dried and examined with ESCA SSX-100 XPS.

First, Figure 2.5(a) displays XPS spectra in the range of 361~322 eV binding energy in high resolution. The top curve represents the spectrum of the gold chip (sample (I)) that shows two typical Au 4d_{3/2} and Au 4d_{5/2} peaks with binding energy at 352.36 and 334.47 eV respectively. No Pd was observed for this gold chip only case. The second spectrum is from TMV chip (sample (II)), which shows very similar peak pattern and position with strong gold peaks. However, slightly lower intensity of gold peaks for TMV chip implies that there may be a

thin layer of TMV1cys exists over gold chip surface. The other two spectra show Pd 3d core level feature from Pd-TMV chips before and after reaction (sample (III) and (IV)). In contrast to the top two spectra for the gold chip and TMV chip, both Pd-TMV chip spectra show apparent Pd 3d_{3/2} peak with binding energy at about 341 eV, clearly showing the presence of Pd substance. The Pd 3d spectra of Pd-TMV chips before and after dichromate reduction appear quite similar. Particularly, the position of Pd 3d_{3/2} peak shows no significant shift after the reaction, which indicates no meaningful changes in the chemical state under the reaction conditions employed. This minimal change in the Pd peak position further suggests the stability of Pd-TMV chips during the catalytic reactions. In addition, the intensity of Au 4d_{3/2} peak from Pd-TMV chips is clearly much weaker than that of the gold only case for many samples examined. This suggests that the gold surface is covered with a 30 nm film of Pd-TMV complex, since X-ray can only penetrate through the top 1~10 nm surface.

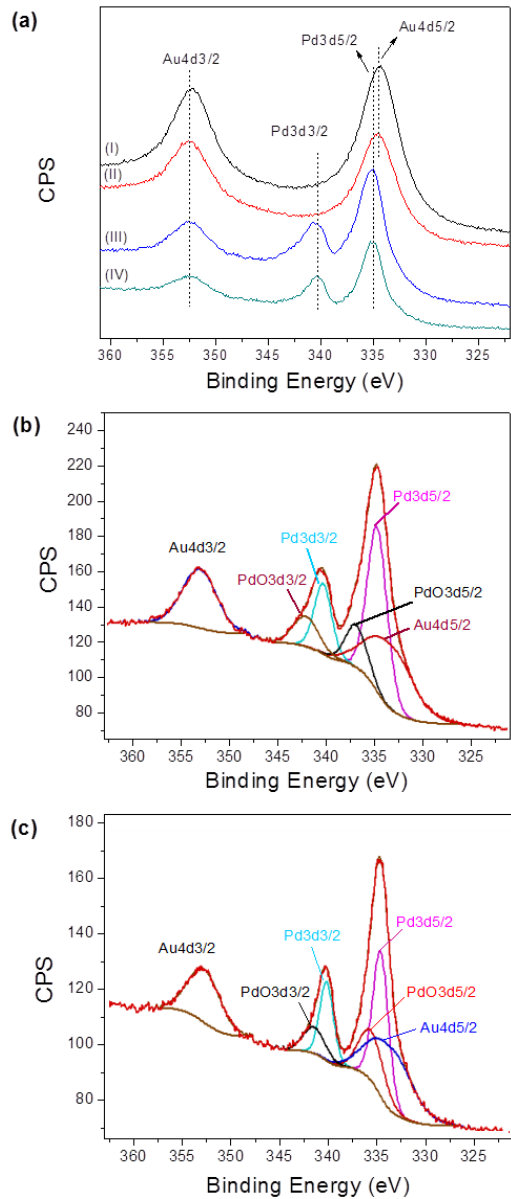


Figure 2.5. XPS Analysis of Gold Chip, TMV Chip and Pd-TMV Chips before and after Reaction

(a) High resolution XPS spectra with Pd 3d features. (I) Gold chip, (II) TMV chip, (III)Pd-TMV chip before reaction, (IV) Pd-TMV chip after reaction (b) Peak fitting for Pd 3d photoelectron spectrum of Pd-TMV chip before reaction.(c) Peak fitting for Pd 3d photoelectron spectrum of Pd-TMV chip after reaction

Next, in order to further examine palladium's chemical state distribution and total palladium amount based on gold, peak fitting analysis was carried out. Figure 2.5(b) and (c) show the peak fitting results for Pd-TMV chips before and after the reaction in the bottom two curves shown in Figure 2.5(a). Slightly asymmetric Pd 3d_{3/2} peak indicates the coexistence of metallic Pd and PdO. Thus the Pd3d_{3/2} peak was split into peaks for Pd and PdO by non-linear fitting to estimate the metallic Pd percentage ¹⁸⁹. Similarly, the Pd3d_{5/2} peak is heavily overlapped with Au4d_{5/2} peak at 335 eV binding energy, so Pd3d_{5/2} for both metallic Pd and PdO and also Au4d_{5/2} were involved for the peak fitting analysis. The surface atomic concentration of Pd was obtained from the peak area ratio of Pd/(Pd+Au).

Table 2.1. XPS Pd3d and Au4d binding energies (eV) and XPS derived Pd/(Au+Pd) atomic percentage for Pd-TMV chips before and after reaction

Name	Binding Energy, eV		Pd/(Pd+PdO), %		Pd/(Pd+Au), %	
	Before	After	Before	After	Before	After
	Reaction	Reaction	Reaction	Reaction	Reaction	Reaction
Pd Pd 3d _{3/2}	340.52	340.39				
PdO Pd 3d _{3/2}	342.18	341.62				
Pd Pd 3d _{5/2}	335.18	335.05				
PdO Pd 3d _{5/2}	337.27	335.98	69	65	60	59
Au Au 4d _{5/2}	333.95	334.09				
Au Au 4d _{3/2}	352.7	352.47				

Table 2.1 summarizes the binding energies of Pd3d and Au4d, corresponding metallic Pd percentage and surface atomic Pd concentration. The peak fitting results show that metallic Pd/(Pd+PdO) percentage of Pd-TMV chips before and after reaction are more than 65 %, suggesting that Pd is mostly at the metallic state. Furthermore, the metallic Pd % after dichromate reduction (65 %) is slightly lower than that of chip before reaction (69 %), showing only a minimal change in the oxidation state. Meanwhile, the surface atomic Pd concentration Pd/(Pd+Au) after reaction (59 %) remained almost the same as before reaction (60 %), indicating that most Pd substance stayed on the surface of TMV assembled on the gold chip, without significant decomposition of the Pd-TMV complex or leaching of Pd nanoparticles into the reaction solution. Combined these XPS results provide strong chemical evidence for the presence of palladium substance, chemical states as well as the stability of Pd nanoparticles on the TMV-assembled gold chips upon the catalytic reaction.

2.7. Conclusions

In this chapter, the catalytic activity of TMV-templated palladium nanocatalysts for dichromate reduction was examined. This surface-assembly based format enables simple in-situ real time monitoring of the catalytic dichromate reduction, allowing for rapid screening of reaction conditions. Reaction kinetics studies clearly demonstrated substantial catalytic activity over any other negative controls

examined. Moreover, TMV-templated palladium nanocatalysts retained significant catalytic activity in the recycle study, indicating the stability of viral-metal nanoparticle complexes under the reaction conditions employed in this study. Atomic force Atomic Force Microscopy (AFM) and Grazing Incidence Small-Angle X-ray Scattering (GISAXS) were utilized to probe Pd nanoparticle size and distribution, which further indicated the stability of Pd-TMV complexes upon catalytic reactions. Meanwhile, XPS provided chemical evidence for the presence of Pd and its oxidation states. In the following chapter, the kinetics of Pd catalyzed dichromate reduction under a wide range of reaction conditions, the synthesis-structure-activity relationship will be further examined.

3. Investigation on the Catalytic Reduction Kinetics of Hexavalent Chromium by Viral-templated Palladium Nanocatalysts

3.1. Introduction

In Chapter 2, the catalytic activity, recyclability and stability of TMV-templated palladium nanocatalysts for dichromate reduction, was reported for the first time. Only one synthesis condition and one reaction condition was examined in Chapter 2. The systematic reaction kinetics study of the Pd catalyzed dichromate reduction by formate still remains absent. Additional experiments were undertaken to develop further understanding of the catalyst synthesis-structure-activity relation, and the reaction kinetics, and to identify optimal reaction conditions and processes.

In this chapter, I aim at the surface catalyzed reaction mechanism study, kinetics and the catalyst synthesis-structure-activity relationship for dichromate reduction. The results suggest that Pd catalyzed dichromate reduction follows a Langmuir-Hinshelwood surface reaction mechanism, with a formic acid binding constant substantially greater than that of dichromate ion (~263 times). Furthermore, (1) with synthesis conditions optimized, viral-templated Pd nanocatalysts show 68%

higher specific catalytic activity (per unit Pd mass) than commercially available 5% Pd/C catalysts. (2) Pd nanoparticle size, loading density and catalytic activity of viral-templated Pd nanocatalysts can be tuned by changing chemical composition (e.g. Pd and reducer concentrations) during synthesis under mild aqueous conditions. At the same time, larger Pd particles exhibited higher catalytic activity for dichromate reduction with formic acid, per unit Pd surface area, suggesting size-dependent behavior of Pd catalyst for dichromate reduction.

3.2. Materials and Methods

3.2.1. Materials

The same as in section 2.2.1.

3.2.2. Synthesis of TMV-templated Pd Catalysts

The synthesis method for the Pd-TMV catalyst chips is similar to section 2.2.2 with minor modification. Briefly, clean gold chips were incubated in aqueous 100 $\mu\text{g/ml}$ TMV1cys solution for surface assembly, which yields consistently dense near-monolayer surface coverage. These TMV-assembled chips were then exposed to various concentrations of Na_2PdCl_4 precursor solutions in the presence of various concentrations of NaPH_2O_2 as reducer for 20 min under ambient

conditions. These Pd-TMV chips were then thoroughly rinsed with deionized water, dried, and stored for the reaction and characterization studies.

3.2.3. Comparison with Commercial Pd/C Catalysts

For direct comparison with Pd-TMV chip catalysts, 0.0023 g commercial 5% Pd/C catalysts were immersed in 40 ml of the standard dichromate solution (containing 0.1 mM K₂Cr₂O₇ and 100 mM NaCOOH, and with the pH adjusted to 3). The reaction rate was then closely monitored. At each time point (every one minute), a small volume of the reaction solution was removed and filtered with a syringe filter (Pore size=0.22 µm, Diameter=13 mm, Polypropylene Housing, VWR); the absorbance of the supernatant at 350 nm was measured.

For the study of dichromate reduction catalyzed by Pd-TMV chip catalysts, 1 ml of 0.1 mM K₂Cr₂O₇ and 100 mM NaCOOH in water were carried out in quartz cuvettes in the presence of Pd-TMV chips under vigorous stirring (stirring speed=600 rpm), the same condition as described in Section 2.2.3. The TMV-templated Pd nanocatalysts have Pd nanoparticles with diameter of 3.6 ± 0.4 nm and Pd loading of 4.0 µg Pd/g chip. The reaction was monitored in-situ by EvolutionTM 300 UV/vis Spectrophotometer every minute by taking the full absorbance spectra (250 nm-450 nm).

For comparison purposes, the dichromate reduction rates catalyzed by both catalyst systems, 5% Pd/C and Pd-TMV chips, were each normalized by the Pd metal contents (surface area); accordingly, apparent first-order rate constants, k' _{app}, are expressed in units of L/(g Pd·min).

Experiments were undertaken at 5, 15, 25 and 35 °C in order to determine the activation energies E_a (kJ/mol) for dichromate reductions catalyzed by these two Pd catalyst systems. As discussed in section 2.2.3, under the aforementioned conditions, the reaction appears to follow pseudo first-order kinetics (see Figure 2.2). Activation energies were obtained by fitting the Arrhenius Equation¹⁹¹ to curves of $\ln k'$ _{app} vs 1/T (see Figure 3.6), i.e.:

$$\ln k'_{\text{app}} = -E_a/RT + \ln A \quad \text{Equation (3.1)}$$

where A is the pre-exponential factor, and R is the universal gas constant 8.314 J/(mol·K).

3.2.4. Effect of Catalyst Synthesis Conditions on the Catalytic Activity

In order to examine the effect of catalyst synthesis conditions on the catalyst properties, the Pd metallization of TMV biotemplates with various concentrations of precursor Na₂PdCl₄ (0.25, 0.5, 2 and 5 mM) and reducer NaPH₂O₂ (5, 15, 30,

45 and 55 mM) were carried out. Three groups of Pd metallization conditions were employed for the synthesis, as shown in Figure 4(a).

The reactivity of catalysts from various synthesis conditions was studied by measuring the initial dichromate reduction reaction rates r_0 (mmol/(m²·min)), which was obtained from the slope of the dichromate conversion vs. time plots during the initial reaction period (Figure 2.2, Figure A3 in the Appendix), and further normalized by the total surface area (A) of Pd nanoparticles acquired via GISAXS and ICP measurements. The total surface area of Pd nanoparticles on Pd-TMV chip catalysts is calculated according to Equation 3.2:

$$A = \frac{m}{\rho \frac{4}{3}\pi R^3} 4\pi R^2 \quad \text{Equation (3.2)}$$

(A: total Pd surface area; m: Pd mass; ρ: density of metallic Pd; R: diameter of Pd nanoparticles; the Pd nanoparticles are approximated as spherical.)

Pd particle sizes (R) were characterized by Grazing Incidence Small Angle X-ray Scattering (GISAXS) and the Pd loading amount from each sample (m) was determined by Inductively Coupled Plasma Optical Emission Spectrometry (ICP-OES).

For these synthesis condition effect studies, the reactions were all carried out in the standard dichromate reduction reaction condition (0.1 mM K₂Cr₂O₇ and 100 mM NaCOOH, at pH 3 and 25 °C).

3.2.5. Grazing Incidence Small Angle X-ray Scattering (GISAXS)

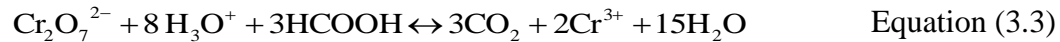
The measurement and data analysis in this chapter are the same as section 2.2.4.

3.2.6. Inductively Coupled Plasma Optical Emission Spectrometry (ICP-OES)

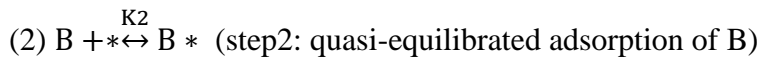
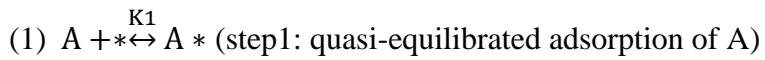
The exact amount of Pd loading on TMV-templated Pd nanocatalysts was measured by high performance ICP-OES. For this, the Pd-TMV chips were dipped into 1 ml aqua regia solution (HCl : HNO₃ (v:v) = 4:1) for acid digestion. After complete dissolution of Pd-TMV complex for about 5 min, the acid-digested solutions were further diluted by adding 2 ml deionized water. The samples were analyzed by Perkin Elmer 7300 ICP-OES (PerkinElmer Inc., Waltham, MA).

3.2.7. Kinetics Modeling

This section focuses on the kinetics of Pd-catalyzed dichromate reduction by formic acid. The overall catalytic redox reaction can be expressed as follows:



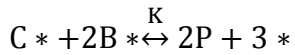
It is assumed here that the elementary steps are those that follow ([A] represents $[Cr_2O_7^{2-}]$, [B] represents $[HCOOH]$, [*] represent the concentration of vacant active chemisorption sites on the solid catalysts surface, $[C^*]$, $[D^*]$ and $[P^*]$ are those of reaction intermediates, and [P] represents the product Cr(III) ion)). It should be noted that the pH value of all reaction conditions studied is set as the same, pH=3. Thus, the effect of pH ($[H_3O^+]$) on the initial reaction rate was not examined.



Based on different elementary steps as rate determining steps, the overall rate expressions were derived, as shown in Section A1 of the Appendix. After fitting the experimental data with several derived kinetic expressions, the one based on

the assumption that step 3 is rate determining step (RDS) (for which the derivation is detailed below) was found to be the most suitable one. The fittings over other kinetic expressions based on other assumptions either obtain unreasonable parameters (negative value) or lower R_2 value, as shown in Section A1 of the Appendix. The derivation will be introduced in detail below.

Since step 3 is assumed to be rate determining step (RDS), equilibrium steps (4)-(6) can be combined, as shown below.



$$K = \frac{[P]^2 [*]^3}{[C *][B *]^2}$$

The overall number density of adsorption sites is represented by $[*]_0$, which includes both vacant ($[*]$) and occupied ($[A^*]$ or $[B^*]$) adsorption sites on the catalyst surface, as shown below.

$$[*]_0 = [*] + [A *] + [B *] = [*] + K_1[A][*] + K_2[B][*]$$

$$[*] = \frac{[*]_0}{1 + K_1[A] + K_2[B]}$$

$$[A *] = [*]_0 \theta_A = K_1[A][*] = \frac{K_1[A][*]_0}{1 + K_1[A] + K_2[B]} \quad \text{Equation (3.4)}$$

$$[\text{B}^*] = [*]_0 \theta_B = K_2 [\text{B}] [*] = \frac{K_2 [\text{B}] [*]_0}{1 + K_1 [\text{A}] + K_2 [\text{B}]} \quad \text{Equation (3.5)}$$

where θ_A, θ_B (theta A and theta B) are the surface coverage of $[\text{Cr}_2\text{O}_7^{2-}]$ (A) and $[\text{HCOOH}]$ (B) respectively. K_1 and K_2 are the adsorption equilibrium constants for $[\text{Cr}_2\text{O}_7^{2-}]$ and $[\text{HCOOH}]$.

The overall reaction rate, which is equal to the forward rate of the rate determining step (step 3), can be expressed as below:

$$\begin{aligned} r &= -\frac{d[K_2\text{Cr}_2\text{O}_7]}{dt} = k_3 [\text{A}^*][\text{B}^*] \\ &= k_3 [*]_0^2 \theta_A \theta_B \\ &= k_3 [*]_0^2 \frac{K_1 [\text{A}] K_2 [\text{B}]}{(1 + K_1 [\text{A}] + K_2 [\text{B}])^2} \end{aligned} \quad \text{Equation (3.6)}$$

r is the dichromate reduction reaction rate ($r = -\frac{d[\text{Cr}_2\text{O}_7^{2-}]}{dt}$, mmol/(L·min)), and $[\text{A}]$ and $[\text{B}]$ are the concentrations of $[\text{Cr}_2\text{O}_7^{2-}]$ and $[\text{HCOOH}]$ respectively. $[*]_0$ represents the number density of all adsorption sites (vacant and occupied) on the catalyst surface. The initial concentrations of both $[\text{A}]$ and $[\text{B}]$ are independent variables in the model fitting procedure. There are three unknown parameters: P_1 , P_2 and P_3 .

The TMV-templated Pd catalysts were synthesized with 0.25 mM Na₂PdCl₄ and 15 mM NaPH₂O₂, with 20 min metallization. In the first series of experiments (Figure 3.2(a)), the initial NaCOOH concentration was varied in the range 0-200 mM with initial K₂Cr₂O₇ concentrations as constants (0.05, 0.1 and 0.3 mM). In a second series (Figure 3.2(b)), the NaCOOH concentration was fixed at 30, 50 and 120 mM; and that of K₂Cr₂O₇ was varied in the range 0-0.5 mM. The initial pH was measured by pH meter. At pH 3, the concentration of [HCOOH] was calculated by the “Henderson-Hasselbalch” equation, i.e. pH=pKa+log([COOH⁻]/[HCOOH]). Thus, [HCOOH]=0.85×([HCOOH]+[COOH⁻]) under pH 3 condition. Initial reaction rates r were obtained from the slope of the dichromate concentration vs. time plots during the initial reaction period (i.e. initial rate

$$r = \frac{dc}{dt} = \frac{\Delta c}{\Delta t} = \frac{c_{(t=1\text{min})} - c_{(t=0\text{min})}}{(t_{1\text{min}} - t_{0\text{min}})}.$$

3.3. Chip Removal Study: Heterogeneous Surface Reaction

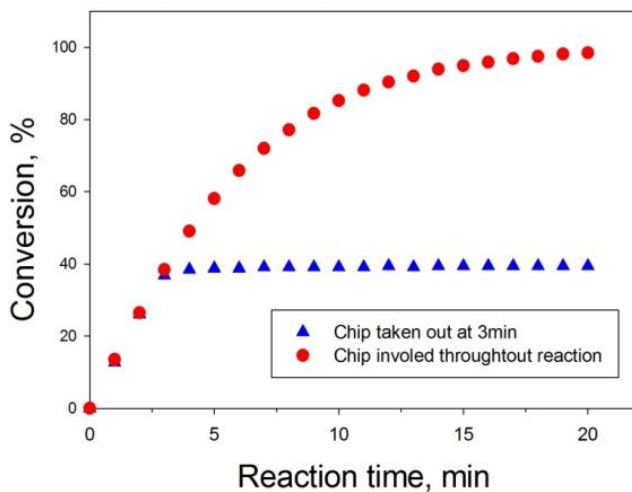


Figure 3.1. Surface Reaction Confirmation by Simple Chip Removal Study

The TMV-templated Pd Catalysts synthesis condition: 0.5 mM Na₂PdCl₄, 15 mM NaPH₂O₂, 20min metallization. The dichromate reaction condition: 0.1 mM K₂Cr₂O₇, 100mM NaCOOH, pH=3, at 25 °C.

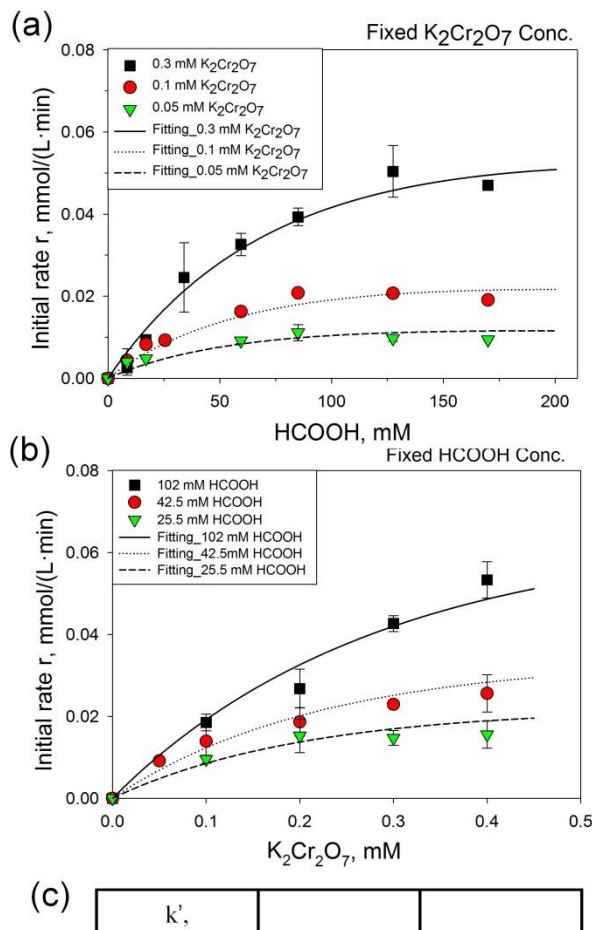
As part of the study of catalytic kinetics, viral-templated palladium (Pd) nanoparticles chips were removed at 3 minute from dichromate reduction experiments; see Figure 3.1, which compares results with and without chip removal. Absorbance at 350 nm of the reaction solution was measured minute by minute.

The data in Figure 3.1 make it clear that dichromate reduction ceased upon chip removal; when the Pd-TMV chip was present throughout experiment, the reaction proceeded to completion. This clearly confirms that the reaction takes place on

the surface of the viral-templated Pd nanoparticles. Notably, this is in direct contrast to the results of the study of the Suzuki coupling reaction (see Chapter 5), which continued subsequent to chip removal, consistent with the generally accepted leaching-based reaction mechanism⁶⁸. In addition, cease of dichromate reduction upon chip removal here confirms that: (1) Pd-TMV complexes are robust and highly stable under the acidic reaction environment; (2) the surface-assembled format enables simple catalyst recovery and reaction mechanism study, and further confirms the validity of the chip removal study for the Suzuki reaction. In summary, this simple chip removal study clearly indicates the surface-originated heterogeneous nature of the dichromate reduction by viral-templated Pd nanocatalysts.

3.4. Kinetics Modeling

Next, the reaction kinetics of dichromate reduction catalyzed by viral-templated Pd chips was studied more extensively; results are shown in Figure 3.2. As described in section 3.2.7, a few series of reactions were carried out with Pd-TMV chips possessing identical particle diameter ($d=12.4$ nm) and surface Pd loading (4.7 μg Pd/g chip).



(c)

k' , mol/(L min)	K_1 , L/mol	K_2 , L/mol
6.7×10^{-4}	1475	5.6

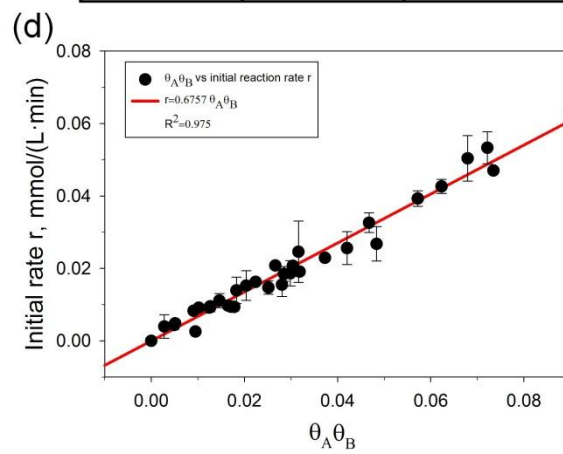


Figure 3.2. Langmuir-Hinshelwood Kinetics of Dichromate Reduction.

(a). Dependence of the initial reaction rate r_0 on the initial concentration of NaCOOH with fixed $K_2Cr_2O_7$ concentration. (b) Dependence of the r_0 on the initial concentration of $K_2Cr_2O_7$ with fixed NaCOOH concentration. (c) Rate constants and adsorption equilibrium constants of both reactants. (d) The initial rate r , (mmol/(L·min)), is plotted against $\theta_A\theta_B$ according to the Eqn. (9). The catalyst synthesis condition: 0.25 mM Na_2PdCl_4 , 15 mM $NaPH_2O_2$, 20min metallization.

As shown in Figure 3.2(a) and (b), the point symbols represent experimental data and solid lines were derived based on using Equation (3.6) and three unknown parameters (k , K_1 and K_2) fit to the experimental data. Both Figure 3.2(a) and (b) show that the initial reaction rate depends on the concentration of both reactants. All curves in Figure 3.2(a) show that the increase in [HCOOH] leads to the saturation of the reaction rate. High [HCOOH] concentration results in nearly full coverage of active sites on the palladium surface. This inhibits the adsorption of $[Cr_2O_7^{2-}]$ to start the surface reaction; this same trend is also observed in Figure 3.2(b). The obtained parameters (listed in table of Figure 3.2(c)) were chosen to provide the best fit overall to the calculated initial reaction rates r of all of the experiments.

Next, I employed these obtained parameters to develop the predicted reaction kinetics as shown in Figure 3.3 below. For all the reaction conditions shown in Figure 3.2, the concentration of formic acid ([B]) is 30 times larger than dichromate ion ([A]), thus [B] is considered to be constant value throughout the

entire reaction time course. When the values of k , K_1 , K_2 and initial $[B]$ are plugged into equation 3.6, the theoretical $[A]$ concentration changes over reaction time t can be predicted and compared to the experimental $[A]$ changes over time. As shown in Figure 3.3 (a)-(d), when the ratio between $[B]$ and $[A]$ is larger than 100 fold, the predicted $[A]$ obtained from the model fitting by using three parameters (k , K_1 and K_2) are in good agreement with the experimental values of $[A]$. However, when the ratio between $[B]$ and $[A]$ is lower than 100, the experimental data deviated from the predicted $[A]$, especially as the reaction proceeds for longer time, as shown in Figure 3.3 (e) and (f). Specifically, the conversion rates in these cases were slower than the model-predicted values. This disagreement of experimental data with the model may be due to the over simplification during the derivation procedure. Another rate expression derivation based on the pseudo-steady-state hypothesis is shown in Section A1.3 of the Appendix. In that detailed derivation, the reverse reaction of step 3 is also taken into account. The neglection of the reverse reaction of step 3 is only valid when the concentration of $[B]$ is high and/or k_{-3} is low, i.e. $k_4 K_2 [B] \gg k_{-3}$. On the other hand, when the concentration of $[B]$ is relatively small (with $[B]/[A]$ ratio < 100) and/or the reverse reaction rate k_{-3} is high, the reverse reaction of step 3 cannot be neglected, thus the real experimental reaction rate may become lower than the prediction based on the derived model equation (3.6).

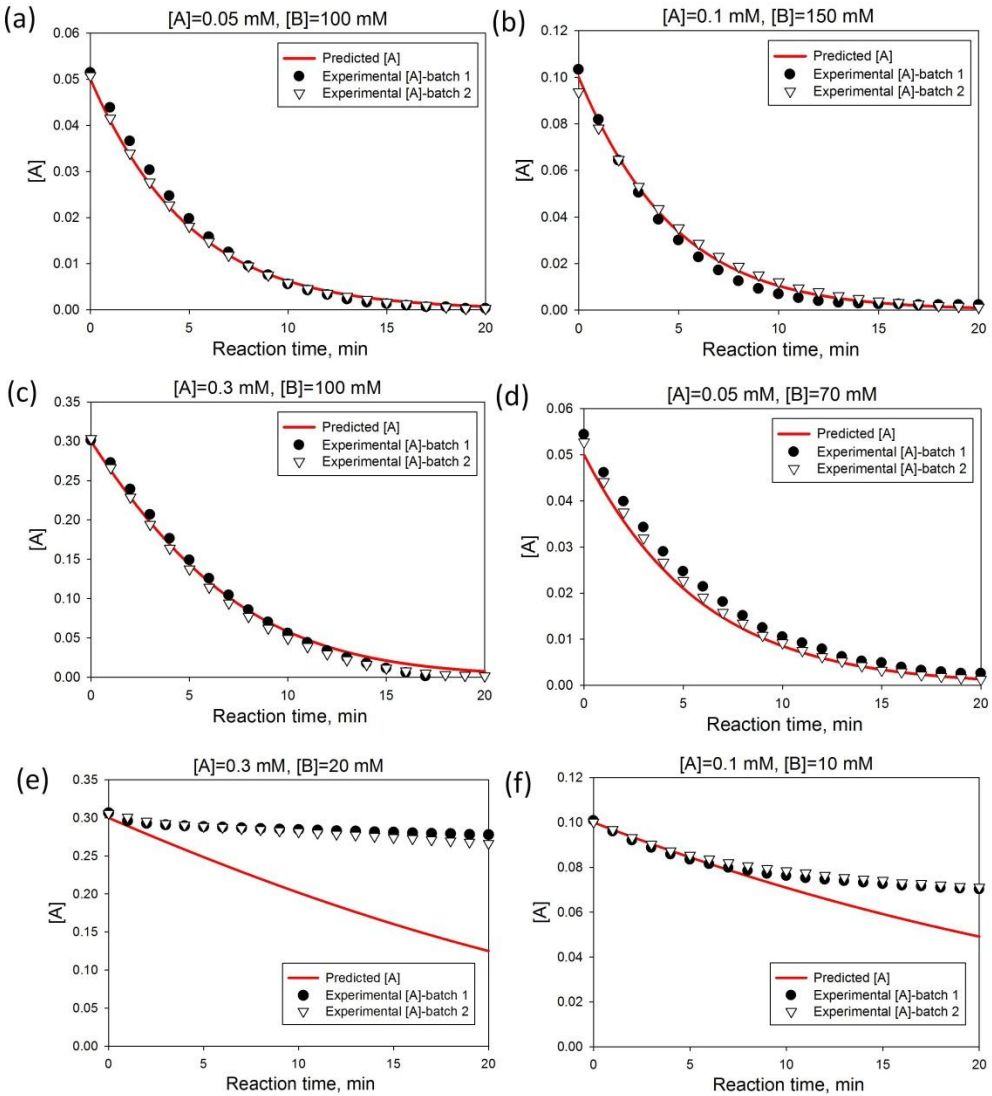


Figure 3.3. Comparison of Predicted $[A]$ with the Experimental $[A]$ over the Time Course

From the model fitting analysis shown in Figure 3.2 and 3.3, the Langmuir-Hinshelwood mechanism was found to be applicable to predict the initial reaction rate of dichromate reduction. Deng and Stone^{63,64} demonstrated that metal oxide-catalyzed Cr(VI) reduction by naturally-occurring organic compounds is subjected to surface catalysis and follows Langmuir Isotherm-type behavior. However, to our knowledge, there is lack of kinetics study and reaction mechanism of Pd catalyzed Cr(VI) reduction with formic acid as the electron donor. The adsorption and oxidation of formic acid over palladium nanocatalysts have been widely studied for the hydrogen production in the clean energy field¹⁹²⁻¹⁹⁴. Indeed, Pd has been reported in the literature¹⁹⁵ to be the most active transition metal catalyst for the formic acid oxidation. The adsorption of Cr(VI) on various substrates^{32,55,196} simulated by Langmuir Adsorption Isotherm has also been studied. Previous reports provide solid support in different aspects for our Langmuir-Hinshelwood study for the Pd-catalyzed dichromate reduction with formic acid as the electron donor. As shown in Section 3.2.7, the experimental data were fit to the Langmuir-Hinshelwood model and evaluate the theoretical support behind it. These results show that: (1) the model equation is only applicable for the prediction of the initial reaction rate, (2) the adsorption constant of dichromate ion is substantially larger than that of formic acid (263 times according to our results), (3) the obtained model equation can predict the [A]

changes over reaction time well for large [B]/[A] ratio conditions. However, the model does not predict the whole reaction time course well for small [B]/[A] ratio conditions. This further explains why previous studies^{10,57,197} all utilized much more formic acid than dichromate for the catalytic dichromate reduction reaction. Through the model fitting study reported in this dissertation, the reaction mechanism and kinetics can thus be better understood for the palladium-catalyzed heterogeneous dichromate reduction by formic acid.

Overall, the reaction kinetics at the initial reaction stage can be represented in terms of the Langmuir-Hinshelwood mechanism that involves surface adsorption of dichromate and formic acid on the active Pd surface to start the surface reaction. Notably, these results clearly indicate that dichromate has much stronger adsorption than formic acid onto the active sites.

3.5. Comparison with Commercial 5% Pd/C Catalysts

Next to gain further quantitative understanding of the catalytic activity of the TMV-templated Pd nanocatalysts, I carried out a direct comparison study with commercially available 5% Pd/C catalysts. To examine the dichromate conversion for Pd/C catalysts, a small volume of the reaction solution was taken out and filtered by 0.22 μm membrane at different time points and the absorbance was measured at 350 nm. Triplicate dichromate reduction reactions with different

catalyst charges were carried out and the reaction rates normalized by Pd mass within the kinetics controlled region were obtained.

The normalized reaction rate catalyzed by 5% Pd/C was determined to be 0.0164 ± 0.0002 (mol/(g Pd·min)), while the highest rate that can be achieved by TMV-templated Pd nanocatalysts (Pd diameter (D_{Pd}) = 3.6 ± 0.4 nm, Pd loading=4.0 μ g Pd/g chip) was found to be 0.0275 ± 0.0019 mol/(g Pd·min), which is 68 % higher than that of Pd/C. The Pd-TMV chip catalysts prepared under other metallization conditions also show comparable catalytic activity (per unit Pd mass) as the commercial Pd/C catalysts. In contrast, Pd/C has shown to possess much broader size distribution in my own examination: average size 3.18 nm with minimum size 1 nm and maximum size 10 nm (as shown in TEM images in Figure 3.4), with certain degree of Pd particle aggregation on the carbon support. The measured Pd particle size distribution is shown in Figure 3.5. From the size distribution, the specific surface area (per unit of mass) was calculated to be 70.7 m^2/g , by using Equation 3.7.

$$SSA = \frac{\sum_{i=1}^n a_{m,i} F_{m,i}}{\rho \times \sum_{i=1}^n v_{m,i} F_{m,i}} \quad \text{Equation (3.7)}$$

(SSA: specific surface area per unit of mass; $a_{m,i}$: surface area of Pd nanoparticles with size m; $v_{m,i}$: volume of Pd nanoparticles with size m; $F_{m,i}$: Frequency of Pd nanoparticles with size m; ρ : density of Pd metal)

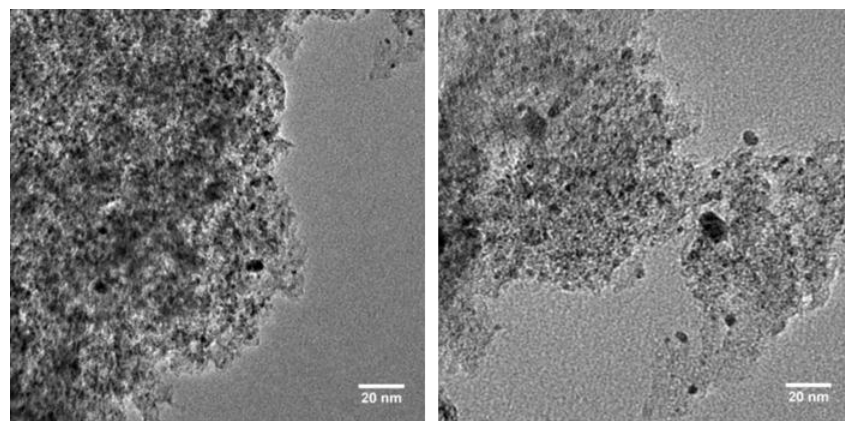


Figure 3.4. TEM Images of Commercial 5% Pd/C Catalysts

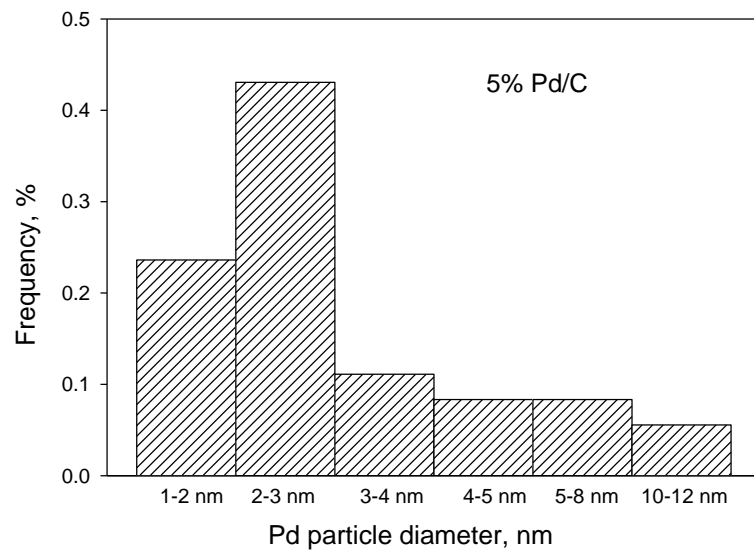


Figure 3.5. Pd Particle Size Distribution of Commercial 5%Pd/C Catalyst

Furthermore, the specific reaction rate (per Pd surface area) of commercial 5% Pd/C was calculated to be $0.23 \text{ mmol}/(\text{m}^2 \cdot \text{min})$, which is lower than that of Pd-TMV chip catalysts ($0.65 \text{ mmol}/(\text{m}^2 \cdot \text{min})$) prepared with optimized synthesis condition. The difference in reaction rate may be due to size-dependent effect (shown in Section 3.8) or the support effect. Therefore, these viral-templated Pd catalysts are shown to be more efficient catalysts than the Pd/C due to the narrow particle size distribution, absence of any deactivating surfactants or capping agents combined with pristine synthesis conditions.

Next, in order to understand the Pd catalyzed dichromate reduction, the activation energy E_a of both Pd-TMV and Pd/C catalyst systems was investigated as shown in Figure 3.6. For this, the apparent dichromate reduction rate constants at different temperatures were measured for both catalytic systems, and the E_a was obtained from the slope of $\ln k'_{\text{app}}$ versus $1/T$. The E_a for dichromate reduction catalyzed by Pd-TMV chip ($D_{\text{Pd}}=11.4 \text{ nm}$, $11.8 \mu\text{g Pd/g chip}$) is determined to be 27.3 kJ/mol , while the E_a from commercial Pd/C catalyst system is 25.7 kJ/mol . This nearly identical E_a from the two catalyst systems indicates similar catalytic mechanism in the presence of Pd nanoparticles. Generally, catalysts speed up chemical reactions by providing an alternative reaction pathway involving different transition states with lower activation energy. Without using any catalysts, the activation energy of Cr(VI) reduction by vitamin C is $63.5 \text{ kJ/mol}^{198}$,

by Soil Humic Substances (SHA) is 121.8 ± 2.8 kJ/mol¹⁹⁹, and by Soil Fulvic Acid (SFA) is 111.1 ± 1.4 kJ/mol²⁰⁰. In the presence of chitosan-Fe⁰ nanoparticles, the E_a for dichromate reduction was reported to be 33 kJ/mol²⁰¹. Therefore, Pd is an efficient catalyst for dichromate reduction.

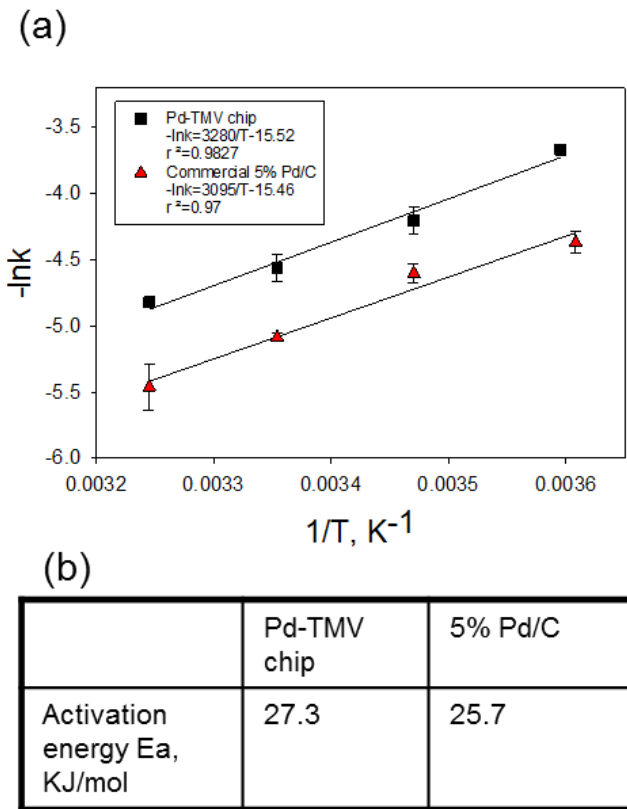


Figure 3.6. The Activation Energy of Pd-TMV Chip and Pd/C Catalysts

Arrhenius plot of the Pd catalysts specific rate constant k'_{app} ($L/(g\text{ Pd}\cdot\text{min})$) and the inverse temperature $1/T$ (K^{-1}). The synthesis condition for Pd-TMV chip is 0.5 mM Na₂PdCl₄, 15 mM NaPH₂O₂, 20min metallization. The reaction condition: 0.1 mM K₂Cr₂O₇, 100 mM NaCOOH, pH=3, at 25 °C.

3.7. Effect of Synthesis Conditions on the Particle Size and Surface Loading

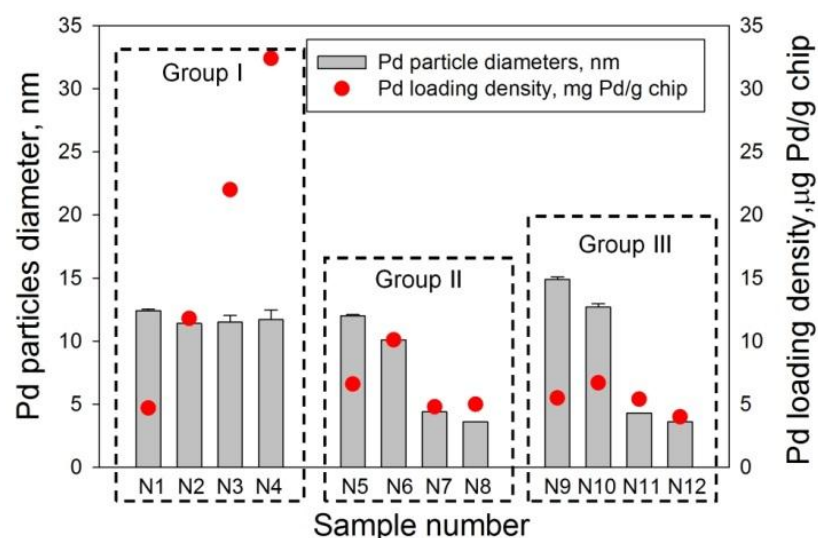
This viral-templated nanocatalyst synthesis approach enables facile control of both particle size¹⁵⁸ and surface loading density²⁰² by simply tuning synthesis parameters. Building on the unique feature of this bottom-up assembly approach, I examined the effect of such synthesis conditions on the nanoparticle size and the Pd loading density via Atomic Force Microscopy (AFM), Grazing Incidence Small Angle X-ray Scattering (GISAXS) and Inductively Coupled Plasma (ICP) respectively, and on the catalytic activity.

First, Figure 3.7 shows the effect of synthesis conditions on the Pd particle size and surface loading density. For this, I employed Pd precursor concentrations ranging from 0.25 to 5 mM and the reducer (NaPH_2O_2) from 5 to 55 mM¹⁵⁸, as shown in the table of Figure 3.7(a). The as-prepared Pd-TMV catalyst chips were then examined via GISAXS for Pd particle size and ICP for surface loading determination as in Figure 3.7(b).

(a)

	Sample number	Na_2PdCl_4 , mM	NaPH_2O_2 , mM
Group I	N1	0.25	15
	N2	0.5	15
	N3	2	15
	N4	5	15
Group II	N5	0.5	5
	N6	0.5	30
	N7	0.5	45
	N8	0.5	55
Group III	N9	0.25	5
	N10	0.25	30
	N11	0.25	45
	N12	0.25	55

(b)

**Figure 3.7. Effect of Catalyst Synthesis Conditions on Catalyst Properties**

(a) Table of TMV-templated Pd catalysts prepared under various synthesis conditions. (b) The Pd particle size and loading density of TMV-templated Pd catalysts.

First, the sample Group I (N1-N4) in Figure 3.7(b) shows that the Pd loading density per unit mass of Pd-TMV chip increases almost linearly with the increase in Pd precursor concentration at the same reducer concentration, with nearly identical particle size (12 nm diameter). This trend indicates that chips with higher Pd loading density yet similar particle size may have more Pd particle coating on each TMV template. Next, both sample Groups II (N5-N8, 0.5 mM Na₂PdCl₄) and III (N9-N12, 0.25 mM Na₂PdCl₄) show that smaller Pd nanoparticles were formed by higher reducer concentration at the same Pd precursor concentration. However, the data points for both Groups II and III in Figure 3.7(b) show that the Pd loading density increases and then decreases along with the increasing reducer concentration. This result indicates that the reducer concentration has effects on both particle size and loading density, and that the number of Pd particles on each TMV template varies with metallization conditions. For example, sample N5 has the particle average diameter of 12 nm, which is larger than N6 (10 nm). However, the Pd loading density of N5 (6.6 µg Pd/g chip) is lower than that of N6 (10.1 µg Pd/g chip). This indicates that there are much less yet bigger Pd particles on each TMV for sample N5 compared to N6. Overall, the size of Pd nanoparticles formed along TMV biotemplates under all synthesis conditions studied can be divided into two groups, 3-5 nm and 10-14

nm respectively. In summary, the results in Figure 3.7 show that the concentrations of the Pd precursor and reducer in the simple and mild catalyst synthesis procedure have effects on both the Pd nanoparticles size and Pd loading density of viral-templated Pd nanocatalysts.

3.8. AFM and GISAXS Study of Viral-templated Pd Nanoparticles

AFM images were acquired using a Dimension 3100 series Scanning Probe Microscope (SPM) (Veeco, Woodbury, NY) in tapping mode with TAP-A1-50 AFM tips (Budget Sensors, Sofia, Bulgaria), and the images were analyzed using NanoScope software³. Figure 3.8 shows the AFM images of sample N1-N12, which were prepared with various synthesis conditions. Samples N1-N4 appear to have similar particle size, while N4 appears to have denser coverage. From sample N5-N8, the Pd particle sizes seem to become smaller. Similar trend is observed for sample N9-N12. These AFM images provide an initial observation of the Pd nanoparticle size difference between sample N1-N2, which is further confirmed and determined by GISAXS analysis.

Grazing Incidence Small Angle X-ray Scattering (GISAXS) was applied for the in-depth examination of the particle size under varying synthesis conditions as well as stability under reaction conditions, as shown in Figure 3.9. To further examination of the average Pd particle diameter, Guinier analysis^{158,186,187} was

employed. For this, scattering curves were first created by making a horizontal line-cut of intensity (shown by the red line in the scattering pattern in Figure 3.9(a)). The intensity $I(q_{xy})$ was then plotted versus the scattering vector q_{xy} . The scattering curves from several selected samples before and after the dichromate reduction reaction are shown in Figure 3.9(b).

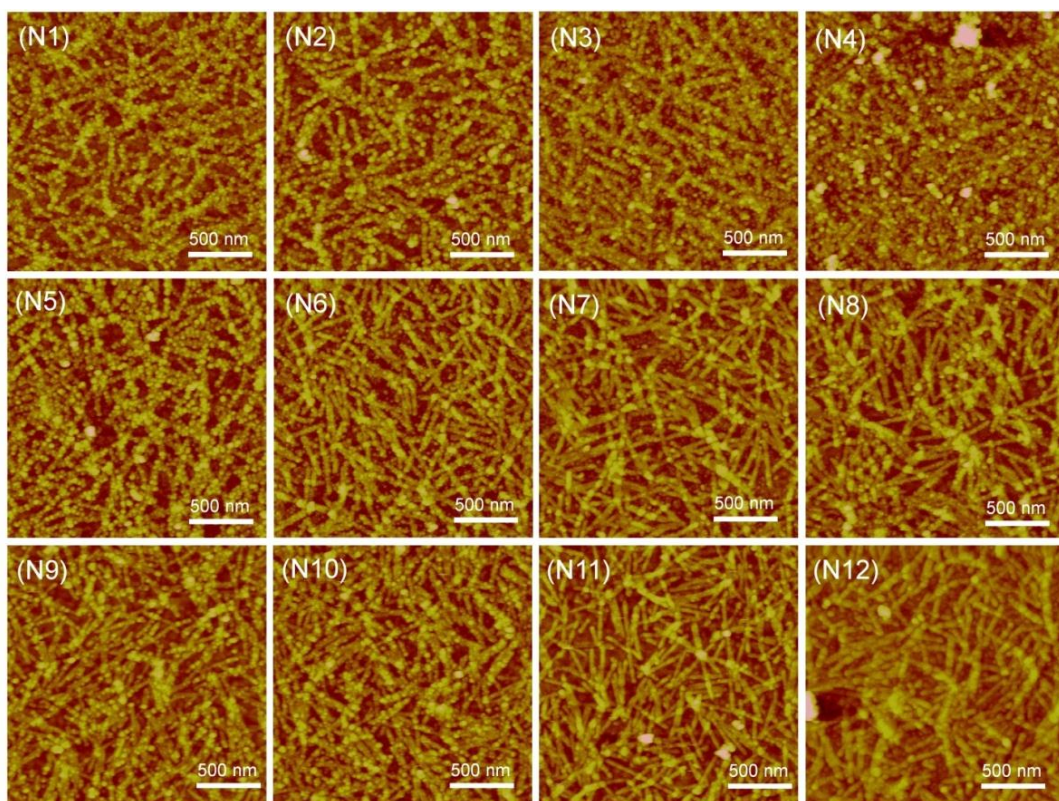


Figure 3.8. AFM Images of Pd-TMV Chips

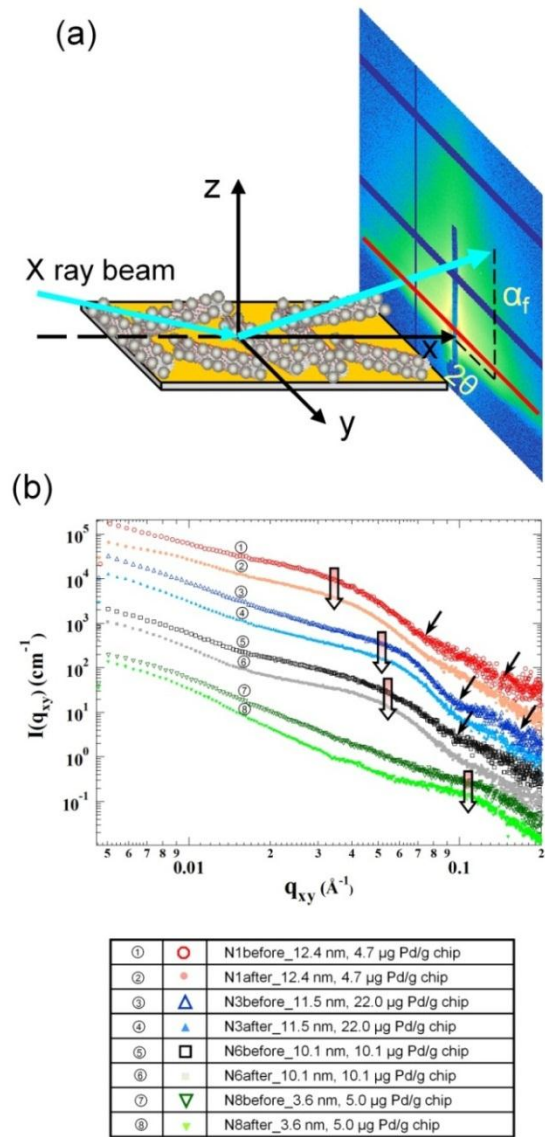


Figure 3.9. GISAXS Study of TMV-templated Pd Nanoparticles

(a) Schematic diagram of the GISAXS setup. (b) GISAXS scattering curves ($I(q_{xy})$ vs q_{xy}) of Pd-TMV samples before reaction and after 4 cycles' reaction.

The four downward arrows marked on the scattering curves in Figure 3.9(b) indicate bump locations (a.k.a. Guinier knees), which are inversely proportional to nanoparticle size¹⁸⁶; e.g. Guinier knee at lower q_{xy} indicates larger particle size. The exact average Pd particle sizes of different samples shown in Figure 3.9(b) were obtained via Guinier analysis^{158,160}. Most of the samples exhibit oscillation features as shown with the small black arrows in Figure 3.9(b), clearly indicating the monodisperse nature of the Pd nanoparticles^{186,187}. In addition, the Guinier knee locations of the Pd-TMV chips before (large dotted curves) and after (small dotted curves) the dichromate reduction reactions are nearly identical, showing no shift in q_{xy} . This clearly indicates that there is no apparent change in the particle size or distribution during the reaction. Further Guinier analysis demonstrates that the Pd particle size remains the same over catalytic reaction for all particle size cases (Figure 3.9(b)), further confirming the stability of TMV-templated Pd nanocatalysts for dichromate reduction reaction²⁰³. In summary, results shown in Figure 3.9 indicate that: (1) Pd nanoparticle sizes are readily controlled by tuning the synthesis conditions, (2) Oscillation of scattering curves shows that Pd nanoparticles on TMV templates are quite monodisperse, and (3) No shift in Guinier knee locations after reaction indicates the stability of TMV-templated Pd nanoparticles for all the particle size ranges examined.

3.9. Effect of Synthesis Conditions on the Catalytic Activity

Next, I examined the catalytic activity (based on per unit Pd surface area) over a wide range of Pd particle sizes and surface loading densities, as shown in Figure 3.10. For this, all the samples shown in Figure 3.7(a) were applied as catalysts for the reaction with 0.1 mM $\text{K}_2\text{Cr}_2\text{O}_7$ and 100 mM NaCOOH at pH 3, and the normalized reaction rates per unit Pd surface area ($\text{mmol}/(\text{m}^2 \cdot \text{min})$) were plotted against the particle size (nm) and surface loading density ($\mu\text{g Pd/g chip}$).

First, the comparison of the Pd-TMV chip samples with similar Pd loading density (~5 $\mu\text{g Pd/g chip}$; located along blue short dash arrow in the 3D plot of Figure 3.10(a) and 2D plot of Figure 3.10(b)) show that Pd nanoparticles with larger size show higher catalytic activities. This clear trend suggests the size-sensitive property of dichromate reduction by Pd nanocatalysts. This is in line with previous reports that formic acid oxidation is a structure-sensitive reaction with Pd catalysts^{204,205}. Formic acid electrooxidation on single-crystal Pd is affected by the crystallographic orientation of the Pd surface²⁰⁶. In the active-intermediate (AI) pathway ($\text{Pd} + \text{HCOOH} \rightarrow \text{Pd-(COOH)}_{\text{ads}} + \text{H}^+ + \text{e}^- \rightarrow \text{Pd} + \text{CO}_2 + 2\text{H}^+ + 2\text{e}^-$), the strength of formic acid adsorption on the Pd(111) plane is stronger than on the Pd(100) plane²⁰⁶, so the oxidation reaction is favorable on Pd(111) plane. Meanwhile, the relative abundance of Pd(111) crystallographic planes varies with the particle size²⁰⁷. Generally, larger Pd particle size tends to

have thermodynamically more stable structure with larger Pd(111) to (100) ratio, thus larger Pd particles with more (111) planes would be more active for the formic acid oxidation in the AI pathway²⁰⁷. In contrast, smaller particles have certain degree of lattice defect, which may possess less intact (111) planes. In addition, higher concentration of reducing agent may lead to rapid formation of small Pd nanoparticles with amorphous structures, which results in lower catalytic activities. The real mechanism of this size-dependent behavior needs to be further explored. Some of the previous TEM observations by my group member Amy K. Manocchi indicate that 10 nm Pd particles show apparent (111) crystallographic planes. Therefore, the experimental results in Figure 3.10 for the Pd catalyzed dichromate reduction by formic acid reveal size sensitive property, where larger Pd particle size contributes to higher catalytic activity.

Furthermore, Pd-TMV samples with similar Pd nanoparticle size (12 nm diameter; located along the green long dash arrow in 3D plot of Figure 3.10(a) and 2D plot of Figure 3.10(c)) show the influence of Pd surface loading density on the catalytic activity. These clearly indicate that lower Pd loading density on chip surface leads to higher catalytic activity based on unit Pd surface area. Conversely, lower catalytic activity (per Pd surface area) from the high Pd loading density case suggests that not all the Pd surface areas are accessible for the surface adsorption-based reaction. With the same number of TMV's on the

chip, the Pd particles are more closely packed on the TMV surface in the higher Pd loading density case, thus it is likely that some Pd surfaces are embedded or not readily accessible. We also hypothesize that when Pd nanoparticles form on the TMV templates, more complex structures between the TMV and Pd particles may have formed. The interaction between Pd nanoparticles and the TMV biotemplates may be essential to the catalyst activity. When the Pd loading density is too high, some Pd nanoparticles may overlap with each other and don't have sufficient contact with the TMV templates. Therefore, the Pd nanoparticles may be more readily accessible and utilized when sparsely dispersed on the viral templates. In the future, the influence of TMV biotemplates on the catalytic activity has to be fully examined and understood.

Overall, results in Figure 3.10 show the combined effect of both Pd particle size and Pd loading density on the chip surface on the catalytic activity (per Pd surface area) for dichromate reduction. Pd-TMV chip catalysts with larger Pd particle size and lower Pd loading density lead to higher catalytic activity per unit Pd surface area. Pd catalyzed dichromate reduction with formic acid shows size-dependent behavior in my study.

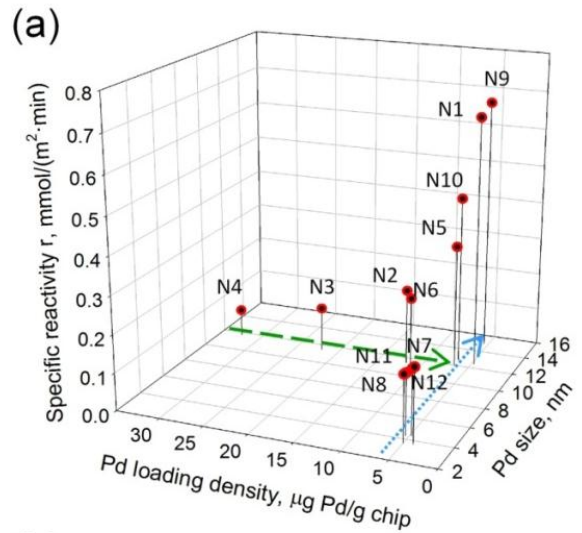


Figure 3.10. Catalytic Activity (based on the surface area) vs. Pd Nanoparticle Size and Loading Density of TMV-templated Pd Nanocatalysts.

The Reaction conditions: 0.1 mM K₂Cr₂O₇, 100 mM NaCOOH, pH=3, at 25 °C. (a) 3D bar chart (b) Initial reaction rate vs. Pd loading density. (c) Initial reaction rate vs. Pd particle size. All data points were obtained from triple runs of experiments reactions.

Combined results in Figures 3.7 and 3.10 reveal the relationship between catalyst synthesis-structure (i.e. size/loading)-activity. Under different synthesis conditions (e.g. Pd precursor or reducer concentration), the Pd particle size and loading density can be varied, leading to the control of catalytic activity. For example, by utilizing lower concentration of Pd precursor or reducer (e.g. samples N1 and N9), larger Pd particles sparsely form on TMV biotemplates, which contributes to higher catalytic activity. Meanwhile, samples with almost the same Pd particle size and loading density appear to have close catalytic activity (e.g. samples N7, N8, N11, N12). Finally, Pd precursor concentration has big effect on the Pd loading density (samples N1-N4), leading to the apparent difference in the catalytic activity. Above all, this catalyst synthesis-structure-activity relationship provides good guidance for the design of efficient Pd nanocatalysts for the dichromate reduction.

3.10. Recyclability of Pd-TMV Chips

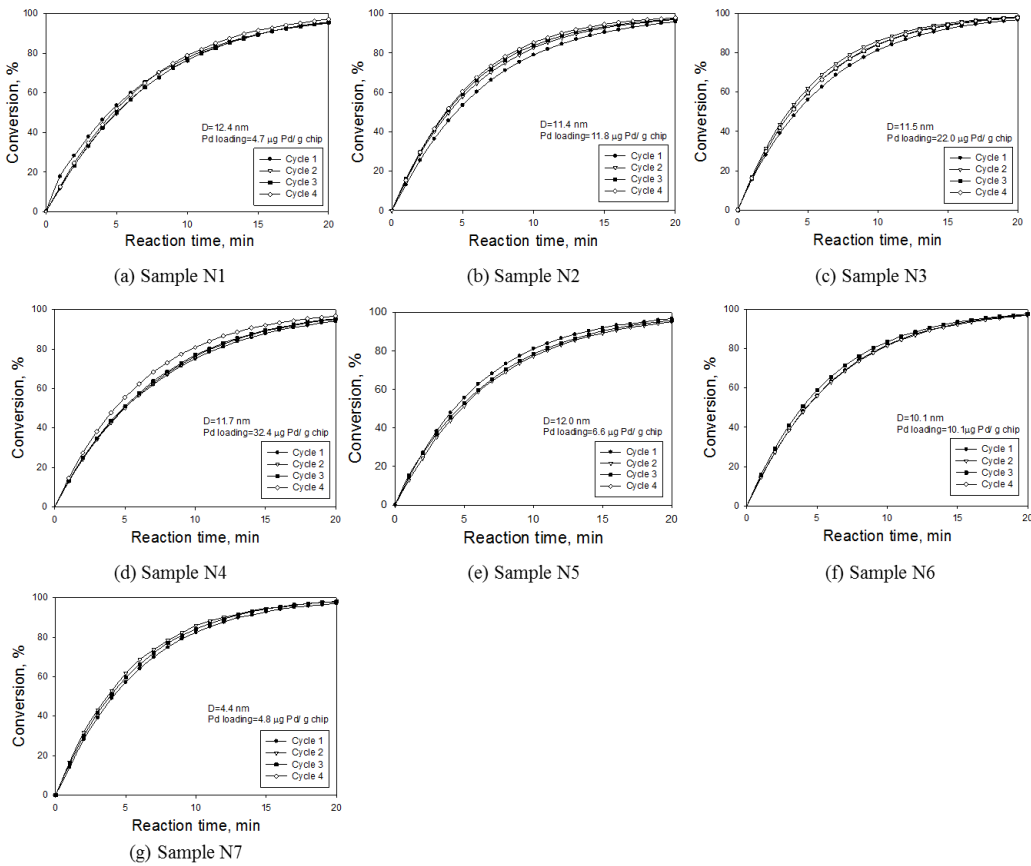


Figure 3.11. Recyclability Study of TMV-templated Pd Nanocatalysts

In order to examine the stability and reusability of Pd-TMV catalysts for dichromate reduction, the recycle studies for representative samples with various Pd particle size and loading density (N1-N7) were conducted, as shown in Figure 3.11. For these studies, the reactions were carried out with 0.1 mM $\text{K}_2\text{Cr}_2\text{O}_7$ and 100 mM NaCOOH, at pH 3 and 25 °C. Thoroughly rinsed Pd-TMV chips were

directly utilized for the next reaction cycle after each batch reaction without any regeneration treatments. Figure 3.11 shows that samples N1-N7 have almost identical conversion rates from four cycles of reactions, indicating that the Pd nanoparticles on TMV templates retained most catalytic activity.

Table 3.1. Reaction Rate Constant Changes over Recycling

Sample #	N1	N2	N3	N4	N5	N6	N7
Reaction cycle							
Cycle 1	0.15	0.16	0.17	0.14	0.17	0.18	0.18
Cycle 2	0.15	0.17	0.18	0.15	0.15	0.17	0.19
Cycle 3	0.15	0.19	0.20	0.15	0.15	0.19	0.19
Cycle 4	0.14	0.18	0.19	0.17	0.16	0.18	0.19
$(k_{app}(\text{max}) - k_{app}(\text{min})) / k_{app}(\text{max}) * 100\%$	8.6%	16%	15%	16%	12%	11%	9.1%

As mentioned in Section 3.2, the dichromate reduction with viral-templated Pd nanocatalysts follows pseudo first-order batch reaction kinetics^{1,2} under the reaction conditions employed. The apparent reaction rate constants k_{app} (min^{-1}) were obtained from the slope of linear regression of $\ln([\text{Cr(VI)}]/[\text{Cr(VI)}_0])$ vs. reaction time. Table 3.1 shows that k_{app} from four reaction cycles of all sample N1-N7 are very close, with less than 16% difference. These results from Figure 3.11 and Table 3.1 indicate that the TMV-templated Pd nanocatalysts with

various Pd particle size and Pd loading density all have good stability and recyclability for at least up to 4 reaction cycles.

To further examine the changes in chemical states of the viral-templated Pd catalysts over the dichromate reduction reaction, XPS was carried out for Pd-TMV chip catalysts (Sample N1-N7) before and after 4 cycles' reactions, as shown in Figure 3.12. The XPS analysis was performed with XPS ESCA SSX-100 machine at the Center for Nanoscale Systems (CNS) of Harvard University (Cambridge, MA). Briefly, the chip samples were mounted on an aluminum cup prior to insertion into the ultrahigh vacuum chamber. The measurement was performed with an Al K α monochromatic X-ray source, focused to a 600 μ m diameter beam for the high resolution spectra. For the individual peak energy regions, pass energy of 100 eV across the hemispheres was used.

As shown in Figure 3.12, all the samples (N1-N7) before and after reaction appear to have the characteristic peaks at 335 eV and 341 eV, which corresponds to the metallic Pd3d_{5/2} and Pd3d_{3/2} peak. Notably, for samples N3, N4 and N6, there appears no apparent binding energy shift, thus no significant chemical state changes after four reaction cycles. For samples N1, N2 and N5, the Pd3d_{3/2} peaks show slight shift to higher binding energy, which implies certain degree of Pd oxidation after 4 reaction cycles. However, the recyclability studies in Figure 3.11 show that the Pd-TMV chip catalysts exhibit high catalytic activity after

reuse for 3 times. These XPS results provide strong chemical evidence for the stability of Pd-TMV nanocatalysts with various size and loading properties.

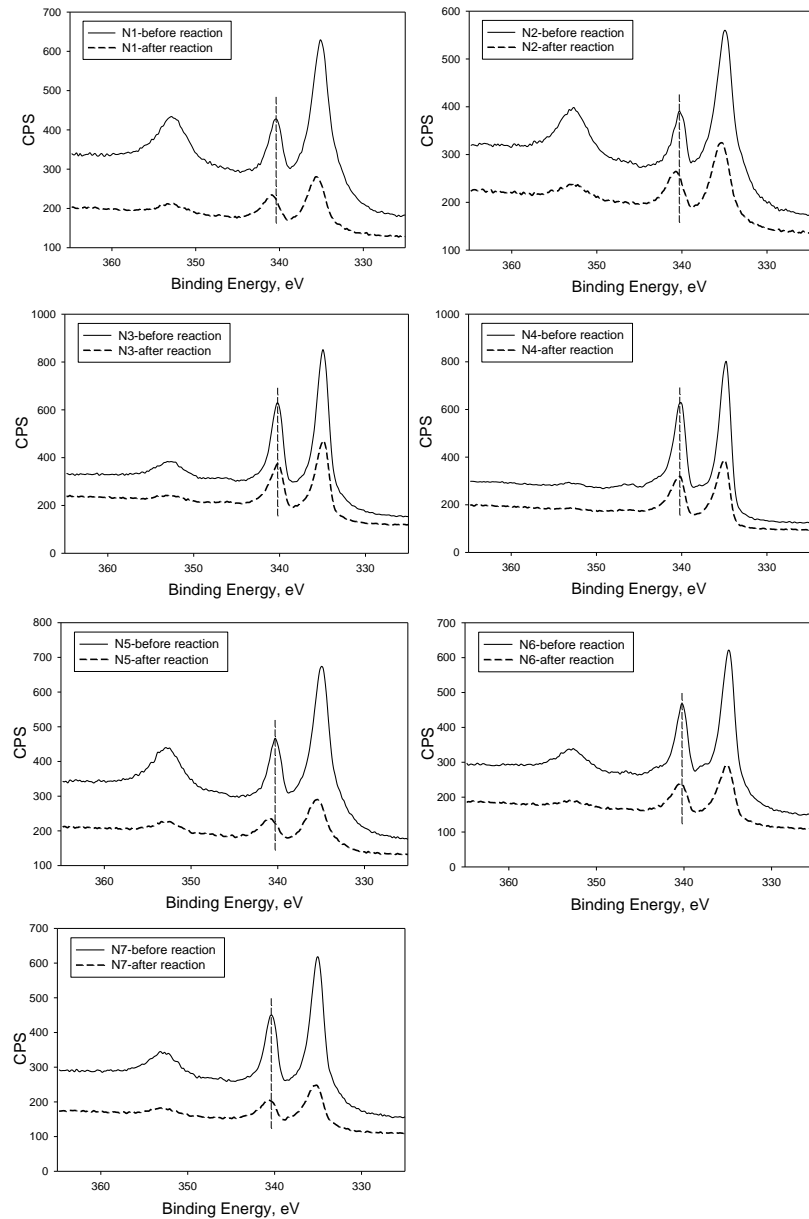


Figure 3.12. X-ray Photoelectron Spectroscopy

3.11. Conclusions

In this chapter, I studied the reaction mechanism, kinetics and the synthesis-structure-activity relationship of the viral-templated palladium nanocatalysts for dichromate reduction reaction. First, the surface-originated heterogeneous nature of dichromate reduction via simple chip removal study was studied. This viral template based Pd nanocatalyst synthesis approach enables facile control of both Pd nanoparticle size and surface loading density. The catalyst synthesis condition study indicates that the Pd catalyzed dichromate reduction by formic acid is a size sensitive reaction, where larger Pd particle size tends to have higher catalytic activity (per Pd surface area). Meanwhile, TMV-templated Pd nanocatalysts with lower loading density showed higher catalytic efficiency (per Pd surface area). From these studies, I envision that this simple, controllable and robust approach for nanocatalyst synthesis could potentially be utilized in other novel catalyst systems and a wide range of heterogeneous surface reactions.

4. Facile Approaches to Control Catalyst Loading

Density and Location by Tunable and Selective TMV

Surface Assembly

4.1. Introduction

While high catalyst loading is desirable in most cases for large scale industry application, the ability to control the catalyst loading density and location is also very important in a number of cases, such as to better understand reaction mechanisms or to investigate complex reaction pathways. A prime example can be found in biocatalysis, where multiple enzymes assembled on solid substrates can be employed for metabolic pathway optimization^{208,209}. Although such controlled assembly strategies have gained significant attention in the biocatalysis field, facile routes to control the loading of metal or inorganic catalysts are still lacking. Over the past two decades, catalytic microreactors have emerged as viable alternatives for such control due to several advantages including continuous operation at small-length scales in closed systems, enhanced heat and mass transfer, and reaction rate²¹⁰⁻²¹². Yet, such microreactors suffer from several technical challenges such as particle clogging, arduous fabrication and packaging procedures, and harsh synthesis conditions that make the catalytic activity uncontrollable and unpredictable.

Therefore, there exists a critical need for simple and facile routes to control the catalyst loading density and precise locations of active catalysts, especially in the small scale reactor, such as microreactor system.

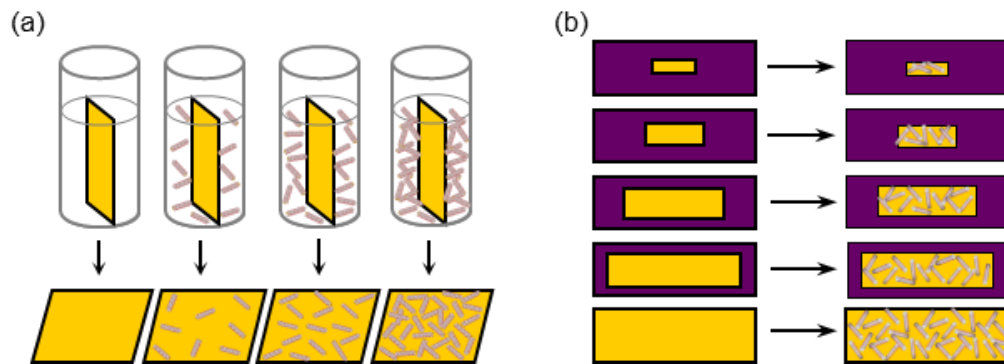


Figure 4.1. Two Facile Approaches for the Control of Pd Loading Density and Location

(a) Control of Pd catalyst loading density by changing TMV concentration for surface assembly. (c) Control of Pd catalysts location via using gold-patterned chip with varying gold surface area.

In Chapter 3, I described the control of catalyst loading density by tuning the catalyst synthesis conditions (including varying Pd precursor and reducer's concentration). In this chapter, two facile routes are presented for the control of both Pd loading density and specific location by harnessing TMV's surface assembly properties. Specifically, TMV surface assembly is: (1) tunable in that the surface density can be readily modulated by simply changing the TMV solution's concentration for gold chip surface assembly²⁰³, and (2) selective in

that TMV binds preferentially onto gold and not onto a variety of other surfaces including silicon oxide, silicon nitride or silica²⁰².

As shown in the schematic diagrams of Figure 4.1(a), tunable surface assembly of TMV is exploited to control the viral template surface density, leading to tunable Pd surface loading. The difference in the Pd-TMV complex density from AFM, the catalytic activity in dichromate reduction as expressed in terms of apparent first-order batch reaction rate constants, and the relative Pd amount examined by XPS all correlate well with each other. In the second route, as shown in Figure 4.1(b), a standard photolithographic patterning technique is employed to fabricate gold-patterned chips with varying gold surface areas for area-based catalytic activity control. AFM images clearly show preferential TMV surface assembly onto gold surfaces but not onto silicon nitride. The catalytic activity (expressed as first-order rate constants) from patterned chips with different size of gold areas correlates well with AFM results, illustrating the control of location where active Pd catalysts are assembled. Combined these results show two facile routes for modulating catalytic activity via tunable and selective surface assembly of viral templates. I envision that these two approaches exploiting bioengineered templates and interactions can be readily extended to other biotemplates and catalytic reaction systems where precise control of catalyst loading and location is highly desired via various surface patterning schemes and bioengineering tools.

4.2. Materials and Methods

4.2.1. Materials

The gold-patterned chips utilized were fabricated via standard photolithography^{209,213}, which was generously provided by Dr. Xiaolong Luo at the University of Maryland. Briefly, 500 μm thick silicon wafers were coated with 2000 \AA silicon nitride film as the insulating layer, followed by deposition of 100 \AA Cr layer, and then 1000 \AA gold film according to the desired shape and size of pattern. As shown in Figure 4.1(b), four types of patterned chips (2.4 cm \times 0.75 cm) were fabricated, containing four sizes of gold area with varying ratios to the whole chip as 1/2 (2.2 cm \times 0.41 cm), 1/4 (1.2 cm \times 0.375 cm), 1/8 (0.85 cm \times 0.265 cm) and 1/16 (0.6 cm \times 0.188 cm), respectively. Other materials applied in this chapter are as described in section 2.2.1.

4.2.2. Methods

For the surface assembly of TMV templates, silicon chips with or without patterned gold were cut into desired sizes (2.4 cm \times 0.75 cm) and thoroughly rinsed by incubating the chips in acetone, isopropanol and methanol, each for 20 min, followed by thorough rinsing with deionized water after each solvent. For gold-patterned chips, 1 N NaOH solution was utilized for complete removal of photoresist after being rinsed by the three organic solvents above, followed by

thorough rinsing with deionized water. These chips were then dried under a stream of ultrapure nitrogen gas and then etched with plasma (Ernest F. Fullam Inc., Clifton Park, NY). Immediately after etching, the clean chips were immersed in TMV solution in phosphate buffer ($\text{pH}=7$) with different concentrations, 0, 10, 50 and 100 $\mu\text{g}/\text{ml}$, for overnight incubation. The patterned chips with varying gold areas were incubated in the same concentration of 100 $\mu\text{g}/\text{ml}$ TMV overnight at room temperature. After the TMV assembly, the chips were thoroughly rinsed with deionized water, dried with N_2 gas and stored at room temperature for further Pd nanoparticle formation. The formation of Pd nanoparticles on surface-assembled TMV templates followed the same protocol as previously in section 2.2.2. Briefly, TMV-assembled gold chips were immersed in freshly prepared mixture of 0.5 mM Na_2PdCl_4 precursor and 15 mM NaPH_2O_2 for 20 min to synthesize ~10nm diameter Pd nanoparticles on TMV templates. These chips were cleaned, dried and then stored at room temperature for catalytic reactions (Pd-TMV chips).

Dichromate reduction reactions, the rate constant determination, the AFM and XPS characterization of the catalysts are as described in section 2.2.

4.3. Control of Catalyst Loading Density and Reaction Rate by Tunable TMV Surface Assembly

4.3.1. Characterization of Pd-TMV Complex Surface Density by AFM

As the first route to control Pd nanocatalyst loading, I modulate the TMV surface assembly density by simply varying the concentration as shown in Figure 4.1(a). For this, gold-coated chips were dipped in TMV solutions with varying concentrations for surface assembly (Figure 4.2(a) to (d)), exposed to Pd precursor with reducing agent NaPH₂O₂ to form nanoparticles on the surface-assembled TMV templates (Figure 4.2(e) to (h)), then probed via tapping mode AFM.

First, Figure 4.2 (a) to (d) show a clear proportional relationship between the TMV concentration and the surface assembly density. Specifically, there are about 0, 14, 40, 80 TMVs within 1 μm^2 gold area respectively for the case of 0, 10, 50 and 100 $\mu\text{g}/\text{ml}$ TMV solution. These results indicate the tunable nature of the TMV surface assembly. In Figure 4.2 (e) to (h), AFM images of chips upon Pd nanoparticle formation show that most Pd nanoparticles are uniformly formed along TMV templates and very few on the gold surface, indicating that Pd particles preferentially form on TMV templates. Meanwhile, the number of tubular Pd-TMV complex remains almost the same as before the Pd particle

formation, suggesting the stability of TMV templates under the reducing environment for Pd nanoparticle formation. Thus, more Pd particles were obtained at higher TMV surface density. To sum up, results in Figure 4.2 illustrate a simple route to control Pd loading by simply changing the concentration of TMV for surface assembly.

4.3.2. Dichromate Reduction Catalyzed by Chips with Different Pd-TMV Density

The effect on the reaction rate constants for Cr(VI) reduction from varying the Pd loading density (Figure 4.2) is shown in Figure 4.3. For this, the Pd-TMV chips were immersed in reaction solutions to catalyze dichromate reduction, and the reaction was monitored by a UV/vis spectrophotometer every minute. The conversion was calculated from the decrease in the absorbance at 350nm characteristic of dichromate ion.

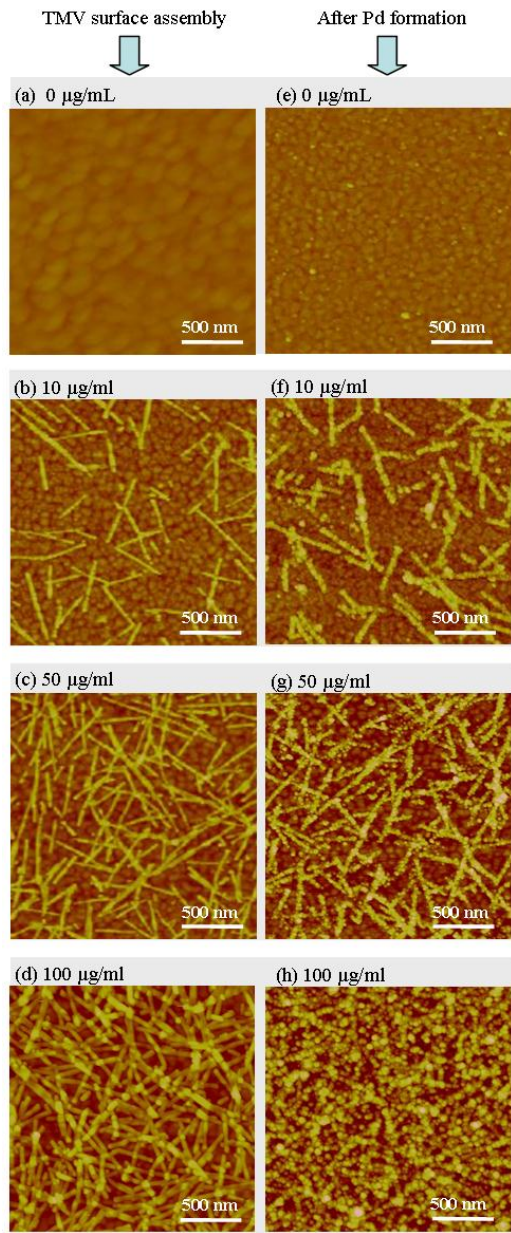


Figure 4.2. AFM Images of TMV Surface Assembly

(a-d) on gold chips with varying concentrations of TMV solution and upon Pd nanoparticles formation (e-h).

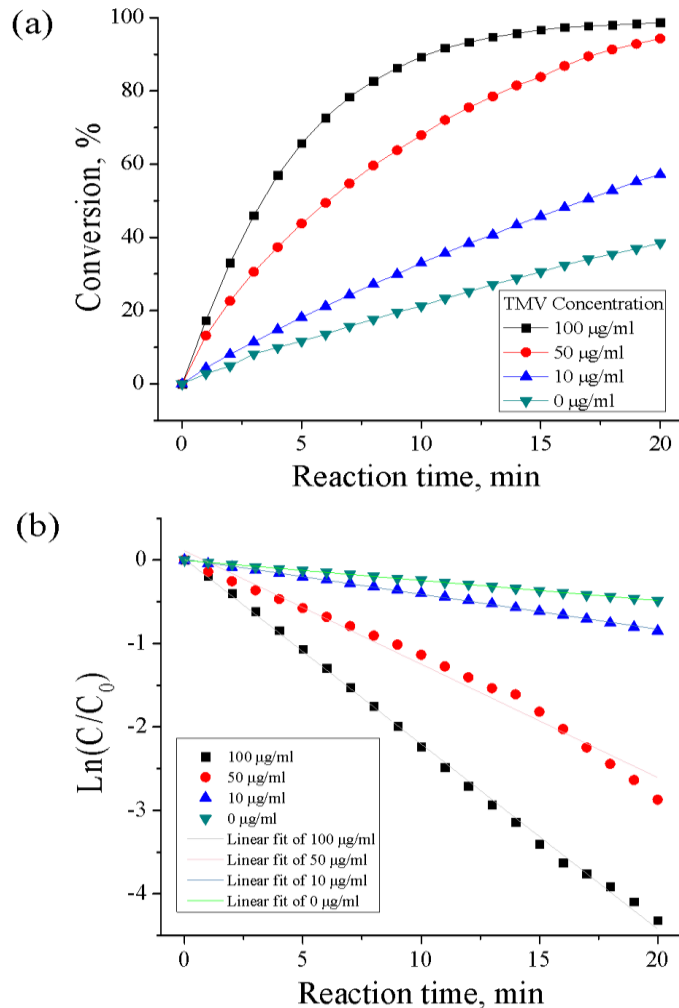


Figure 4.3. Controlled Catalytic Activity of Pd-TMV Chips for Dichromate Reduction

(a) Cr(VI) conversion catalyzed by chips with different Pd-TMV complex density.
(b) First-order reaction kinetics analysis for rate constants.

First, conversion curves of representative batches with Pd-TMV chips prepared from four different TMV concentrations are shown in Figure 4.3(a). The top curve of with square symbol represents the catalytic performance from the chip

prepared by 100 $\mu\text{g/ml}$ TMV surface assembly, where Cr(VI) ion was rapidly converted to near-complete (99 %) depletion within 20 min. The next curve shows that Pd-TMV chips prepared from 50 $\mu\text{g/ml}$ TMV had slightly lower final conversion and lower degradation rate. The final conversions of Cr(VI) catalyzed by the chip from 10 $\mu\text{g/ml}$ TMV and the chip without TMV were even smaller after 20 min reaction time, only about 57 % and 38 %, respectively. This clear difference in both the conversion rate and final conversion strongly indicate the control over catalyst loading via simple tuning of the TMV template assembly density.

Next to gain further quantitative understanding of the reaction rate, a plot between $\ln(C/C_0)$ and reaction time was made, as shown in Figure 4.3(b). The slope from linear regression represents the rate constant for first-order batch reaction kinetics. From top to bottom, the rate constants are 0.22, 0.14, 0.04 and 0.02 min^{-1} in sequence, indicating that the reaction rate is strongly dependent on the “apparent” catalyst loading. In other words, by increasing the density of Pd-TMV complex density, the rate constant increases accordingly; this linear trend is plotted again for further quantitative comparison in Figure 4.3. Importantly, this 1 ml batch reaction system followed first-order batch reaction kinetics in all the cases studied as indicated by consistently high R^2 values in the $\ln(C/C_0)$ plot. In addition, there was no apparent mass transfer limitation as stirring speeds higher than 600 rpm

yielded same conversion rates (data not shown). In summary, the catalytic conversion rate shown in Figure 4.3 correlates well with the apparent catalyst loading shown in Figure 4.2, and supports my first simple route to control the catalyst loading by simply tuning the viral template surface density.

4.3.3. X-ray Photoelectron Spectroscopy Analysis

As shown in Figure 4.4, XPS was then employed to obtain chemical evidence and quantitative correlation between the reaction rate constant (Figure 4.3) and relative Pd loading. Figure 4.4(a) shows XPS spectra in the range of 361~322 eV binding energy (BE) for the Pd-TMV chips prepared from different concentrations of TMV for surface assembly. Spectrum (I) at the top is from Pd chips without TMV templates, showing two typical Au 4d_{3/2} and Au 4d_{5/2} peaks with 352.61 and 334.47 eV BE respectively. No peaks representing either metallic Pd or oxidized PdO were observed here, indicating negligible amount of Pd. Next, the other three spectra (II) (III) (IV) from the Pd-TMV chips prepared from three different TMV concentrations clearly show several features. First, all the three spectra display clear Pd 3d core level features (including Pd3d_{3/2} and Pd3d_{5/2}), especially Pd3d_{3/2} peak at about 341 eV BE, confirming substantial presence of Pd substance on the surface for all the cases. Second, it is clear from these three spectra that as the original TMV concentration increases from samples (II) to (IV), the Au4d_{3/2} peak intensity decreases and the intensity of Pd3d_{3/2}

peak increases simultaneously. Finally, the position of the overlapping peaks rising from Au4d5/2 and Pd3d5/2 shifts towards higher BE direction (the position of Pd3d5/2 peak) as the original TMV concentration increases from the samples (II) to (IV). These clear features strongly indicate: ① surface-assembled TMV provides preferential templating sites for Pd nanoparticle formation since the XPS spectra show negligible Pd amount in the absence of TMV and substantial amount of Pd in the presence of TMV. ② the “apparent” Pd loading shown via AFM images in Figure 4.2 correlates well with the actual surface coverage acquired via XPS, and ③ the relative catalytic activity shown in Figure 4.3 correlates well with the actual surface loading of Pd as seen via XPS.

In Figure 4.4(b), to further examine quantitative relationship among the samples, a non-linear least square fitting program was utilized to calculate relative Pd to Au amount from $Pd/(Pd+Au)$, which was plotted against the number of TMVs per unit area (square micrometer) in along with the rate constants. First, the top line (with square symbol, $Pd/(Pd+Au),\%$ vs. TMV #) clearly shows that there is a linear relationship between Pd percentage from XPS and the apparent TMV surface density from AFM. Second, the bottom line (with circle symbol, k, min^{-1} vs. TMV #) shows similar linear relationship between the first-order rate constant (average value from 3 batches) for Cr(VI) reduction and the TMV surface density

as well. Also, high R^2 values from the linear regression for both lines further illustrate that any two of these three parameters follow the linear relationship well.

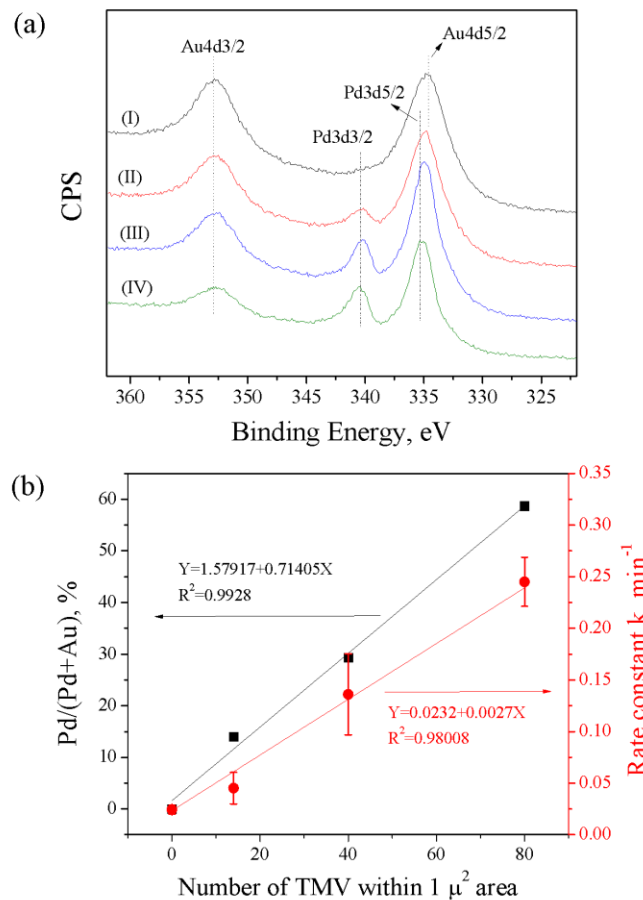


Figure 4.4. High Resolution XPS Spectra from Pd-TMV Chips Prepared with Different TMV Concentrations

(a) High resolution XPS spectra from Pd-TMV chips prepared by different concentrations of TMV for surface assembly (I) no TMV (II) 10 $\mu\text{g}/\text{ml}$ (III) 50 $\mu\text{g}/\text{ml}$ (IV) 100 $\mu\text{g}/\text{ml}$. (b) Correlation between TMV surface density, real Pd amount from XPS and first-order rate constants in catalytic reaction.

In summary, the XPS analysis (Figure 4.4(a)) and the subsequent quantitative analyses (Figure 4.4(b)) provide strong evidences for the difference in the Pd loading, which correlates well with the apparent Pd-TMV complexes density (AFM, Figure 4.2) and the conversion rate for dichromate reduction reaction (Figure 4.3). Thus, these results demonstrate the first route to control the catalytic activity, or more specifically catalyst loading expressed via first-order rate constants, by simply tuning the TMV template concentration for surface assembly.

4.4. Control of Catalyst Location and Reaction Rate by Selective TMV Surface Assembly

4.4.1. Selective Assembly of TMV on Gold-patterned Chips

The second route exploits gold-patterned silicon chips to control the catalyst loading based on gold surface area for viral template assembly, as shown in Figure 4.5. Specifically, different sizes of gold patterns were fabricated onto silicon wafers via standard photolithography and cut into individual chips to provide varying gold surface areas. These microfabricated chips were then immersed in 100 $\mu\text{g}/\text{ml}$ TMV solution for surface assembly then in Pd precursor solution for nanoparticle formation, as shown schematically in Figure 4.1(b). Upon thorough rinsing, the surface-assembled TMV and Pd-TMV complexes on gold and silicon nitride areas were examined by AFM.

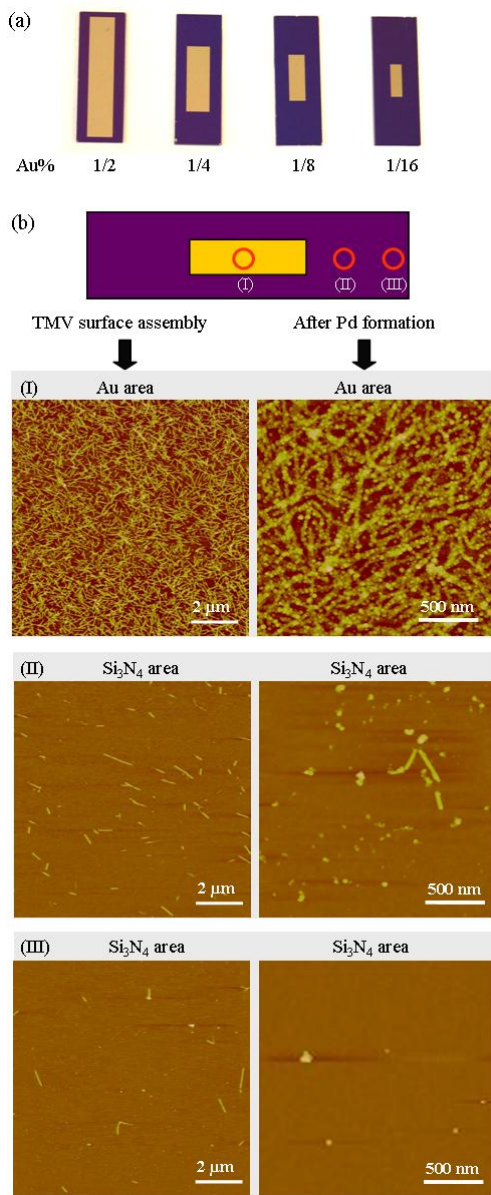


Figure 4.5. Selective TMV Surface Assembly and Pd Nanoparticle Formation

(a) Photograph of fabricated gold-patterned silicon chips with varying gold surface areas. (b) Tapping mode AFM images showing selective surface assembly of TMV on gold-pattered chips: on (I) gold surface, (II) (III) silicon nitride surface.

First, the photograph in Figure 4.5 (a) shows microfabricated chips with decreasing areas of gold patterns from left to right, where the ratios between gold area and the whole chip area are 1/2, 1/4, 1/8 and 1/16, respectively. Gold area clearly shows bright yellow color while the silicon nitride appears dark purple color. Next, Figure 4.5(b) marks three representative positions on the chip for AFM examination (red circles) and the corresponding AFM images before and after Pd nanoparticle formation. The AFM image of position (I) upon TMV assembly clearly shows dense and consistent TMV coverage throughout the gold area.

Furthermore, the AFM image on the right shows that TMVs retain the shape and overall surface density upon Pd nanoparticle formation, and that Pd particles form preferentially along TMV, consistent with the previous results. Meanwhile, much less TMV was observed on the silicon nitride area (both positions (II) and (III)), clearly indicating preferential assembly onto the gold surface. Moreover, AFM images of position (II) and (III) upon Pd particle formation on the right show negligible amount of Pd present on the silicon nitride surfaces. These images further illustrate preferential Pd nanoparticle formation on TMV templates. Overall, this clear difference in the TMV and Pd-TMV complexes surface density between gold and silicon nitride surfaces demonstrates a potentially simple route

for modulating the Pd nanocatalyst loading based on standard photolithography-based patterning.

4.4.2. Dichromate Reduction Catalyzed by Gold-patterned Chips

As shown in Figure 4.6, I carried out dichromate reduction catalyzed by gold-patterned chips with Pd-TMV complexes assembled on the gold area.

First, Figure 4.6(a) shows representative conversion rates for Cr(VI) reduction reaction from patterned Pd-TMV chips with the full size, 1/2, 1/4, 1/8, and 1/16 of gold area and the silicon nitride chip without any gold area (negative control), from top to bottom. Apparently, when the gold area decreased, both final conversion and degradation rate of Cr(VI) ion decreased as expected. The final conversion after 20 min drops from about 99 % for the full size case to only 27 % for 1/16 size case. In addition, silicon nitride chip without any gold area showed final conversion of 6 % after 20 min, which is even lower than the “gold chip only” case shown in section 2.3. Hence, this clear tendency of conversion among chips with varying gold surface areas illustrates the potential for controlling catalyst loading via routine photolithographic patterning in a spatially selective manner. Moreover, a plot of $\ln(C/C_0)$ vs. reaction time in Figure 4.6(b) clearly shows that all the cases follow first-order batch reaction kinetics without apparent mass transfer limitation. The rate constants obtained from the linear regression are 0.25,

$0.12, 0.06, 0.03, 0.028, 0.002 \text{ min}^{-1}$ in sequence from the full size gold chip to the silicon nitride chip without gold, apparently scaling well with the relative surface areas. Hence, this clear difference in the rate constant among these samples further illustrates that the conversion rate correlates well the gold surface area.

Finally, these rate constants from at least triplicate experiments are plotted against the gold surface area in Figure 4.6(c). Clearly, there is a linear relationship between the average rate constant and the area, since most Pd nanoparticles are preferentially formed on TMV templates, which are preferentially assembled on the gold surfaces as shown in Figure 4.5. More importantly, this study clearly demonstrates the spatial control of catalysts; that is, one can control the precise location of the catalysts via surface assembly of viral nanotemplates on patterned substrates followed by preferential nanocatalyst formation on the viral templates.

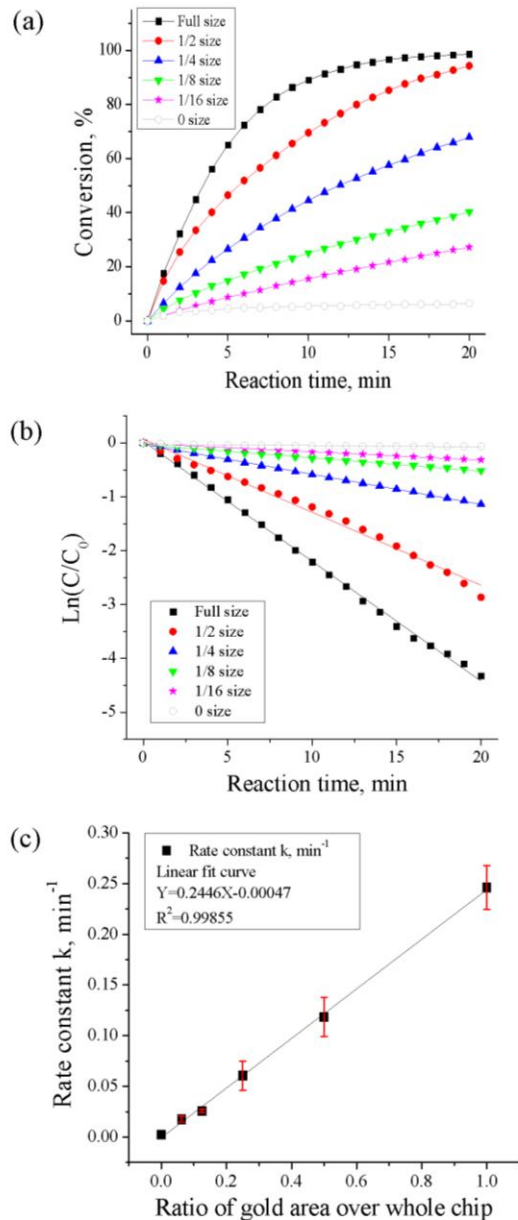


Figure 4.6. Dichromate Reduction Catalyzed by Gold-patterned Chips

(a) Cr(VI) conversion catalyzed by patterned chips with varying gold surface area.
 (b) First-order kinetics analysis for rate constant analysis. (c) Correlation between gold surface area and first-order rate constant.

4.5. Conclusions

In this chapter, I examined two simple routes to modulate the nanostructured Pd catalyst loading for dichromate reduction by taking advantages of TMV's tunable and selective surface assembly on gold surfaces. In the first route, by simply varying TMV solution concentration, the surface density of TMV and the total amount of Pd loading were modulated. The first-order rate constant for dichromate reduction was linearly proportional to the corresponding TMV surface density from AFM images and the Pd loading from XPS analysis, demonstrating the feasibility of controlling Pd catalyst loading via tunable TMV surface assembly. In the second route, by exploiting routine photolithographic patterning, the total amount of TMV and thus Pd loading were controlled via selective TMV assembly onto gold surfaces. The rate constants showed linearly proportional relationship to the gold surface area, showing an alternative route for the location control of active Pd catalysts.

I believe that the facile routes presented in this chapter can be extended to the catalytic activity control of other metal nanocatalysts synthesized based on other preferential templates. Specifically, unique chemical or biological properties that are inherent or engineered to biologically derived materials could be harnessed to provide not only templating sites but also novel routes to pattern, manipulate or control the capacity and/or location of catalytically active nanoparticles.

Furthermore, while I employed gold-patterned chips with large dimensions (in millimeters range) fabricated via standard photolithography in this study, patterned assembly of biotemplates at low- to sub-micrometer scale can be readily achieved by a wide variety of simple and economically viable patterning techniques and reaction schemes, including soft-lithography of self-assembled monolayers (SAM)^{106,214}, direct printing techniques¹⁷⁹, inkjet printing²¹⁵⁻²¹⁷ and nanolithographic techniques^{218,219} on practically any kind of surfaces as common as glass slides. Finally, while the current study enlisted a simple dichromate reduction as a probing reaction under mild aqueous environment, I envision that such simple and tunable routes could find applications in a wide range of areas including catalytic microreactors with tunable catalyst capacity for complex chemical synthesis involving multiple reaction steps.

5. TMV-templated Pd Nanocatalysts for Suzuki Coupling Reaction

5.1. Introduction

In Chapter 2, 3, 4, the TMV template Pd nanocatalysts in chip format were applied for inorganic reaction (dichromate reduction) successfully. In this chapter, I aim at exploring the potential application of this novel catalyst for organic reaction. By far, there has been no endeavor to harness catalytic activities of such attractive materials for organic synthesis reactions of value-added chemicals and small molecule drugs in order to exploit the unique advantages that these potent nanotubular templates offer.

The Pd-catalyzed Suzuki-Miyaura reaction⁴ represents one of the most important routes to synthesize biaryl compounds through the cross-coupling of aryl halides with aryl boronic acids, as shown in the general scheme of Figure 5.1(a). These reactions are typically carried out with phosphine-based or phosphine-free homogeneous Pd catalysts^{20,70,220} in organic solvents. In the past few years, a number of ligand-free heterogeneous Pd catalysts on various supports have emerged^{24,74,221}. While offering simpler catalyst recovery, these ligand-free heterogeneous systems face a number of complications including the need to

employ surfactants in aqueous solution^{22,23} or microwave⁷² to assist phase transfer.

Despite the improved conversion and yield, such additives also present obstacles, such as product contamination, more arduous downstream purification, and increased cost.

In this chapter, I thoroughly examine catalysis of Suzuki coupling reactions by nanostructured Pd nanoparticles templated on TMV, as shown in Figure 5.1(b).

The synthesis method of this catalyst is the same as described in section 2.2.2. These chips (*i.e.* Pd-TMV chips) were then simply immersed in the reaction mixtures, containing the reactants in various ratios of acetonitrile/water mixtures, in well-sealed vials to carry out the Suzuki reactions, and the catalytic reactivity was then analyzed by High-Performance Liquid Chromatography (HPLC). The results show high selectivity and facile product separation with high water content and complete conversion under mild conditions. Additionally, these catalysts exhibit consistent stability throughout reaction and sample analysis using AFM and GISAXS, as well as simple catalyst recovery and reusability rising from surface-assembled chip format. Combined these results demonstrate the facile fabrication of nanostructured viral-metal catalytic systems for ligand-free Suzuki coupling reactions. I believe that this viral-templated bottom-up assembly approach can be readily applied to a wide range of organic synthesis reactions and

other noble metal or alloy catalysts where facile catalyst recovery, product separation, and mild reaction conditions are desired.

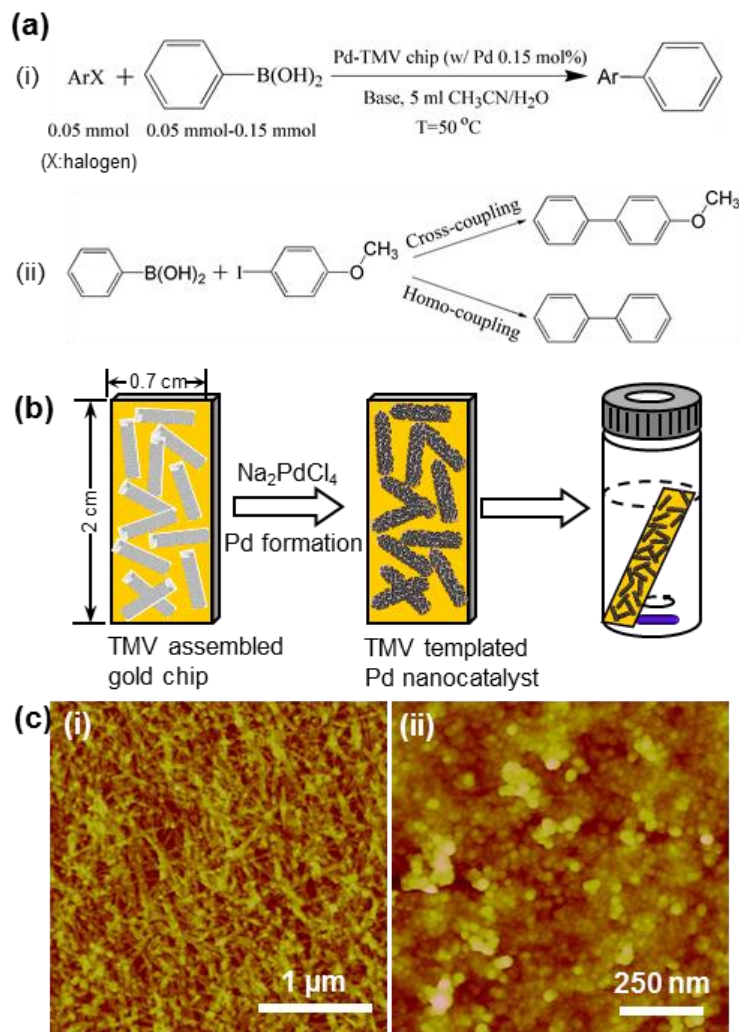


Figure 5.1. Pd-TMV Nanocatalyst Catalyzed Suzuki Reaction

(a) Scheme of Suzuki cross- and homo-coupling reactions catalyzed by nanostructure Pd-TMV complex. (b) Diagram of TMV templated Pd catalyst and simple reaction setup. (c) AFM images of TMV assembled gold chip (i) and Pd formation on assembled TMV (ii)

5.2. Materials and Methods

5.2.1. Materials

Iodoanisole (IA) (>98%), bromoanisole (99%), chloroanisole (99%), iodophenol (>98%), iodobenzene (>98%), 4-methoxybiphenyl (4-MB) (98%), and sodium carbonate (Na_2CO_3) were purchases from Alfa Aesar (Ward Hill, MA) and used without further purification. Phenylboronic acid (PBA) (>95%), bromobenzene (99%), biphenyl (BP) (99.5%).

5.2.2. Synthesis of TMV-templated Pd Catalysts

The Pd-TMV catalyst chips were prepared as previously described in section 2.2.2 with minor modifications. Briefly, clean gold chips were immersed in TMV1cys solution (200 $\mu\text{g}/\text{ml}$) for surface assembly that yielded highly dense and consistent surface loading. These TMV-assembled chips were then exposed to 5 mM Na_2PdCl_4 precursor solution containing 15 mM NaPH_2O_2 reducer for 20 min, which provided reproducible formation of about 13 nm Pd nanoparticles along the TMV tubes.¹⁶ These Pd-TMV chips were then thoroughly rinsed with deionized water, dried, and stored for the reaction studies.

5.2.3. Suzuki Reaction Studies

The Suzuki reactions between iodoanisole (IA) and phenylboronic acid (PBA) were catalyzed by as-prepared Pd-TMV chips. For this, various amounts of IA, PBA and Na₂CO₃ were dissolved in 5 ml acetonitrile/water (CH₃CN/H₂O) solvent. After the reaction mixture was heated to 50 °C, one Pd-TMV chip was added to start the reaction with stirring at 600 rpm for 24 hours.

To study the solvent effect, 0.05 mmol IA (10 mM), 0.05 mmol PBA (10 mM) and 0.15 mmol Na₂CO₃ (30 mM) were dissolved in 5 ml CH₃CN/H₂O mixture with different volume ratio of 3:1, 3:2, 1:1 and 2:3. For the reactant ratio study, concentration ratios of IA: PBA: Na₂CO₃ (mM: mM: mM) were varied as 10:10:30, 10:15:30, 10:20:30, 10:30:30, 10:20:40, and 10:30:60 all in an CH₃CN/H₂O (2:3) mixture. Reusability studies of Pd-TMV chips were carried out by taking the chips out of the completed reaction mixture, rinsing with deionized water, drying, and then immersing in a fresh reaction mixture for three more reaction cycles without further treatments or activation steps. Suzuki reactions between phenylboronic acid and other aryl halides, including bromoanisole, chloroanisole, iodophenol, iodobenzene, bromobenzene, were carried out under various reaction conditions, as described in Table 5.3.

5.2.4. High-Performance Liquid Chromatography (HPLC) Analysis

The reactants and products in the Suzuki reaction mixture were analyzed by HPLC (Waters LC module 1 plus, Milford, MA) equipped with a UV detector at 254 nm. A reversed-phase Nova-Pak C18 column (Waters, 4.6×150 mm, 4 µm) was used with an acetonitrile/water (60:40, v/v) mixture as the eluent at a flow rate of 1 ml/min.

Calibration curves, for determining the concentration of all reactants and products, were constructed by plotting the peak area versus the concentration of all standard compounds. The solutions were diluted 4 or 8 times to be within the range of calibration curves. The product yields at each time point were calculated based on the original concentration of the aryl halides. For example, the 4-MB yield was calculated by Equation (5.1).

$$Yield, \% = \frac{[methoxybiphenyl]_t}{[iodoanisole]_0} \times 100\% \quad \text{Equation (5.1)}$$

5.2.5. Catalyst Characterization

The catalyst was characterized by Atomic Force Microscopy (AFM) and Grazing Incidence Small Angle X-ray Scattering (GISAXS), as described in section 2.2.4.

5.3. Effect of Solvent Ratio on Reaction Selectivity

In Figure 5.2, I examine the effect of the solvent ratio between acetonitrile and water ($\text{CH}_3\text{CN}/\text{H}_2\text{O}$) on the selectivity of the Suzuki coupling reaction catalyzed by Pd-TMV chips. For this, as prepared Pd-TMV chips were applied as catalysts for reactions with 10 mM phenylboronic acid, 10 mM iodoanisole, 30 mM sodium carbonate at 50 °C in well-sealed vials. The reactants and products were analyzed via HPLC.

First, Figure 5.2(a) shows that the $\text{CH}_3\text{CN}/\text{H}_2\text{O}$ ratio is critical to the competition of cross-coupling against the homo-coupling pathway. Specifically, higher water content (*i.e.* $\text{CH}_3\text{CN}/\text{H}_2\text{O}=2:3$) is beneficial for the production of cross-coupling product 4-methoxybiphenyl (4-MB), and suppresses the production of homo-coupling product biphenyl (BP). When the $\text{CH}_3\text{CN}/\text{H}_2\text{O}$ ratio was changed from 3:1 to 2:3, the yield of 4-MB increased from 23.3% to 66.9%, while the yield of BP decreased from 20.1% to 14.4% under the reaction conditions studied. This trend clearly shows that water facilitates the cross-coupling pathway while providing mild reaction conditions with less organic solvent. In addition, higher or lower water content, beyond the range shown in Figure 5.2(a), did not provide adequate solubility of Na_2CO_3 or iodoanisole at 50 °C.

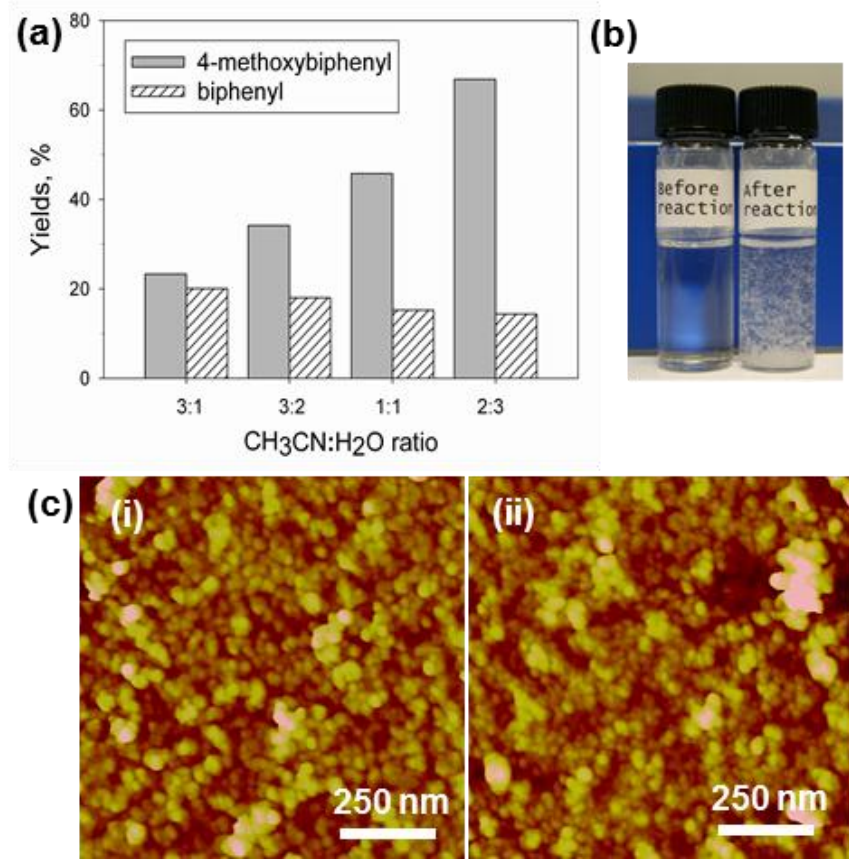


Figure 5.2. The Effect of Solvent Ratio on Reaction Selectivity and Surface Characterization by AFM

Reaction condition: iodoanisole 10 mM, phenylboronic acid 10 mM, sodium carbonate 30 mM, 5 ml CH₃CN/H₂O mixture, temperature 50 °C. (a) The effect of solvent CH₃CN/H₂O volume ratio on reaction selectivity. (b) Products precipitation at room temperature. (c) AFM images of Pd-TMV chip after reaction in CH₃CN/H₂O mixed solvent with volume ratio of 3:2 (i) and 2:3 (ii).

To further verify the effect of solvent ratio (CH₃CN/H₂O) on the coupling reaction selectivity, another boronic acid compound, 4-methoxyphenylboronic acid (10 mM), was examined as an alternative reactant to the phenylboronic acid for the Suzuki coupling reaction in the presence of iodobenzene (10 mM) and one

Pd-TMV chip. As shown in Table 5.1, the reactions were carried out under two different solvent conditions with identical reaction time and temperature. In CH₃CN:H₂O=3:2, the final yields of 4-methoxybiphenyl (cross-coupling) and 4,4'-dimethoxy-1,1'-biphenyl (homo-coupling) are 32.7% and 10.8%, respectively. When the CH₃CN/H₂O ratio was changed to 2:3, the yield of cross-coupling product increased to 51.2%, while the homo-coupling product yield decreased to 8.2% under the same reaction conditions. This clear difference in the reaction selectivity under different solvent ratios is consistent with the one with phenylboronic acid, and shows that higher water content leads to higher selectivity towards the cross-coupling pathway. Therefore, the selectivity from the solvent effect appears to be general and not limited to phenylboronic acid.

Table 5.1. Solvent Ratio Effect on Selectivity of Coupling Reaction

Entry	Reactants ratio (mM) IC ₆ H ₅ : CH ₃ OC ₆ H ₄ B(OH) ₂ : Na ₂ CO ₃	Solvent	Yield of cross-coupling product (C ₆ H ₅ - C ₆ H ₄ OCH ₃), %	Yield of homo-coupling product (CH ₃ OC ₆ H ₄ - C ₆ H ₄ OCH ₃), %
1	10:10:30	CH ₃ CN:H ₂ O=3:2	32.7	10.8
2	10:10:30	CH ₃ CN:H ₂ O=2:3	51.2	8.2

Reaction time:24h; Reaction temperature:50 °C; Stirring speed: 600 rpm

To further confirm the effect of water content on the homo-coupling pathway, reactions with only phenylboronic acid in the absence of iodoanisole were also carried out under two types of solvent mixtures ($\text{CH}_3\text{CN}/\text{H}_2\text{O}=2:3$ and $3:2$). As shown in Table 5.2, the yield of biphenyl decreased from 31.1% to 16.8% when the $\text{CH}_3\text{CN}/\text{H}_2\text{O}$ solvent ratio changed from $3:2$ to $2:3$. Apparently, in this case, higher water content in the solvent mixture also inhibited the homo-coupling pathway even in the absence of the other reactant iodoanisole, which is consistent with the trend found in the presence of iodoanisole (Figure 5.2(a)).

Table 5.2. Solvent Ratio Effect on Homo-coupling Reaction

Entry	Reactants ratio (Mm) $\text{C}_6\text{H}_5\text{B}(\text{OH})_2 : \text{Na}_2\text{CO}_3$	Solvent	Yield of homo-coupling product ($\text{C}_6\text{H}_5-\text{C}_6\text{H}_5$), %
1	10:30	$\text{CH}_3\text{CN}/\text{H}_2\text{O}=3:2$	31.1
2	10:30	$\text{CH}_3\text{CN}/\text{H}_2\text{O}=2:3$	16.8

Reaction time: 24h; Reaction temperature: 50 °C; Stirring speed: 600 rpm.

There has been limited number of studies with contradictory conclusions on the effect of water on the selectivity of Suzuki reaction.^{74,222} The results in Figure 5.2 (a) and table 5.1 and 5.2 show that a $\text{CH}_3\text{CN}/\text{H}_2\text{O}$ mixture with the appropriate ratio is crucial in directing cross- vs. homo-coupling pathways, leading to efficient selectivity control. In-depth studies on the mechanism of this striking effect of water content on the selectivity are currently underway.

Importantly, no catalytic conversion was observed for several negative controls (e.g. no chip, gold chip and TMV-assembled gold chip) examined under the same reaction conditions (0% conversion for all). This clear difference in conversion demonstrates the catalytic activity of TMV-templated palladium nanoparticles in the Suzuki coupling reaction.

Next, the photograph of Figure 5.2(b) shows that both 4-MB and BP products were precipitated as white flocculates while cooling the reaction mixture to room temperature due to their relatively low solubility in CH₃CN/H₂O (2:3) mixture. The products can thus be separated by centrifuge or sedimentation upon completion of the reaction, highlighting an additional advantage of the high water content condition enlisted here. Importantly, this result illustrates the facile and robust nature of this chip-based catalyst format that enables the simple separation of both catalysts and products upon reactions without additional steps such as centrifugation or filtration, as compared to homogeneous Pd catalysts.^{20,70}

Next, to qualitatively evaluate the surface morphology and stability of Pd-TMV chip under the conditions employed, the chips were simply taken out of the reaction mixture and analyzed by AFM, as shown in Figure 5.2(c). Compared to the AFM image of the Pd-TMV chip before the catalytic reaction (Figure 5.1(c)-(ii)), chips after the reaction in various CH₃CN/H₂O ratios (Figure 5.2(c)) show no apparent changes in the Pd loading density or particle size. This preliminary

examination indicates that the surface-assembled Pd-TMV complexes were stable under the range of reaction conditions studied. Combined, the results in Figure 5.2 show clear reactivity and selectivity, stability of the nanostructured Pd-TMV catalyst chips, along with facile catalysts and products separation for the Suzuki coupling reaction.

5.4. Surface Characterization by GISAXS

As shown in Figure 5.3, I next employed grazing incidence small angle X-ray scattering (GISAXS) to further examine the stability of Pd-TMV chips in the Suzuki reaction. First, the schematic diagram of Figure 5.3(a) shows a typical GISAXS setup where the incident X-ray strikes the surface of the Pd-TMV chip and the scattered rays are recorded at low angles (less than 2°) on a 2D CCD detector.¹⁸⁶ Figure 5.3(b) shows scattering images of various samples as a function of the scattering angles 2θ in the horizontal direction and α_f in the vertical direction. First, the TMV1cys-assembled gold chip (i) shows strong scattering in the out-of-plane direction (at $2\theta=0$), characteristic of the rod shaped TMV.¹⁴⁵ Second, the Pd-TMV chips before (ii) and after (iii and iv) reactions all show nearly identical isotropic scattering, rising from abundant spherical Pd particles. This result clearly indicates that most Pd particles and Pd-TMV complexes were well-preserved after completion of the Suzuki reactions under different solvent ratios ($\text{CH}_3\text{CN}/\text{H}_2\text{O}=2:3$ and $3:2$) at 50°C .

Next, a Guinier analysis^{158,186,187} was employed to further examine the average Pd particle diameters. For this, scattering curves were first created by making a horizontal line-cut of intensity (shown by the red line in Figure 5.3(b)-(ii)) and plotting intensity vs. the scattering vector, q_{xy} . The table in Figure 5.3(c) shows that the average Pd particle diameter did not change significantly under all the reaction conditions examined, with slight variations rising from different Pd-TMV chips for the *ex-situ* GISAXS analysis.

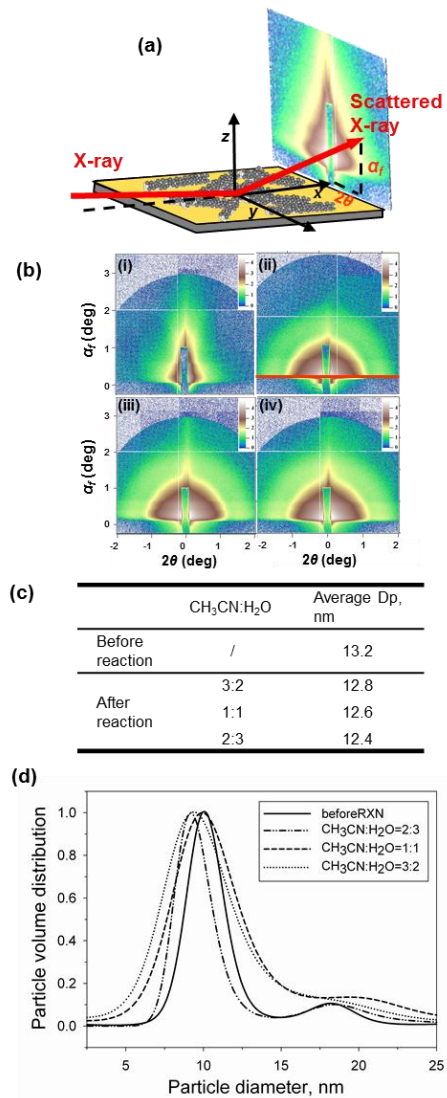


Figure 5.3. Pd Particle Size Distribution of Pd-TMV Catalyst Examined by GISAXS

(a) Schematic diagram of GISAXS. (b) Scattering patterns of TMV-gold chip (i), Pd-TMV chip before reaction (ii), Pd-TMV after reaction in CH₃CN/H₂O solvent with ratio of 2:3 (iii) and 3:2 (iv). (c) Summary of average Pd particle size on Pd-TMV chip before and after reaction. (d) Pd particle size distribution of Pd-TMV chips before and after reactions. Y-axis represents normalized number density of Pd nanoparticles n(R)

Finally, normalized particle volume distributions of Pd-TMV chips before and after reactions under different reaction conditions were examined by simulating size distributions from the scattering curves using Irena software. The Irena software utilizes the Maximum Entropy Method (MEM) with a 15% error allowance to simulate particle size distributions.¹⁸⁸ As shown in Figure 5.3(d), the average Pd particle size remained nearly identical upon completion of the reactions in all three solvent ratios examined, which further confirms the results in Figure 5.3(c) acquired from Guinier analysis. While the particle size distribution for all three samples appears to broaden upon reaction, I note that the *ex-situ* GISAXS measurements without direct comparison to the same pre-reaction chips may not provide reliable means to examine the change in particle size distribution. The reaction mechanism of the Suzuki reaction is generally considered to occur by a small number of molecular Pd species that leach out into the bulk solution, which then re-deposit rapidly onto supports.⁶⁸ These consistent particle size retention results in Figure 5.3 show no apparent disappearance of the original particles or increase of larger size particles (through Ostwald ripening) that may lead to different size distributions and larger average particle sizes.

5.5. Batch Reaction Profile

Figure 5.4 shows the reactants conversion and products yield curves at 50 °C. For this, Suzuki reaction of 10 mM iodoanisole with 15 mM phenylboronic acid was

carried out in the presence of Pd-TMV chips in 5 ml CH₃CN/H₂O (2:3) mixture for 24 hours. Samples were taken at certain intervals and analyzed with HPLC as described above.

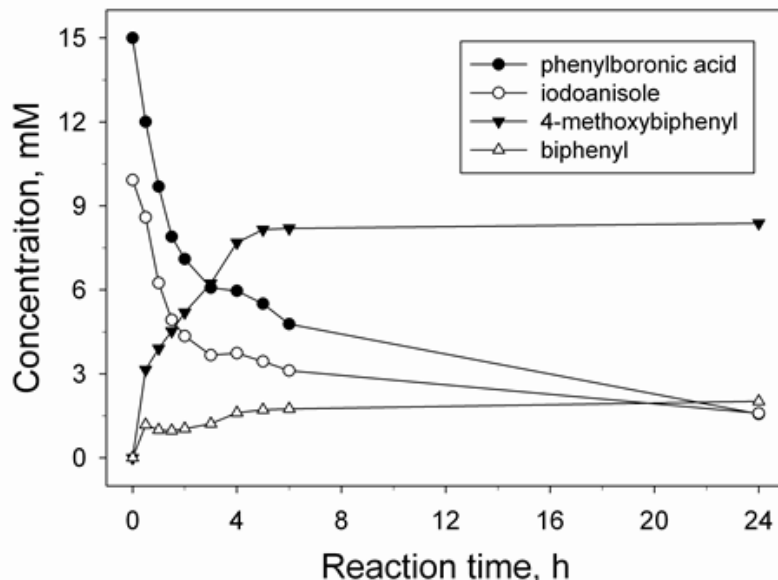


Figure 5.4. Concentration of Reactants and Products vs. Reaction Time

Reaction condition: iodoanisole 10 mM, phenylboronic acid 15 mM, sodium carbonate 30 mM, 5 ml CH₃CN/H₂O mixture solvent with ratio of 2:3, temperature 50 °C

The concentration of both reactants (iodoanisole and phenylboronic acid) decreased rapidly in the first 2 hours, and then decreased slowly until the end of the reaction. Meanwhile, the target product 4-MB started forming rapidly in the first 0.5 hours and kept increasing steadily until the 4th hour. After 5 hours, the 4-MB concentration reached the maximum value of 8.2 mM and didn't change

significantly until the end of the reaction. A similar trend was observed for the formation of BP. The curves show that the majority of both products (4-MB and BP) were formed within the first 5 hours, which is sufficient for near-complete conversion of IA at 50 °C. In addition, the reaction time didn't affect the reaction selectivity. Meanwhile, further in-depth Inductively Coupled Plasma Optical Emission Spectrometry (ICP-OES) experiments revealed the total Pd amount per chip to be 8.3 µg, which leads to the Pd catalyst ratio of 0.15 mol% based on iodoanisole (0.05 mmol per batch). Furthermore, the “apparent” reaction rate within the first 5 hours was determined to be 0.0165 mol/(min·g) based on this amount of Pd employed for each batch reaction

Meanwhile, Suzuki reactions at lower reaction temperatures (25 and 40 °C) were also examined and yielded much slower reaction rates (data not shown). Therefore, a moderately high temperature clearly facilitated the Pd-TMV catalyzed Suzuki reaction.

5.6. Effect of Reactant Ratio on the Reaction Conversion

To further investigate the effect of reactant ratio (iodoanisole (IA):phenylboronic acid (PBA):base) on the product yields, I carried out Suzuki reactions with different reactant concentrations in CH₃CN/H₂O (2:3) mixture, as shown in Figure 5.5.

I first studied the influence of PBA amount on the product yields by keeping IA and base concentration constant (Entries 1-4). In Entry 1, equivalent amount of two reactants IA and PBA (both 10 mM) resulted in only 68.6% yield of 4-MB. When PBA concentration was increased from 10 mM to 20 mM from Entry 1 to 3, both 4-methoxybiphenyl (4-MB) and biphenyl (BP) yields increased simultaneously. Entry 3 shows that two-fold higher concentration of PSB than IA leads to 100% yield of 4-MB and 29.6% of BP. Meanwhile, further addition of PBA up to 30 mM (Entry 4) didn't have a significant influence on either reaction conversion or selectivity. The mass balance analysis based on HPLC quantification indicated that all BP was formed from the homo-coupling of PBA. These results indicate that more PBA content than IA is needed to complete the cross-coupling reaction, since a certain amount of PBA follows the homo-coupling pathway catalyzed by Pd^{223,224} or Au²²⁵ as previously reported.

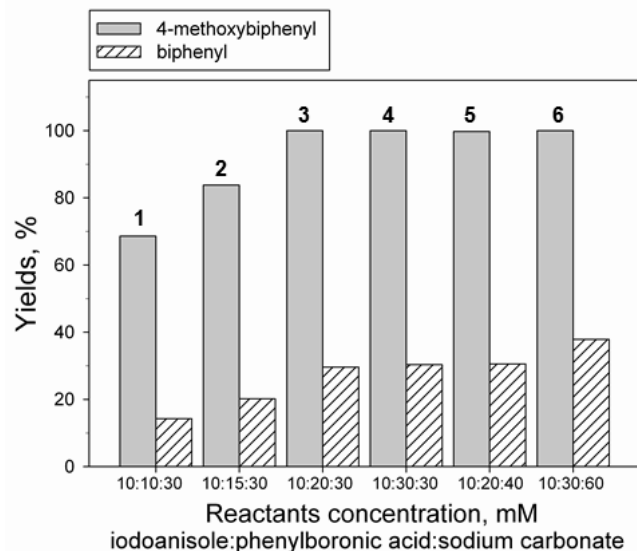


Figure 5.5. Effect of Reactants Ratios on Product Yields

Reactions were carried out with Pd-TMV chips at solvent ratio of $\text{CH}_3\text{CN}/\text{H}_2\text{O}=2:3$ and temperature 50°C .

Next, the effect of base (Na_2CO_3) amount was investigated (Entries 5 and 6).

Compared to Entry 3, 33% higher base concentration (Entry 5) yielded similar final product amounts. A two-fold higher base amount (Entry 6, 60 mM) yielded 8% more byproduct (BP) than Entry 4, showing relatively lower reaction selectivity. It is well known that base could activate phenylboronic acid in the Suzuki coupling reaction;²²⁶ the results shown here indicate that excess base may lead to more homo-coupling byproducts while certain amount of base is required to complete the cross-coupling reaction. Overall, the results in Figure 5.5 demonstrate that proper reactant ratio plays an important role on both reaction conversion and selectivity.

5.7. Reusability of Pd-TMV Catalysts

As shown in Figure 5.6, I further conducted recycle reaction studies to examine the reusability of these Pd-TMV catalysts based on the clear stability shown via GISAXS in Figure 5.3. For this, Pd-TMV chips were thoroughly rinsed with deionized water and applied to three more batch reaction cycles without any regeneration treatments. The reactions were carried out in the optimized conditions as described above, with 10 mM IA, 20 mM PBA and 30 mM base in CH₃CN/H₂O (2:3) solvent at 50 °C for 24 h. The results in Figure 5.6 show a small decrease in the catalytic activity of Pd-TMV chip in the second cycle: the yield of 4-MB decreased from 100% (first run) to 91.7% (second run) and BP decreased from 29.6% to 28.8%. However, the third and fourth batches did not show a further decrease in activity, as shown in the fourth reuse of catalysts: the yield of 4-MB was maintained at 91.4%. These results are consistent with my findings in the dichromate reduction reaction,^{202,203} and clearly demonstrate the stability and reusability of Pd-TMV catalysts for the Suzuki reaction under the conditions studied. More importantly, the surface-assembled TMV-templated format enables the significantly simpler recovery and repeated use of the catalysts (*i.e.* mechanical removal of the chip from the reaction mixture) with minimal loss of catalytic activity without arduous separation and/or regeneration procedures.

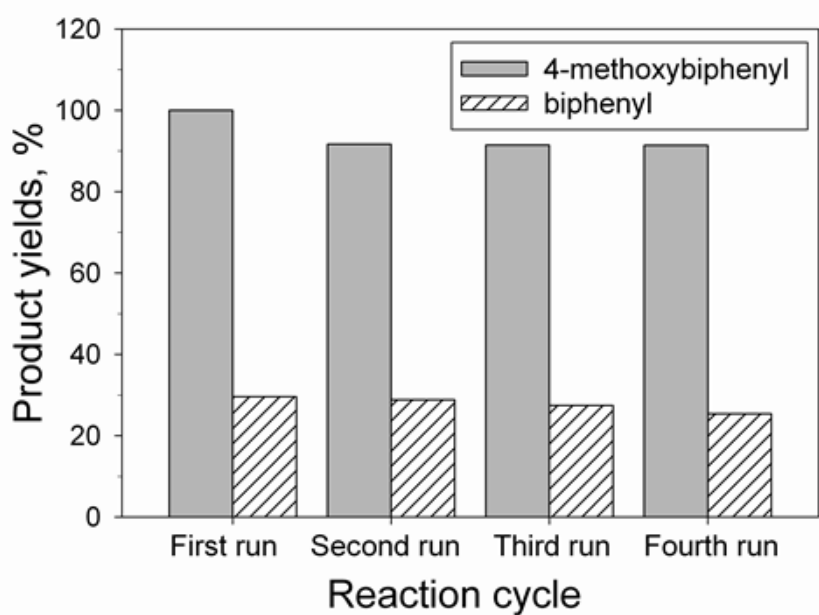


Figure 5.6. Recycling Test of Pd-TMV Chip Catalyzed Suzuki Reaction of Iodoanisole with Phenylboronic Acid

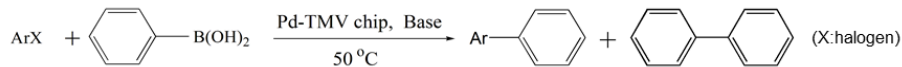
5.8. Catalytic Suzuki Reaction of Other Aryl Halides with Phenylboronic Acid

Finally, I further examined the conversion and selectivity of the Pd-TMV catalyzed Suzuki reaction for a range of aryl halides as summarized in Table 5.3. Entries 1 and 2 show that Pd-TMV catalysts are active for the cross-coupling of PBA with bromoanisole, but not chloroanisole. This result is consistent with previous reports, where the relative cross-coupling reactivity decreased in the order of I > Br >> Cl.^{4,68} Next, Entries 3-6 show the Suzuki reaction of 4-

iodophenol with PBA, where the solvent ratio also played a significant role on the reactivity. Higher water content (Entry 3 vs. 4) produced more of the cross-coupling product 4-phenylphenol (80%) and less biphenyl (14%), which is consistent with the trend shown in Figure 5.2 for iodoanisole. Contrary to other reports,²²¹ iodophenol is only slightly soluble in water, thus no product was observed in aqueous solution (Entry 6). Meanwhile, the commonly used dimethylacetamide (DMA)/water (1:1) mixture^{74,222} (Entry 5) did not yield significant conversion for this catalytic reaction. Next, Suzuki reactions using benzene halides were also studied (Entries 7 and 8). The reaction with iodobenzene (Entry 7) led to 133.7% yield (vs. initial iodobenzene) of biphenyl, most likely from both the cross-coupling (between iodobenzene and PBA) and the homo-coupling reactions (between two moles of PBA). The reaction with bromobenzene in Entry 8 showed a much lower conversion, as expected from the lower reactivity of bromides.

Considering the unoptimized reaction conditions for each reactant case shown in Table 5.3, higher product yields could be expected upon further examination of parameters (e.g. solvent ratio, base addition amount, reactants ratio). Overall, these studies show that these TMV-templated Pd catalysts are active with several different reactants examined, further confirming the general catalytic activity for Suzuki coupling reactions.

Table 5.3. Pd-TMV Chip Catalyzed Suzuki Reaction of Aryl Halides with Phenylboronic Acid



Entry	ArX	Solvent ^a	Base	Concentration (mM) ArX: C ₆ H ₅ B(OH) ₂ : Base	Yield of Ar-C ₆ H ₅ , %	Yield of C ₆ H ₅ -C ₆ H ₅ , %
1	4-BrC ₆ H ₄ OCH ₃	CH ₃ CN:H ₂ O=2:3	Na ₂ CO ₃	10:30:60	30.8	29.9
2	4-ClC ₆ H ₄ OCH ₃	CH ₃ CN:H ₂ O=2:3	Na ₂ CO ₃	10:30:60	0	10.9
3	4-IC ₆ H ₄ OH	CH ₃ CN:H ₂ O=1:3	Na ₂ CO ₃	10:20:30	80.0 ^b	14.0
4	4-IC ₆ H ₄ OH	CH ₃ CN:H ₂ O=2:3	Na ₂ CO ₃	10:20:30	68.4 ^b	30.5
5	4-IC ₆ H ₄ OH	DMA:H ₂ O=1:1	K ₂ CO ₃	10:10:30	0	0
6	4-IC ₆ H ₄ OH	H ₂ O	K ₂ CO ₃	10:10:30	0	0
7	IC ₆ H ₅	CH ₃ CN:H ₂ O=1:1	Na ₂ CO ₃	10:20:30	/	133.7 ^c
8	BrC ₆ H ₅	CH ₃ CN:H ₂ O=1:1	Na ₂ CO ₃	10:20:30	/	53.0

^aSolvent ratios are all based on volume ratio

^bThe yield of Ar-C₆H₅ is calculated from the conversion of IC₆H₄OH on a basis of mass balance.

^cByproduct from homo-coupling of C₆H₅B(OH)₂ is the same as cross-coupling product, so the yield of biphenyl based on iodobenzene is higher than 100 %.

5.9. Preliminary Study of the Reaction Mechanism via Chip Removal during Reactions

Due to the surface-assembled format, the Pd-TMV catalyst chips are good candidates to examine the nature and role of potential active species in Suzuki coupling reaction by simply removing the chips in the middle of the reaction and continuing the reaction monitoring. To identify the catalytically active species, coupling reaction of iodoanisole with phenylboronic acid with different

experimental designs were carried out as shown in Figure 5.7. For this, three individual experiments were conducted: (i) in the presence of Pd-TMV chip throughout the reaction, (ii) taking the Pd-TMV chip out of the reaction solution after 1 h, (iii) taking the Pd-TMV chip out after 2 h, as shown in Figure 5.7(a). After the first reaction cycle, these chips were thoroughly rinsed, then reused for the next reaction cycle without any regeneration treatment in Figure 5.7(b) under three conditions; (i) without taking the Pd-TMV chip out, (ii) taking out the chip at 0.5 h, (iii) taking out the chip at 1 h. The reaction products were then closely monitored for 8 hours.

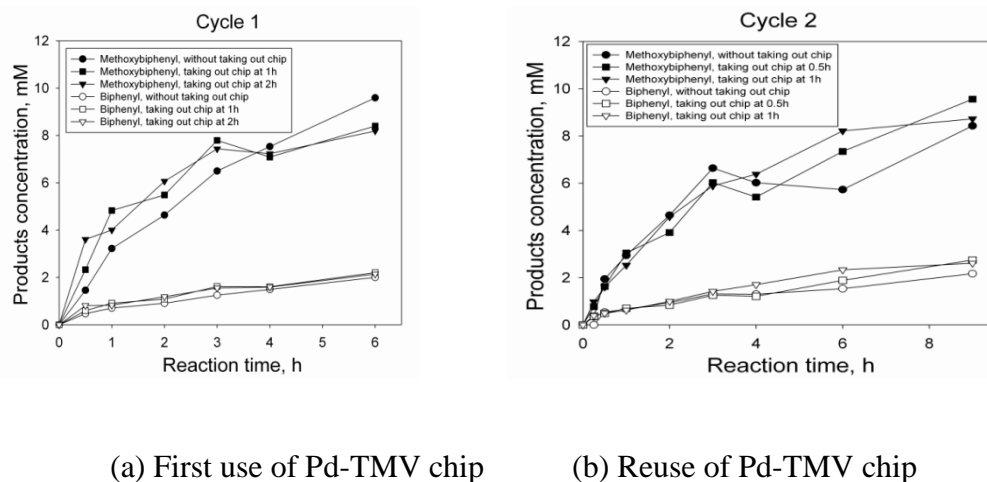


Figure 5.7. Mechanism Investigation of Suzuki Reaction
 Iodoanisole : Phenylboronic acid : Sodium carbonate=10 mM: 20mM:30mM,
 Acetonitrile/Water=2:3, Reaction temperature: 50 °C, Reaction time: 24h, Stirring speed: 600 rpm.

As shown in Figure 5.7(a), the Suzuki reaction continued after the Pd-TMV chips were removed from the reaction mixture after 1 hour (case (ii)) or 2 hours(case (iii)), and both the cross-coupling and homo-coupling products continued increasing for 8 hours examined. The product conversion curves from the cases (ii) and (iii) are very close to the case in the presence of Pd-TMV chips throughout the reaction (case (i)). Similarly, for the second reaction cycle, the Suzuki coupling reactions upon the removal of Pd-TMV chips also proceeded with equivalent reaction rate as in the first case, as shown in Figure 5.7(b). These results suggest that the coupling reaction may be catalyzed largely by Pd species in the reaction solution (presumably leached Pd molecular species or small clusters), instead of Pd nanoparticles on the chips. Importantly, this chip-based catalyst format enabled these mechanistic studies in a drastically simple manner (i.e. mechanical removal of the chips from the reaction mixture) without arduous catalysts separation procedures.

Based on these findings, ICP-OES was employed again on the reaction mixtures in order to further confirm the presence of Pd in the reaction solution, as shown in Table 5.4. For this, the reaction mixtures were evaporated until completely dry, and then treated with aqua regia solution for 1 hour and diluted by water, as described above.

Table 5.4. Leached Pd Amount Determined by ICP

		Experiment methods	Pd in reaction solution, μg/ml (ppm)	
Reaction cycle 1	Case (i)	without taking out chip	0.07	
	Case (ii)	taking out chip at 1h	0.09	
	Case (iii)	taking out chip at 2h	0.05	
Reaction cycle 2	Case (i)	without taking out chip	0.05	
	Case (ii)	taking out chip at 0.5h	0.002	Below DL
	Case (iii)	taking out chip at 1h	0.001	Below DL

First, Table 5.4 shows that the Pd concentrations in the solution at the end of reaction cycle 1 from three different cases were consistently low (0.05-0.09 ppm), within the same order of magnitude as the Pd detection limit (0.044 ppm) of the ICP-OES equipment. In the second reaction cycle, the Pd concentrations at the end of reaction are even less (in the ppb level), with the cases (ii) and (iii) being below the detection limit (only 1-2 ppb). While being inconclusive due to the low concentrations close to the detection limit, these ICP results suggest that such trace amounts of Pd may exist in the reaction mixtures, consistent with the chip removal results shown in Figure 5.7. Several studies have shown that trace amounts of Pd in the ppm or ppb level are responsible for the catalytic activity, and sufficient to catalyze Suzuki coupling reactions.^{227,228} The chip removal and ICP results shown here thus suggest that the Pd-TMV chip-based Suzuki reaction

may be catalyzed largely by the soluble Pd active species as in other nanoparticle-based systems.^{68,229} Based on these previous findings, we speculate that Pd atoms may be released/leached from the surface of Pd nanoparticles, leading to the formation of Pd(II) or Pd(0) molecular species that subsequently react with aryl halides.^{78,230} The Pd nanoparticles formed on TMV-assembled chip here can therefore be considered as a reservoir, or “pre-catalysts”^{68,230,231} of the catalytically active species in the reaction solution. Finally, we caution that very small number of loosely bound Pd nanoparticles may detach from the chips and interfere with these experiments, despite the clear overall stability confirmed via both GISAXS and XPS in this study.

5.10. Conclusions

In this chapter, I examined the catalytic activity of TMV-templated Pd nanoparticles for the Suzuki coupling reaction toward value-added chemical synthesis for the first time. The surface-assembled chip based format allowed for simple catalyst and product separation as well as simple catalysts recycling for several reaction batches. Over 90% of the initial catalytic activity was retained for four reaction cycles. In depth reaction condition studies indicated that the solvent ratio played an important role in the selectivity of the Suzuki reaction, and that a higher water content is beneficial for the cross-coupling pathway.

Importantly, these results suggest that the viral template-based bottom-up assembly approach may lead to facile catalyst synthesis and separation.

6. Integration of Catalytically Active Viral-Palladium Nanostructures into Polymeric Hydrogel Microparticles via Replica Molding

6.1. Introduction

Metal nanoparticles play an important role in catalysis due to their irregular surfaces, high surface area to volume ratio and size-dependent properties, which can be tuned to optimize catalytic activity and selectivity. Palladium (Pd) is an important precious metal catalyst for a wide range of chemical reactions^{44,232,233}. The synthesis of small, uniform, well-dispersed and catalytically active Pd nanoparticles under mild conditions in a predictable and controlled manner is an unmet challenge, despite recent developments in the dispersion and stabilization of Pd nanoparticles^{18,20,24,29,31,33}. Meanwhile, biological supramolecules such as viruses^{140,172-175} and protein cages^{234,235} have gained substantial attention as alternative template materials for the controlled synthesis of metal and metal oxide nanoparticles due to their well-defined structure, monodispersed nature, and abundant surface functionalities that can be further modified via chemical and/or genetic modifications. Particularly, Tobacco Mosaic Virus (TMV) has been extensively utilized due to their robust tubular structure and stability in a wide range of conditions (e.g. pH between 2 and 10, temperature up to 90°C and

organic solvents such as 80% ethanol) as well as safety and simple mass production^{141,143,144,157,236}. Furthermore, genetically displayed cysteines on TMV coat proteins have been shown to improve Pd nanoparticle formation rising from the enhanced biosorption of the precursors^{42,156,237}. However, the use of reducing agents (e.g. dimethylamineborane (DMAB), sodium borohydride (NaBH₄)) leads to large and often uncontrollable Pd nanoparticle formation, with a few exceptions such as on surface-assembled formats^{158,202,203,238}, resulting in inefficient use of the expensive metal precursors for potential applications such as catalysis. Recently, Lim et al.^{159,239} reported the controlled synthesis of Pd coatings with thickness of 25-35 nm on TMV biotemplates in the absence of external reducer. While these studies present potential for the controlled synthesis of functional nanomaterials, substantially smaller and well-dispersed nanoparticles are required for catalytic applications. For example, compared with larger nanoparticles, 1-2 nm Pd nanoparticles supported in large pores of mesocellular foam with lower metal loading showed higher selectivity and reactivity for amine racemization²⁴⁰.

In the meantime, seamless integration of novel nanocatalysts with robust platforms that confer stability, scalable production, and ease of separation and recovery while allowing ready access of the reactants remains a formidable challenge. Polymeric supports, especially in the form of porous 3D hydrogel microparticle formats, should provide improved molecular interactions and offer a

hydrophilic environment with more favorable solution kinetics²⁴¹. The ability to customize specific microparticle features, such as controlled dimensions, anisotropic shapes and added functionalities (e.g. magnetic properties^{83,84}), would further enhance the utility of the catalysts integrated in such hybrid materials as alternative means for separation from bulk solution, patterning, or self-assembly. Recently, polymeric hydrogels have been used as stabilizing platforms for viral or metal nanoparticles, and even served as effective templates for the in-situ synthesis of metal nanocatalysts (such as Co, Ni, Cu, Ag)^{82,88,90,91}. Particularly, polyethylenglycol (PEG) with large chain length has been emerging as both reducer and stabilizer for the synthesis of Pd nanoparticles in the studies of aerobic alcohol oxidation^{96,97}, selective hydrogenation reaction^{98,99} and Heck reaction¹⁰⁰. PEG is relatively inexpensive, non-volatile, nontoxic and environmentally benign. In addition, the physical properties (e.g. mesh size) of PEG-based hydrogels can be readily controlled simply by varying the molecular weight (M_w) and structure (linear vs. branched) of the PEG used²⁴². Thus, PEG-based hydrogels present significant potential as stabilizers or matrixes for the fabrication of functional materials with catalytic activities.

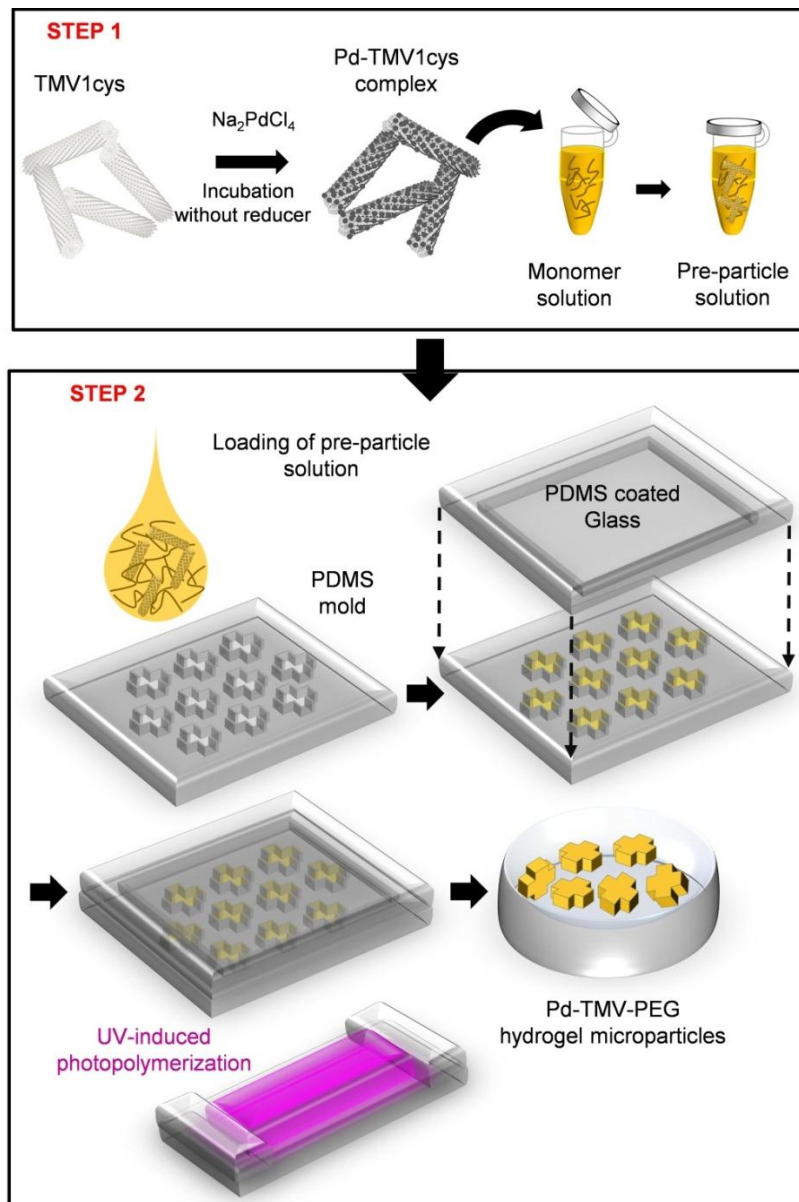


Figure 6.1. Synthesis of Pd-TMV Encapsulated PEG Microparticles by Replica Molding(RM)

Step 1: Spontaneous Pd nanoparticle formation without reducing agent.
 Step 2: Microparticle fabrication via replica molding technique

In this Chapter, I present a simple approach for the synthesis of small, uniform and highly active Pd nanocatalysts on TMV biotemplates (Pd-TMV) in the absence of reducing agents. I also present that these novel nano-bio materials can be readily integrated into PEG hydrogel microparticle platforms via simple and robust replica molding (RM)-based fabrication technique. As shown in the schematic diagram of Figure 6.1, this synthesis-fabrication procedure consists of two steps. First, simple mixing of TMV with Pd precursor solution at 50 °C for half an hour leads to spontaneous formation of small (1-2 nm), uniform, well-dispersed and highly crystalline Pd nanoparticles along TMV biotemplates without externally added reducer in aqueous solution under mild conditions (Step 1). In-depth analysis via Transmission Electron Microscopy (TEM) shows that the concentrations of both Pd precursor and TMV as well as the ratio between these two are important factors for the uniform and exclusive coating of Pd nanoparticles along TMV biotemplates. Second, the as-prepared Pd-TMV complexes are readily integrated into PEG polymeric hydrogel microparticles via simple and robust replica molding (RM) technique (Step 2). Specifically, the Pd-TMV complexes are mixed with poly(ethylene glycol) diacrylate (PEG-DA) and photoinitiator to yield preparticle solution, then placed on PDMS micromolds. Brief irradiation of UV light induces radical chain polymerization to form crosslinked PEG-based hydrogel microparticles containing the Pd-TMV

complexes integrated into the polymeric networks in a stable manner (Step 2). These hybrid microparticles, named Pd-TMV-PEG microparticles, are then utilized for the catalytic reduction of hexavalent chromate ion, a prevalent industrial waste pollutant in drinking water⁵¹. The catalytic reaction study of Pd-TMV-PEG microparticles shows 6-fold higher activity than commercial Pd/C catalysts per Pd mass. Furthermore, the results show that the reaction rate is linearly proportional to the Pd loading density inside Pd-TMV-PEG hydrogel microparticles within the diffusion limitation-free regime. Compared to microfluidic particle fabrication techniques^{101,104,124}, RM allows for simple, robust, scalable and inexpensive integration and manufacturing. In addition, RM technique enables the encapsulation of Pd-TMV complexes in PEG hydrogel microparticles with high Pd loading capacity without clogging or precipitation²⁴³, commonly found in the microfluidic procedures. Combined these results illustrate a facile synthesis-fabrication strategy for robust, highly uniform and catalytically active nano-bio-polymeric hybrid materials in a controlled manner. I envision that the results and methods presented in this Chapter can be readily expanded to a variety of other systems for facile fabrication of multifunctional materials with novel nano-bio components.

6.2. Materials and Methods

6.2.1. Materials

Genetically modified Tobacco Mosaic Virus (TMV1cys) was extracted from infected tobacco leaves with phosphate extraction buffer, followed by chloroform phase separation, PEG8000 sedimentation and sucrose gradient¹⁷⁸. Sodium tetrachloropalladate (II) (Na_2PdCl_4 , Sigma-Aldrich, St. Louis, MO) was used as the precursor for the Pd nanoparticle formation. Poly(ethylene glycol) diacrylate (PEG-DA, $M_n=700$), PEG ($M_n=200$), and 2-hydroxy-2-methylpropiophenone (Darocur[®] 1173, photoinitiator (PI)) were purchased from Sigma-Aldrich (St. Louis, MO). 0.5%Tween 20 solution was used for microparticle storage. Potassium dichromate ($\text{K}_2\text{Cr}_2\text{O}_7$) (99.5%, Sigma-Aldrich) and sodium formate (HCOONa) (99%, Fisher Scientific, Waltham, MA) were used in the study of dichromate reduction. All of these materials were used as received without further purification.

6.2.2. Spontaneous Formation of Pd Nanoparticles on TMV Biemplates and Preparticle Solution Preparation

To form Pd nanoparticles on TMV biemplates, the TMV stock solution was added into the Na_2PdCl_4 solution, then incubated at 50 °C for 30 min. Various concentrations of Na_2PdCl_4 and TMV were studied for the spontaneous formation

of Pd nanoparticles on TMV, as shown in Table 6.1 and Figure 6.3(d). For the catalytic activity study, the Pd-TMV complexes were all synthesized with the condition of sample S6 (0.6 mg/ml TMV, 10 mM Na₂PdCl₄). The mixed solution was centrifuged at 10,000 rpm for 5 min with a Microfuge 22R centrifuge (Beckman Coulter, Brea, CA). The supernatant was discarded and the collected brown Pd-TMV complex pellets were resuspended in 55 µl deionized water. After 5 min sonication, the Pd-TMV solution was mixed with 15 µl PEG200 to make solution **1**. To make solution **2**, 25 µl PEGDA was thoroughly mixed with 5 µl PI. Both solutions **1** and **2** were treated with 5 min sonication. Next, solution **1** was added into solution **2** to have 100 µl preparticle solution with final volume ratio of Pd-TMV solution/ PEGDA/PEG200/PI as 55/25/15/5. In order to make preparticle solutions with TMV final concentration of 0.3, 0.6, 1.2, 2.4 and 4.8 mg/ml, 50, 100, 200, 400 and 800 µl of the Pd-TMV solutions (0.6 mg/ml TMV, 10 mM Na₂PdCl₄) were centrifuged, and the collected pellets were resuspended in 55 µl DI water, mixed with PEG200, then added to solution **2** to obtain 100 µl total volume of preparticle solutions..

Table 6.1. The Synthesis Conditions of Pd Spontaneous Formation on TMV Biotemplates

Sample number	Na ₂ PdCl ₄ , mM	TMV1cys, mg/ml	Ratio between Pd/TMV
S1	2	1.565	1.3

S2	2	0.125	16
S3	5	0.6	8.3
S4	10	1.56	6.4
S5	10	1.2	8.3
S6	10	0.6	16.7
S7	10	0.3	33.3
S8	15	0.6	25
S9	20	1.565	12.8
S10	20	0.125	160

6.2.3. Fabrication of Pd-TMV-PEG Microparticles via Replica Molding

The four major steps of soft lithography, as described by others¹⁰⁷, were followed to prepare the microparticles. Briefly, AutoCAD was used to design the shaped patterns. High-resolution printing was used to generate photomasks on transparency films for the fabrication of silicon masters via photolithography. PDMS elastomeric micromolds were formed with Sylgard 184 (Dow Corning, Midland, MI) following a 24 h cure at 65 °C. Finally, microparticles were fabricated from the PDMS elastomeric micromolds via replica molding (RM).

As shown in Figure 6.1, prepolymer solution (100 µl) was first placed on the surface of the PDMS micromolds (2080 wells per 2 cm × 2 cm mold). Each

cross-shape microparticle has arms of length 100 μm , depth of 100 μm and total width of 300 μm . The volume of each well is 5 nanoliter. The air bubbles in the microwells were removed by rubbing plastic pipette tips against the PDMS molds. After the removal of the excess preparticle solution, the filled PDMS micromolds were then sealed in a humidity chamber ($\geq 90\%$ relative humidity) with a glass slide coated with a thin layer of PDMS obtained via spin-coating for 30 s at 1000 rpm. A square section (same size as the microwell square region within the micromold) of PDMS of this slide had been removed from the glass slide to provide a small gap between the glass surface and the top portion of the microwells. The sealed micromolds were then placed on an aluminum mirror (Thorlabs, Newton, NJ) and exposed to 365 nm UV light with an 8 W handheld UV lamp (Spectronics Corp., Westbury, NY) for 15 min. The polymerized PEG microparticles with encapsulated Pd-TMV complexes (Pd-TMV-PEG microparticles) were collected from the microwells by first physically bending the mold, then placing water containing 0.5% (v/v) Tween 20 on the mold surface. The microparticles were collected by pipetting up and down a few times before transferring into a storage vial. This particle removal with water was repeated several times for the complete collection of microparticles. The prepared Pd-TMV-PEG microparticles are stored in 0.5% (v/v) Tween 20 solution at room temperature until catalytic reaction studies.

6.2.4. High-resolution Transmission Electron Microscopy (HRTEM)

Characterization

The samples for the HRTEM characterizations were prepared as follows: 10 µl of well-dispersed Pd-TMV solution was placed onto 300 mesh copper grid carbon TEM grids (FCF300-Cu, EMS Sciences, Hatfield, PA), and left to dry before examination. The TEM analysis was carried out on a JEOL 2100 TEM at 200 kV at the Center for Nanoscale Systems (CNS) at Harvard University (Cambridge, MA).

6.2.5. Imaging Analysis

The Pd-TMV-PEG microparticles were visualized with an Olympus BX51 microscope (Chroma Technology Corp., Rockingham, VT), and the brightfield micrographs were captured with a DP70 microscope digital camera.

6.2.6. Inductively Coupled Plasma Atomic Emission Spectroscopy (ICP-OES)

The Pd loading densities of the Pd-TMV-PEG hydrogel microparticles containing various TMV concentrations were determined by ICP-OES. For this, before hydrogel encapsulation, centrifuged Pd-TMV complex pellets were mixed with aqua regia solution (HCl : HNO₃ (v:v) = 4:1) for acid digestion. After complete

dissolution of Pd-TMV complexes for about 5 min, the acid-digested solutions were analyzed by Perkin Elmer 7300 ICP-OES (PerkinElmer Inc., Waltham, MA). As shown in Table 6.2, the Pd loading densities of the Pd-TMV-PEG microparticles with various concentrations of TMV were determined based on the Pd amounts added into the preparticle solutions.

Table 6.2. The Pd Loading Densities of Pd-TMV-PEG Microparticles with Various TMV Concentrations

TMV concentration inside microparticles, mg/ml	0	0.3	0.6	1.2	2.4	4.8
Pd loading density, $\mu\text{g Pd}/\mu\text{L microparticles}$	0	0.035	0.071	0.141	0.282	0.564

6.2.7. Catalytic Activity Examination of Pd-TMV-PEG Microparticles

Dichromate reduction was employed to examine the catalytic activity of Pd-TMV-PEG microparticles. For this, microparticles (total volume=5.2 μl) was added into 1 ml reaction solution containing 0.1 mM potassium dichromate and 100 mM sodium formate at pH 3. The reaction was monitored in-situ with EvolutionTM 300 UV/vis Spectrophotometer (Thermo scientific, Waltham, MA) every minute at 350 nm, the characteristic absorption maximum of the dichromate ion. The absorbance at 350 nm was used to calculate Cr(VI) ion concentration, using a calibration curve derived from standard solutions. The conversion of

Cr(VI) was calculated from $([\text{Cr(VI)}_0] - [\text{Cr(VI)}]) / \text{Cr(VI)}_0 \times 100\%$, where $[\text{Cr(VI)}_0]$ is the original concentration before reaction and $[\text{Cr(VI)}]$ is the concentration at each time point. The reaction can be considered to follow pseudo first-order kinetics under the reaction conditions in this study. From the linear regression of $\ln([\text{Cr(VI)}]/[\text{Cr(VI)}_0])$ vs. reaction time, the obtained slope represents the apparent first-order rate constant²⁰³.

6.3. Spontaneous Formation of Palladium Nanoparticles along TMV Biotemplates

As shown in Figure 6.2, small, well-dispersed and highly crystalline palladium (Pd) nanoparticles form on tobacco mosaic virus (TMV) biotemplates in the absence of reducing agent. First, macroscopic and UV-Vis absorbance observations over 30 min incubation period in Figure 6.2 clearly indicate the conversion of Pd precursors into Pd-TMV complexes that can be readily separated via low-speed centrifugation. For this, 10 mM Na_2PdCl_4 (Pd precursor) was mixed with 0.6 mg/ml TMV1cys in deionized (DI) water and incubated at 50 °C for 30 min.

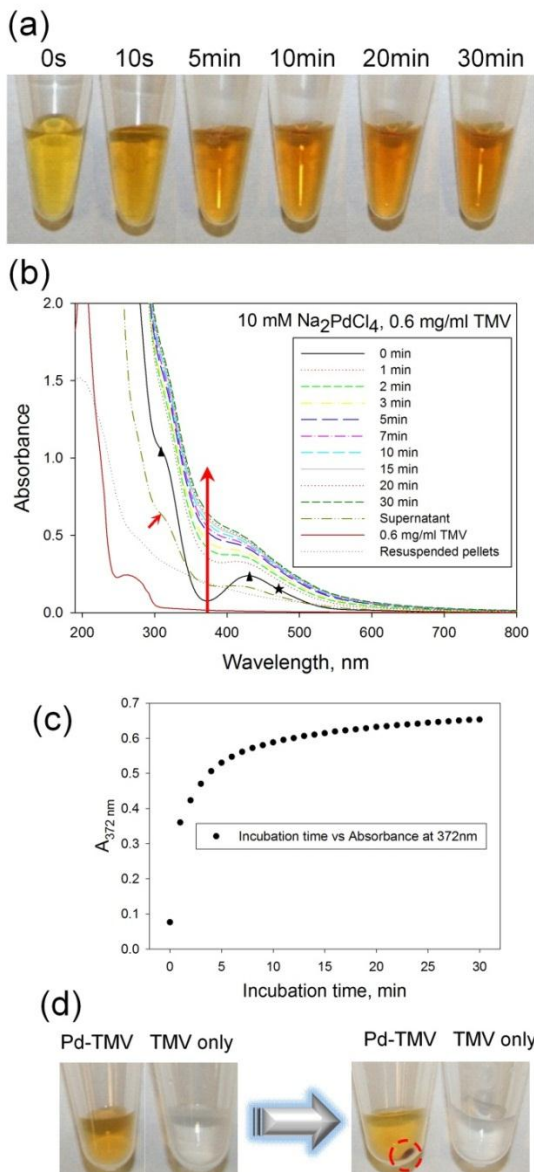


Figure 6.2. Spontaneous Pd Nanoparticle Formation on TMV Biotaemplates

(a) Photographs of Pd-TMV solution over incubation time at fixed temperature 50 °C. (b) UV-vis absorbance of Na_2PdCl_4 solution after mixing with TMV at 50 °C over time (0.1 cm path depth cell). (c) $A_{372 \text{ nm}}$ vs incubation time. (d) Pd-TMV complex pellets collection. Red dash circle highlights the collected Pd-TMV pellets.

As shown in the photographs of Figure 6.2 (a), the color of the solution quickly turned from light yellow into golden yellow within 10 seconds, then into darker brown yellow slowly over time during the incubation. Next, the UV absorbance spectra in Figure 6.2(b) imply the formation of Pd-TMV complexes. At time zero (solid black line), the UV spectrum of Pd precursor solution shows characteristic absorbance peaks at 320 nm and 430 nm (marked with solid triangle), which are due to the charge-transfer and d-d transition of $\text{PdCl}_3(\text{H}_2\text{O})^-$. Meanwhile, the spectrum also shows very strong absorbance below 300 nm and a small shoulder peak at around 475 nm (marked with solid star), which are due to the presence of PdCl_4^{2-} ^{239,244}. The spectrum of TMV solution (red solid curve) shows TMV's typical absorbance at 260-280 nm (aromatic proteins and RNA). After Pd precursor solution was mixed with TMV, those characteristic absorbance peaks of PdCl_4^{2-} and $\text{PdCl}_3(\text{H}_2\text{O})^-$ become indistinguishable as the incubation proceeds, and are replaced by an increased absorbance over a broad wavelength range. We tracked this change in the spectra by taking the absorbance values at the initial minimum at 372 nm over time, as shown in Figure 6.2(c). This plot suggests that the conversion of the precursor proceeds rapidly within the first five minutes then gradually reaches a plateau under the condition employed in this study. Potential causes of this behavior could be the changes in pH of the solution¹⁵⁹ or the thermodynamic equilibrium in which TMV biotemplates may have reached

maximum capacity for the spontaneous formation of Pd nanoparticles. But this behavior is unlikely due to the exhaustion of the Pd precursor as indicated by the remaining Pd precursor in the supernatant solution (shown in the UV-vis absorbance curve in Figure 6.2(b)).

Finally, the photographs of Figure 6.2(d) show that the Pd-TMV complexes are readily centrifuged at low speed (10000 rpm) to yield brown pellets (highlighted with red dash circle) in contrast to TMV solutions that show no pelletting. The UV-Vis spectrum of the collected supernatant (dash-dot-dot line pointed with short arrow) upon 30 min incubation shows similar yet lower absorbance compared to the initial Pd precursor solution, while the resuspended pellets (black dotted line) show apparent shift of absorbance peak into lower wavelength range along with the absence of the 430 nm $\text{PdCl}_3(\text{H}_2\text{O})^-$ peak, indicating the formation of Pd-TMV complexes³⁸. Combined these results in Figure 6.2 indicate that the Pd-TMV complexes form mostly within the first five minutes.

6.4. TEM Characterization

Next, I thoroughly examined the synthesis conditions and the structures of palladium nanoparticles on TMV biotemplates via TEM as shown in Figure 6.3. For this, TMV was exposed to the Pd precursor (Na_2PdCl_4) solution and incubated

at 50 °C for 30 min. The collected pellets were suspended in DI water then placed on the TEM grids.

First, the TEM images of Figure 6.3(a) show minimal number of Pd particles for samples prepared with low Pd precursor concentrations (S1: 2 mM Na₂PdCl₄, 1.6 mg/ml TMV). Next, Figure 6.3(b) shows that the sample with higher Pd precursor concentrations (S6: 10 mM Na₂PdCl₄, 0.6 mg/ml TMV) exhibits the formation of interlocking networks as well as abundant and small Pd nanoparticles formed exclusively on TMV biotemplates. Importantly, the histogram of the Pd nanoparticle sizes based on 100 particles shown in the inset of Figure 6.3(b) reflects narrow size distribution of 1.2±0.3 nm diameter with about 82 % of the Pd particles in the size range of 0.6-1.5 nm. Finally, sample with even higher Pd precursor ratio (S7: 10 mM Na₂PdCl₄ and 0.3 mg/ml TMV) in Figure 6.3(c) shows large flower-like Pd aggregates outside the TMV biotemplates, while many Pd particles also form on TMV biotemplates with uniform particle size and narrow distribution (Figure 6.5). These results indicate that: (1) certain threshold concentration of Pd precursor is needed for the spontaneous formation of nanoparticles along TMV biotemplates, (2) good dispersion of uniform Pd nanoparticles requires adequate amount of TMV biotemplates as support, and (3) extra amount of Pd precursor doesn't lead to the increase in Pd nanoparticle size on TMV biotemplates.

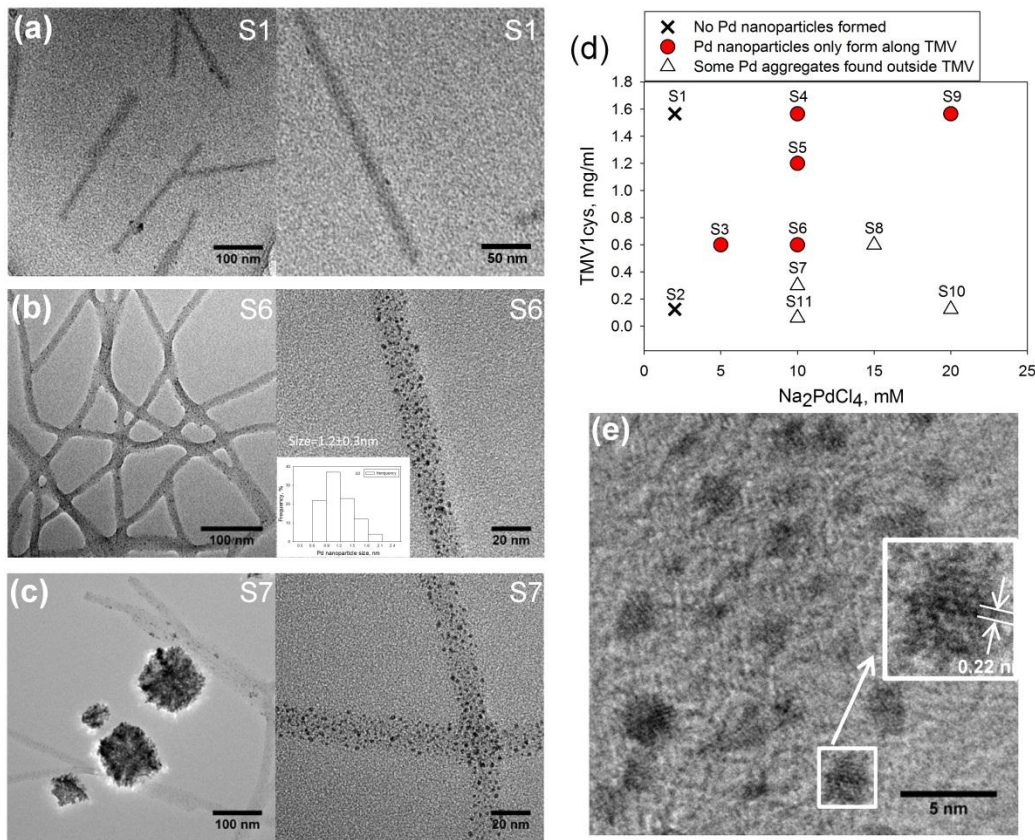


Figure 6.3. TEM Images of Pd Nanoparticles Spontaneously Formed along TMV Biotemplates

(a) Sample S1 (2 mM Na₂PdCl₄ and 1.6 mg/ml TMV). (b) Sample S6 (10 mM Na₂PdCl₄ and 0.6 mg/ml TMV) (c) Sample S7 (10 mM Na₂PdCl₄ and 0.3 mg/ml TMV) (d) The effect of TMV and Na₂PdCl₄ concentrations on Pd nanoparticle formation along TMV biotemplates. (e) Crystal structure of Pd nanoparticles (prepared with S6 condition)

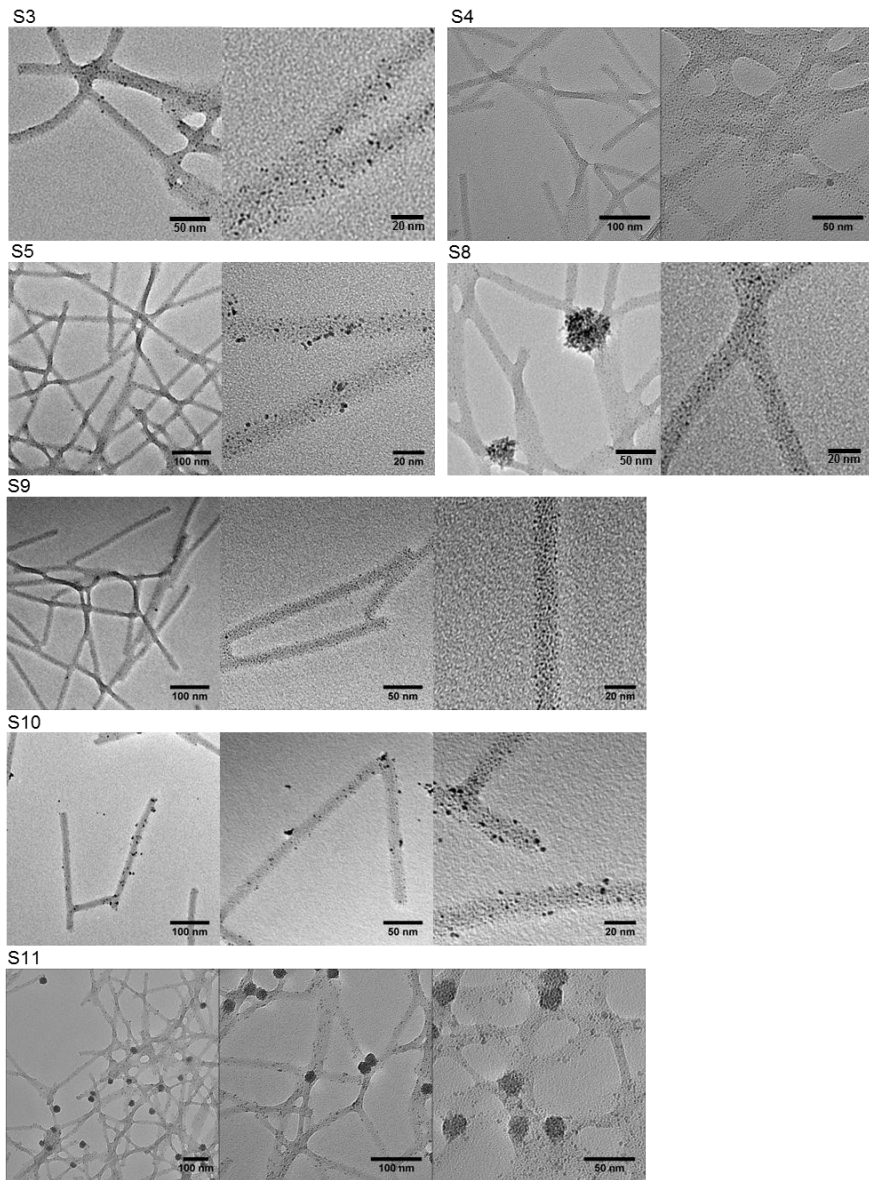


Figure 6.4. TEM Images of Pd Nanoparticles Spontaneously Formed along TMV Biotemplates under Various Synthesis Conditions

The behavior of Pd nanoparticle formation on TMV biotemplates under various Na_2PdCl_4 and TMV concentrations is summarized in Figure 6.3(d). First, when the Na_2PdCl_4 concentration is as low as 2 mM, no visible Pd nanoparticles were formed on the TMV biotemplates (samples S1 and S2, marked as cross symbols). Second, under certain conditions with adequate concentration and proper ratio of Na_2PdCl_4 and TMV, small Pd nanoparticles form only on TMV biotemplates in a uniform and well-dispersed manner (samples S3, S4, S5, S6 and S9, marked as red round circles). The TEM images of additional samples (S3, S4, S5 and S9) are shown in Figure 6.4, and the average sizes of Pd nanoparticles for those samples are all measured to be between 1-2 nm with narrow size distribution (Figure 6.5). Sample S3 and S5 synthesized with the same ratio of Na_2PdCl_4 /TMV (8.3 mmol Pd/g TMV) exhibit nearly the same particle size distribution and average size of 1.7 nm, as shown in Figure 6.5. In addition, in comparison with sample S6 ($\text{Na}_2\text{PdCl}_4/\text{TMV} = 16.6$ mmol Pd/g TMV), the decrease in the $\text{Na}_2\text{PdCl}_4/\text{TMV}$ ratio (sample S3 and S5) results in about 1.5-fold decrease in the number of Pd nanoparticles per unit surface area of TMV.

Third, when the TMV concentration is relatively low, large aggregates of Pd particles are found outside TMV biotemplates (samples S7, S8, S10, and S11, marked as triangles in Figure 6.3(d)). The TEM images of samples S8, S10, and S11 are also shown in Figure 6.4. Combined, the results summarized in Figure

6.3(d) indicate that the concentrations of both Na_2PdCl_4 and TMV, and the ratio between Na_2PdCl_4 and TMV play important roles for the formation of small and uniform Pd nanoparticles along TMV biotemplates, with the optimal ratio of $\text{Na}_2\text{PdCl}_4/\text{TMV}$ (mmol Pd/g TMV) between 6.25 and 17.

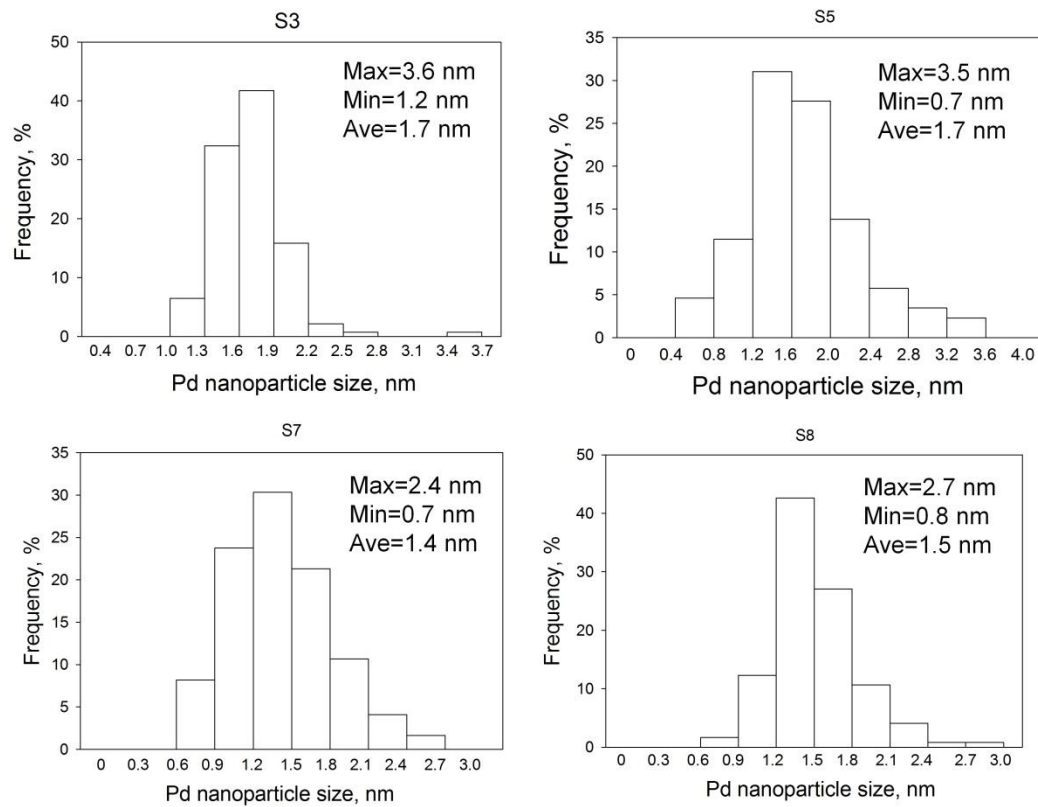


Figure 6.5. Pd Nanoparticle Size Distribution of Samples Prepared with Various Synthesis Conditions

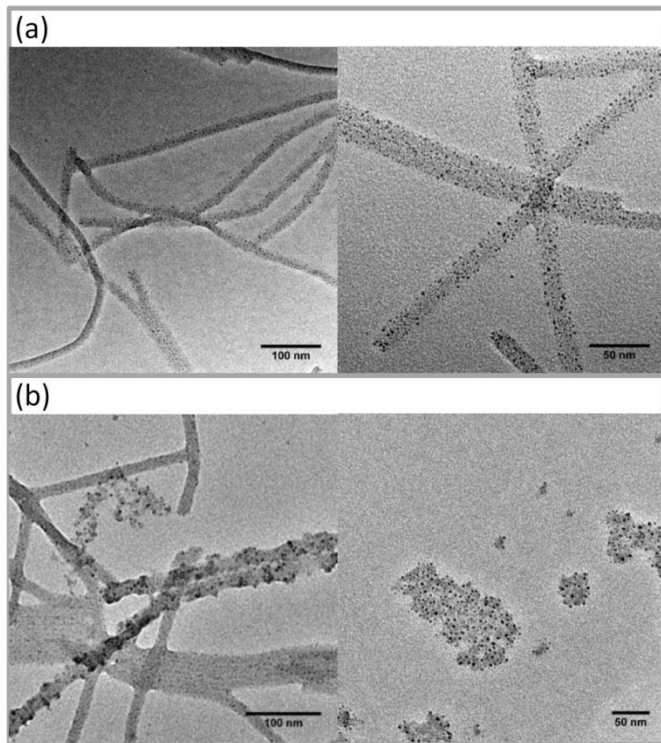


Figure 6.6. Effect of Incubation Time on the Pd Formation on TMV

(a) 1 hour incubation (b) 2 hour incubation. 10mM Na₂PdCl₄, 0.6mg/ml TMV1cys. Incubation temperature=50 °C

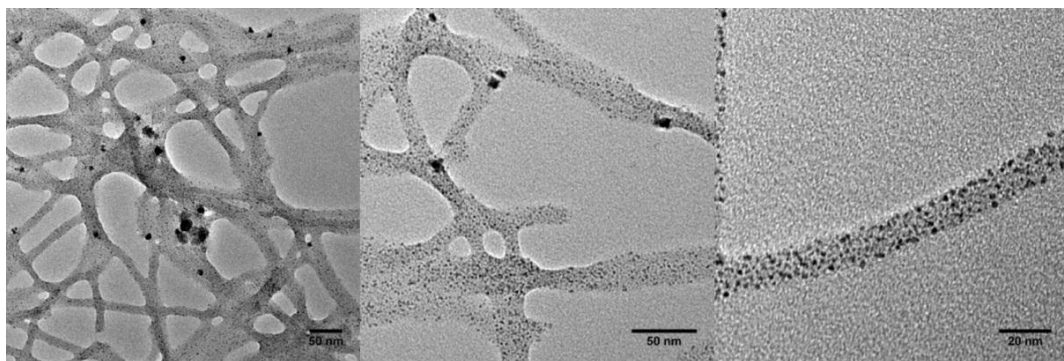


Figure 6.7. Effect of Incubation Temperature on the Pd Formation on TMV

Incubation temperature=80 °C. 10mM Na₂PdCl₄, 0.6mg/ml TMV1cys.
Incubation time= 30 min. Note: The Pd-TMV solution looks very cloudy before centrifuge.

In addition, the effects of incubation time and temperature were also studied as shown in the TEM images of Figures 6.6 and 6.7. I found that longer incubation time does not lead to changes in Pd particle size or distribution, yet causes certain degree of TMV degradation. Higher incubation temperature (80 °C) shows apparent particle aggregation and does not lead to the increase in Pd particle size. Thus, variation of preparation parameters has minor influence on the Pd size distribution in the presence of TMV, similar to the studies on the formation of colloidal Pd particles in the presence of PVP by Wolf and coworkers ³⁸.

Finally, the high resolution TEM image of a randomly selected area (Figure 6.3(e)) shows that most Pd nanoparticles formed on TMV biotemplates are highly crystalline. The Pd particle in the inset shows 0.22 nm spacing, which corresponds to the (111) interplanar distance of the face centered cubic (fcc) structure of metallic Pd crystals.

The results in Figure 6.3 exhibit several benefits of TMV as biotemplates for the metal nanoparticle formation. First, TMV provides abundant bio-adsorption, nucleation and particle growth sites^{101,156,178,236} for the formation of small (1-2 nm) Pd nanoparticles with narrow size distribution under mild aqueous conditions without externally added reducer. Second, TMV's robust 3D nanotubular

structure keeps the Pd nanoparticles well-dispersed^{42,143} throughout centrifugation and resuspension, while the TMV rods form stable networks without aggregation upon Pd metal formation under proper incubation conditions. This network formation of Pd-TMV complexes further facilitates simple separation via centrifugation.

Lim et al.¹⁵⁹ demonstrated the formation of polycrystalline palladium layers with thickness of 25-35 nm on the outer surface of TMV in the absence of reducer via several repeated coating cycles. In the study shown here, ~20 fold higher concentrations of both Na₂PdCl₄ and TMV (with proper concentration and ratio) and only one incubation cycle leads to a completely different behavior, where uniform 1-2 nm Pd nanoparticles are formed in a consistent manner. This spontaneous formation of Pd nanoparticles on TMV may follow complex formation and self-mineralization mechanism, where PdCl_x(H₂O)_y precursors are complexed on the TMV surface functionalities (thiol and hydroxyl groups) and self-mineralized by oxidizing Cl⁻ to release HClO²³⁹. This study here along with previous reports^{159,236,239} indicates that the absence of reducing agent in the process leads to slow nanoparticle growth with more uniform crystalline structures. From our observation of the UV-vis absorbance spectra, the formation of Pd-TMV complexes takes as long as 20 min for ~ 95% of completion. In another report by Lim et al.²³⁹, the incubation time for the Pd adsorption and

mineralization without reducer was also 20 min. In contrast, applying reducer in the TMV solution leads to more rapid and uncontrolled Pd particle formation with some large multicrystalline palladium aggregates outside TMV^{42,101,143,156,178,236}. In the Small-angle X-ray Scattering (SAXS) study reported by Monacchi et al.²³⁶, the Pd growth on TMV with sodium hypophosphite as the reducer was complete within only 33 seconds, leading to relatively large (up to 5 nm) Pd particles. Therefore, the reducer-free procedure shown here represents a simple and low-cost approach for the controlled formation of uniform and small Pd nanoparticles along TMV biotemplates.

In summary, results in Figure 6.3 demonstrate that: (1) small (1-2 nm) and uniform Pd nanoparticles are spontaneously formed along TMV biotemplates without reducing agents, (2) most Pd nanoparticles observed are highly crystalline with (111) facets, and (3) both concentration and ratio between Na₂PdCl₄ and TMV are important factors for the formation of uniform and well-dispersed Pd-TMV complexes.

6.5. Fabrication of Hybrid Hydrogel Microparticles with Encapsulated Pd-TMV Complexes via Replica Molding

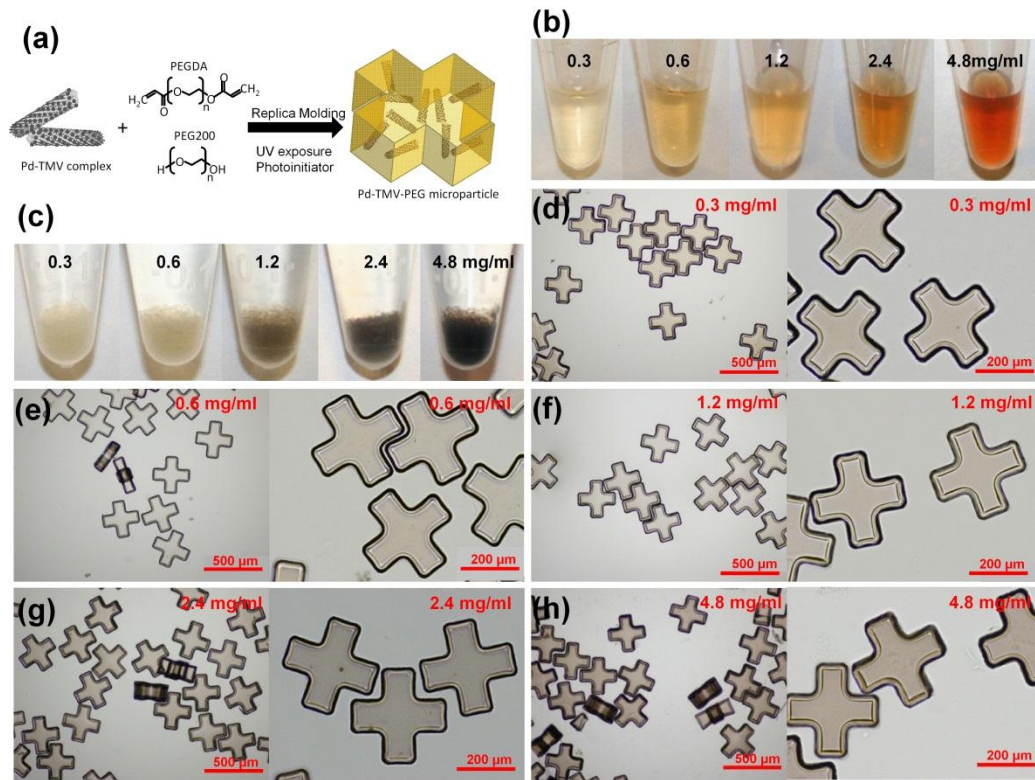


Figure 6.8. Microphotographs of Pd-TMV-PEG Microparticles

(a) Brief schematic diagram of Pd-TMV encapsulated PEG microparticle fabrication. (b) Preparticle solutions; (c) Pd-TMV encapsulated PEG microparticles. (d) Micrographs of Pd-TMV-PEG microparticles containing various concentration of TMV. PEGDA: PEG200: PI: Pd-TMV(Volume ratio) = 25:15:5:55.

Next, the as-prepared Pd-TMV complexes can be readily integrated into non-spherical polymeric microparticle formats via simple replica molding (RM) technique, as shown in Figure 6.8. As shown in the schematic diagram of Figure

6.8(a), the preparticle solution composed of the Pd-TMV complexes, poly(ethylene glycol) diacrylate (PEGDA), PEG200, and photoinitiator (PI) is poured into the PDMS-based micromolds. The volume ratio of Pd-TMV solution/PEGDA/PEG200/PI is set as 55/25/15/5, while the final TMV concentration in the microparticles are varied, as shown in Figure 6.8(d)-(h). Upon irradiation with UV light, the preparticle solution undergoes photo-induced radical polymerization to form crosslinked polymeric networks^{245 246}.

First, the photographs in Figure 6.8(b) show that the preparticle solutions are clear and uniform with final TMV concentration up to 4.8 mg/ml, with increasingly brown color for higher Pd-TMV contents. Next, the photographs of the Pd-TMV embedded PEG microparticles in Figure 6.8(c) show increasingly dark color with increasing Pd-TMV contents, indicating that the Pd-TMV complexes are successfully embedded in the PEG hydrogels. Finally, the photomicrographs of the Pd-TMV-PEG microparticles in Figures 6.8(d)-(h) show uniform color and shape for all the Pd-TMV contents examined up to 4.8 mg/ml TMV concentration without any apparent aggregation or deformation, with highly consistent dimensions of 300 μm in width and 100 μm in thickness. The SEM images in Figure 6.11 further confirm the uniformity of the fabricated microparticles and the smoothness of microparticle surfaces. Various preparticle compositions were also studied for the microparticle fabrication; the microphotographs in Figures 6.9

and 6.10 clearly show that insufficient concentrations of PEGDA (<15%) and PI (2%) result in the incomplete photopolymerization, non-uniform microparticles or weak mechanical strength.

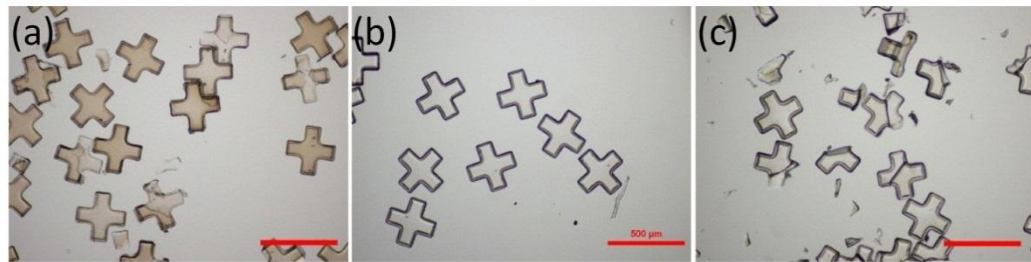


Figure 6.9. Effect of PEGDA % (v/v) on Particle Fabrication

Volume ratio of PEGDA: PEG200: PI: Pd-TMV is (a) 10:30:5:55 (b) 30:10:5:55 (c) 40:0:5:55.

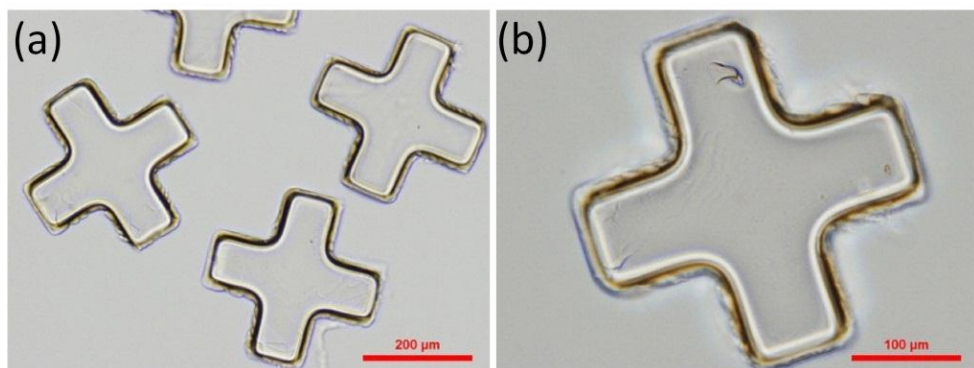


Figure 6.10. Effects of Photoinitiator (PI) Concentration on Particle Fabrication

PEGDA: PEG200: PI: Pd-TMV=15:25:2:58

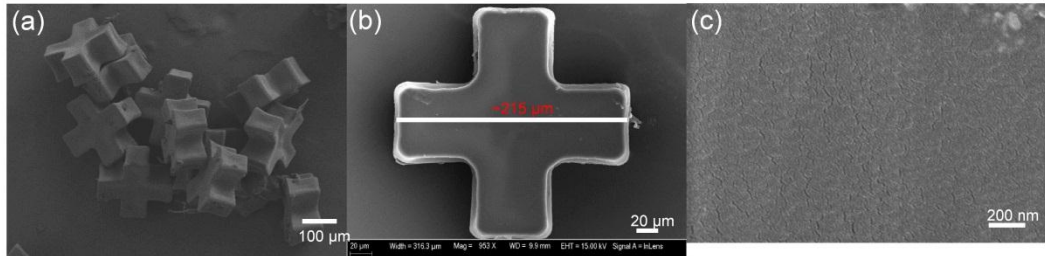


Figure 6.11. Scanning Electron Microscope (SEM) of critical point dried Pd-TMV-PEGDA microparticles

Fabrication composition PEGDA:PEG200:PI:Pd-TMV solution =25:15:5:55. Microparticle contains 0.6 mg/ml TMV-Pd complex inside.

Compared to microfluidic techniques for the microparticle fabrication¹⁰¹, the results in Figure 6.8 shows many inherent advantages of the RM technique, including simple, robust, and inexpensive procedures as well as scalability and reliable duplication of complex structures²⁴⁵. First, the RM procedure is simple due to the usage of a hand-held UV lamp for photopolymerization rather than a high-intensity UV source requiring delicate control for the photolithographic or microfluidic fabrication procedures^{104,247}. Second, the RM procedure is robust due to the tunable fabrication parameters not limited by needs to maintain consistent flows, the viscosity and phase separation. Third, all the silicon master molds, PDMS micromolds, and excess preparticle solution can be fully recycled, making the RM technique a cost-efficient procedure. Fourth, RM leads to the fabrication of 100% uniform and clean microparticles due to the absence of any continuous phase (e.g. oil and unreacted monomer outside of the objective light)⁸³

or deformed particles that often arise at the onset and end of each microfluidic procedure. In conclusion, these results clearly indicate that the Pd-TMV complexes can be readily integrated into polymeric microparticle formats in a simple and highly reproducible manner via RM technique.

6.6. Catalytic Activity Examination

Next, as shown in Figure 6.12, the catalytic activity of the Pd-TMV-PEG hydrogel microparticles for Pd nanoparticle-catalyzed dichromate reduction reaction was examined. For this, Pd-TMV-PEG microparticles (5.2 μ l microparticles for each reaction batch) encapsulating various amounts of Pd-TMV complexes (Figure 6.12) were added to, and vigorously stirred in the 1 ml reaction mixtures containing 0.1 mM $K_2Cr_2O_7$ and 100 mM NaCOOH at pH 3. The conversion was monitored via UV-Vis spectrophotometry at the dichromate ion's characteristic absorption maximum at 350 nm.

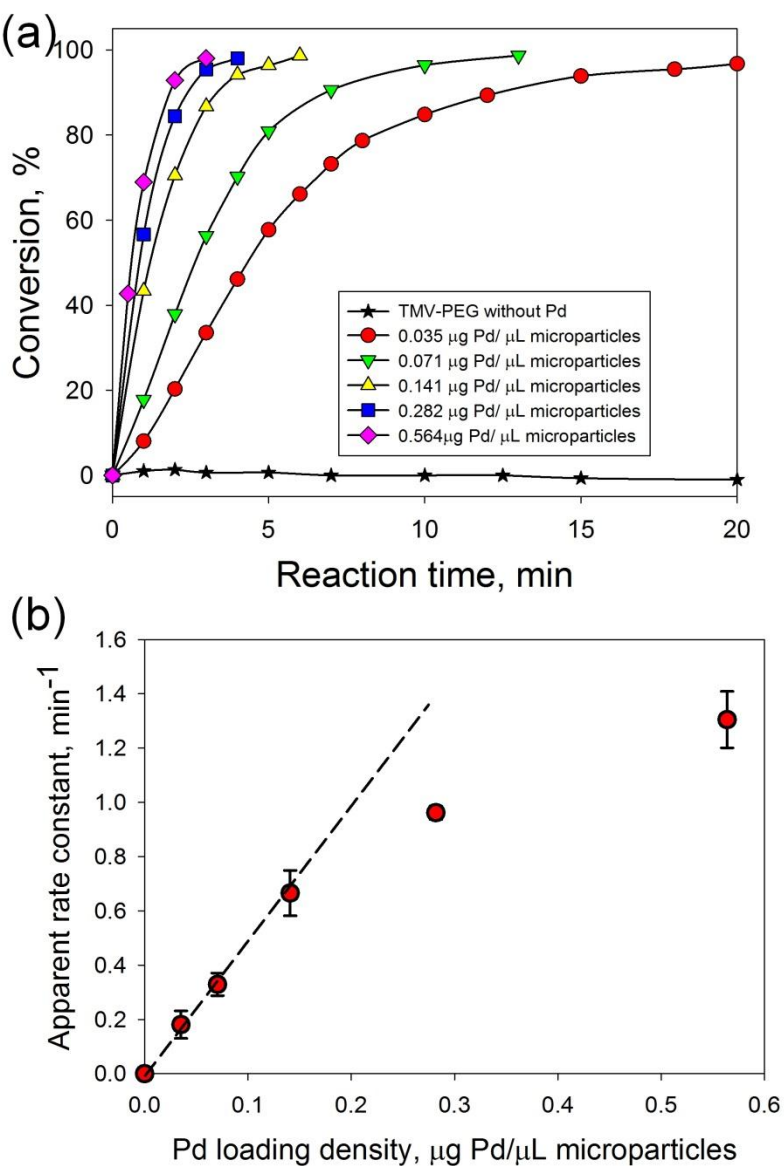


Figure 6.12. Catalytic Activities of Pd-TMV-PEG Microparticles Encapsulating various Amounts of Pd-TMV Complexes

(a) Conversion curves of dichromate reduction catalyzed by Pd-TMV-PEG microparticles with various Pd loading densities. (b) Pd loading densities in Pd-TMV-PEG microparticles versus apparent reaction rate constants. Note: the Pd loading amount is measured by ICP measurement. Preparticle solution composition PEGDA: PEG200: PI: Pd-TMV(v/v/v)=25:15:5:55.

First as shown in Figure 6.12(a), the bottom conversion curve with star symbol is from the microparticles containing only TMV without Pd coating, which shows no dichromate conversion. Meanwhile, all the other PEG microparticles containing Pd-TMV complexes show good catalytic activities with the conversions reaching near-completion within the 20 min period. The Pd-TMV-PEG microparticles containing higher Pd loading density clearly show higher conversion rates.

Under the reaction conditions applied, the reaction follows apparent first-order kinetics²⁰³, and the apparent rate constants k_{app} (min^{-1}) of all batches were obtained from the slope of linear regression of $\ln([\text{Cr(VI)}]/[\text{Cr(VI)}_0])$ vs. reaction time, where Cr(VI) and Cr(VI)_0 represent the dichromate concentration at time t and 0 respectively. As shown in Figure 6.12(b), triplicate reaction experiments were carried out for each Pd loading density condition, and the average k_{app} was plotted against the Pd loading density of the microparticles. The small error bars for each condition indicate the high consistency and reproducibility of this synthesis-fabrication procedure. Furthermore, the k_{app} is proportional to the Pd loading density when Pd loading density is lower than 0.141 $\mu\text{g Pd}/\mu\text{l}$ microparticles. In this linear region, the observed reaction rate is equal to the intrinsic reaction rate catalyzed by Pd-TMV-PEG microparticles fabricated with

composition of PEGDA: PEG200: PI: Pd-TMV(v/v/v/v)=25:15:5:55, which is calculated to be 98.7 mmol/(g Pd·min) from the first four data points in Figure 6.12(b). Importantly, this observed catalytic activity (normalized by Pd amount) is ~6 folds higher than the commercial Pd/C catalyst (Chapter 3) likely due to pristine, small, uniform, well-dispersed and highly crystalline Pd nanoparticles. The apparent rate constants in the linear region (<0.141 µg Pd/µl microparticles) indicate that: (1) all the Pd nanoparticles embedded in the PEG hydrogel network structure are accessible to the reactants for the reaction, (2) the Pd-TMV-PEG microparticles containing uniform and well-dispersed 1-2 nm Pd nanoparticles have good catalytic activity, (3) there appears to be no apparent internal diffusion limitation from these particles containing different Pd-TMV complex amounts, and (4) The PEG porous hydrogel network structure provides a good matrix for the encapsulation of catalytically active Pd nanoparticles while allowing sufficient mass transfer of the small molecule reactants and products under the fabrication conditions enlisted.

When the Pd loading densities in the microparticles are above 0.282 µg Pd/µl microparticles, the apparent rate constants k_{app} start becoming lower than the expected ideal rate constants (the dash line). This indicates that not all the Pd nanoparticles in the hydrogel microparticles are utilized in the catalytic reaction. One explanation is that certain degree of internal diffusion limitation occurs in the

higher Pd-TMV loading density cases. According to the molecular dynamics (MD) simulations by Wu et al.²⁴⁸ and the Amsden theory²⁴⁹, the diffusion coefficient D_{eff} of ions through PEG700 ($n=16$) hydrogel is about $0.5 \times 10^{-5} \text{ cm}^2/\text{s}$. Thus, the estimation of Weisz modulus (M_w) of the Pd-TMV-PEG microparticles with Pd loading density of 0.282 and 0.564 $\mu\text{g Pd}/\mu\text{l}$ microparticles are about 0.26 and 0.35, respectively. These values of the Weisz modulus are within the range of slight diffusion limitation¹⁶. The presence of Pd-TMV complex in crosslinked PEG hydrogel network structure may change the dynamic properties of the hydrogels (such as average mesh size or overall hydrogel structure), thus small degree of internal diffusion limitation may occur for the Pd-TMV-PEG microparticles with higher Pd loading densities. With robust replica molding technique reported here, these results indicate that the catalyst loading density in hydrogel microparticles can be readily controlled to be in the optimal ranges within the kinetic controlled region simply by changing the loading density of the Pd-TMV complexes in the preparticle solution.

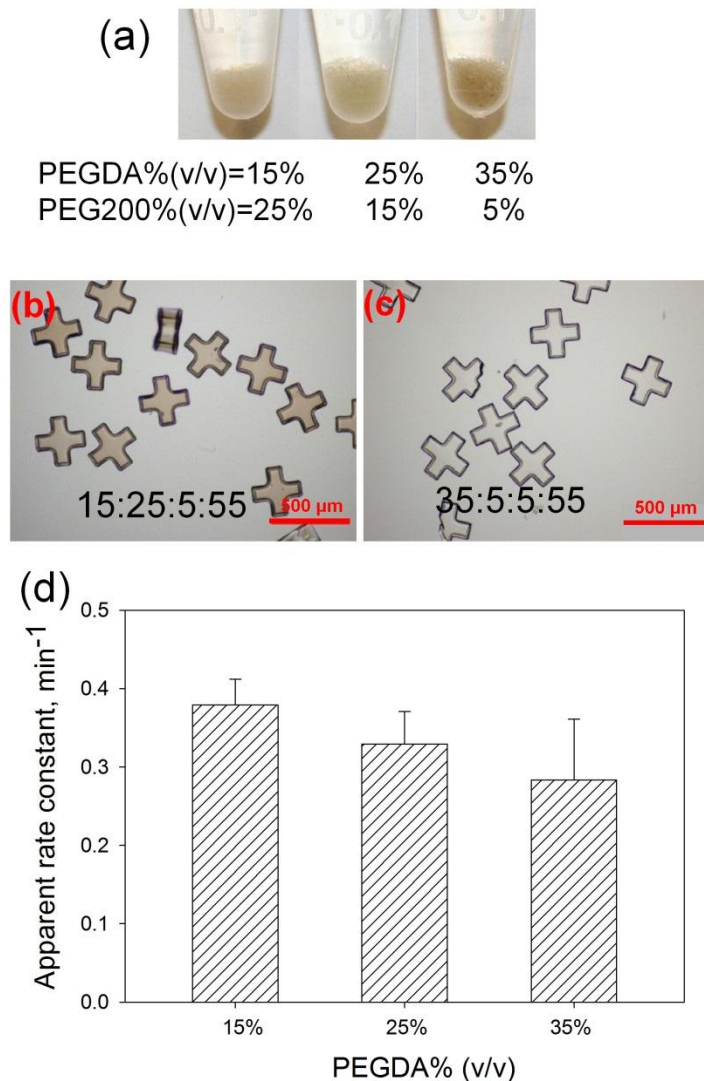


Figure 6.13. Effect of PEGDA% (v/v) on the Microparticle Fabrication

(a) Photographs of Pd-TMV-PEGDA microparticles fabricated with different PEGDA% in preparticle composition. 0.6 mg/ml Pd-TMV. The micrographs of microparticles made with preparticle solution composition PEGDA: PEG200: PI: Pd-TMV(v/v/v/v)=(b) 15:25:5:55 and (c) 35:5:5:55. (d) The apparent rate constant of dichromate reduction catalyzed by various PEGDA% (v/v).

In addition, the catalytic activity studies in Figure 6.13 show that microparticles fabricated with decreasing concentration of PEGDA in the preparticle composition exhibit higher apparent rate constant for dichromate reduction. Engberg et al.^{250 251} found that decreasing the initial PEGDA% acts to increase the spacing of crosslink junctions and to form polymer networks with looser structures. Similarly, the usage of PEG prepolymers with higher molecular weight could lead to larger hydrogel mesh size, resulting in higher diffusion coefficient and thus less internal diffusion limitation of reactants through the hydrogel matrix²⁴⁸.

Combined results in Figure 6.11 demonstrate high catalytic activity of the PEG hydrogel microparticles encapsulating Pd-TMV nanostructures. Furthermore, the reaction rate catalyzed by Pd-TMV-PEG microparticles is linearly proportional to the Pd loading density inside hydrogels within the diffusion limitation-free region. Next, the porous network structure of the PEG hydrogels with 2-3 nm mesh size²⁴² enables sufficient diffusion of small reactant molecules through the matrix. Last, Pd-TMV-PEG hydrogel microparticles as catalysts allow for simple separation from the reaction solution by low-speed centrifugation under mild conditions. Therefore, the simple replica molding for fabrication of PEG hydrogel microparticles to encapsulate Pd-TMV complex as catalysts presents a

robust strategy that could be readily extended to other hybrid nanostructures or functionalities.

6.7. Recyclability and Stability of Pd-TMV-PEG Microparticles

In order to further examine the stability of the Pd-TMV-PEG microparticles, I next carried out five reaction cycles catalyzed by microparticles (total volume=10.4 μl) containing 0.071 μg Pd/ μl microparticles without any regeneration treatments as shown in Figure 6.14. The conversion of the dichromate reached near-completion for all the five runs (Figure 6.14(a)) with the apparent rate constants being 0.75, 0.77, 0.72, 0.69, and 0.60 min^{-1} , respectively. Considering loss of certain number of microparticles at each recycling (i.e. removal of reaction mixtures), the 20% decrease in the rate constant after 5 reaction cycles indicates stability and recyclability of these hydrogel microparticles. Furthermore, the photomicrographs of the microparticles upon 5 cycle reactions in Figure 6.14(b) clearly show that the shape, structure and size remain identical to the before-reaction state. Overall, the results in Figure 6.14(a) and (b) show that the Pd-TMV nanostructures remain entrapped in the cross-linked PEG hydrogel network structure through catalytic reaction conditions in a stable manner. Notably, the good stability and recyclability of as-prepared Pd-TMV-PEG hydrogel microparticles as catalysts are mainly due to the relative dimensions of Pd nanoparticles (1-2nm) vs. Pd-TMV complexes/network (up to

micrometers) vs. hydrogel mesh size (2-3 nm) vs. small molecule reactants and products (angstroms). On one hand, the integration of 1-2 nm Pd nanoparticles with TMV nanostructures (in length of 300 nm) allows Pd nanoparticles to stay well-dispersed and entrapped inside the hydrogel networks through catalytic reaction conditions. On the other hand, the 2-3 nm mesh size of hydrogel allows the minimal mass transfer limitation of small molecule reactants and products (a few angstroms hydrodynamic radius) through microparticles with 50 μm characteristic length examined in this study. Hence, the presence of TMV helps stabilize and disperse small Pd nanoparticles within the PEG hydrogel network structure. Furthermore, the microparticle size and mesh size can be readily controlled and manipulated for optimal payload of Pd nanoparticles and catalytic performance.

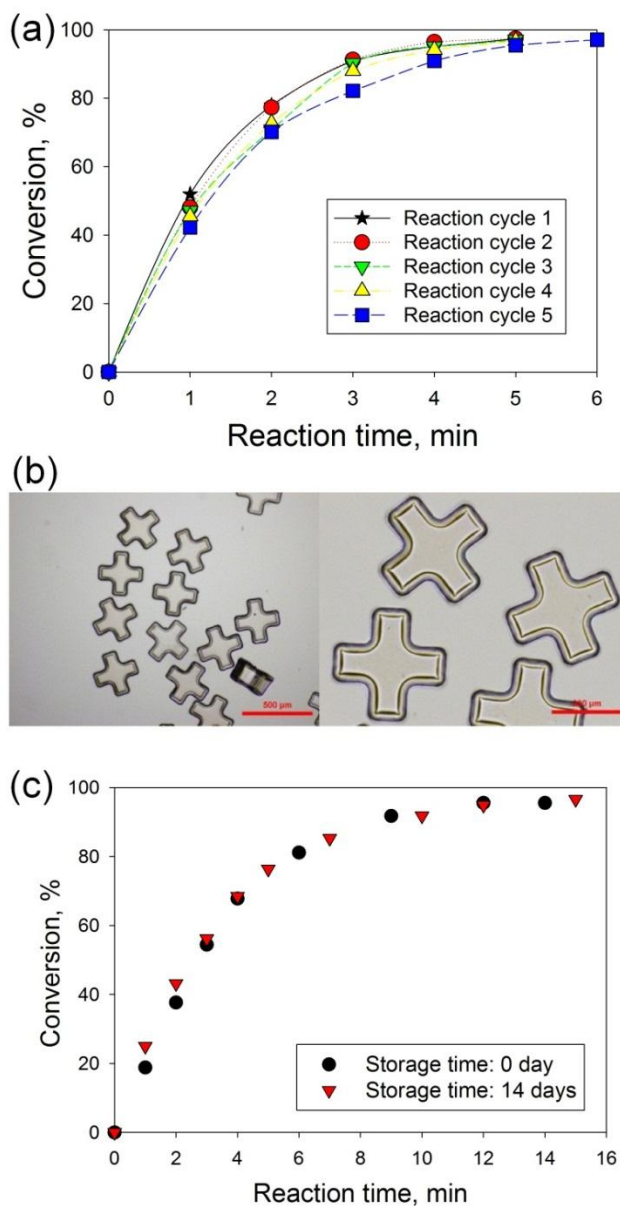


Figure 6.14. Stability Study of Pd-TMV-PEGDA Microparticles as Catalysts for Dichromate Reduction

(a) Recycling study (b) Microphotographs of microparticles after 5 cycles of dichromate reduction. (c) Stability upon 14 days storage

Finally, I further examined the catalytic activity of the Pd-TMV-PEG microparticles upon long term storage, as shown in Figure 6.14(c). The conversion rate upon 14-day storage (triangle symbols) at room temperature was identical to the one from freshly prepared samples (circle symbols). This result clearly indicates that the Pd-TMV-PEG microparticles are stable under ambient conditions, and that the PEG hydrogel network provides stable matrix for the Pd-TMV nano-bio complexes without any leaching over extended storage. Combined, results shown in Figure 6.14 demonstrate that this novel hybrid catalysts embedded in the polymeric hydrogel format possess stability upon catalytic reaction conditions and long term storage.

6.8. Conclusions

In this Chapter, I thoroughly examined a facile synthesis-fabrication procedure to create a novel nano-bio complexes with small and catalytically active Pd nanoparticles seamlessly integrated in robust polymeric hydrogel microparticle formats. First, UV-Vis absorbance observations showed rapid formation of Pd-TMV complexes that can be readily separated and processed. Further, TEM characterization confirmed the spontaneous and exclusive formation of small (1-2 nm), uniform and highly crystalline Pd(111) nanoparticles along TMV

biotemplates. Both concentration and ratio between Na₂PdCl₄ and TMV were found to be important factors for the formation of uniform and well-dispersed Pd-TMV complexes. Second, we presented a simple and highly reproducible fabrication procedure for the integration of Pd-TMV complexes into uniform PEG-based polymeric microparticles via replica molding technique. Third, this novel nano-bio-polymeric hybrid material was demonstrated to possess readily controllable Pd loading density, high catalytic activity and good stability for dichromate reduction. Combined these results not only indicate facile routes to harness the unique advantages of biotemplates for the controlled synthesis of functional nanomaterials, but also suggest robust fabrication strategies to integrate additional functionalities in a stable, robust and highly reproducible formats. I expect that this novel synthesis-fabrication procedure can be readily extended into the fabrication of other nano-bio-polymeric hybrid materials with multifunctionalities based on various metal nanoparticles or polymer formats for catalysis or energy application.

7. Conclusions and Future Prospects

In chapter 2, I described a novel bottom-up assembly synthesis approach for the fabrication of viral-templated Pd nanocatalyst, and examined the catalytic activity, recyclability and stability for dichromate reduction. Here, gold-coated silica chips were utilized for the TMV surface assembly. Considering the economic efficiency, other inorganic materials can be employed as alternatives. For example, Qian Wang's group demonstrated the dynamic self-assembly of TMV on piranha washed glass slides via controlled evaporation¹⁵¹. Meanwhile, although TMV is remarkably stable in a wide range of conditions including high temperature (up to 90 °C), broad pH values (2~10) and even in non-aqueous solvents, the application of TMV-templated Pd nanocatalyst for other reactions with harsher conditions beyond TMV's bearable scope is still a challenge. Therefore, further stabilization of Pd-TMV complex structure without damaging the chemical properties of Pd nanoparticles will be the next step. One potential solution is to further coating Pd-TMV-gold chip surface with thin layers of mesoporous silica by sol-gel process, followed by calcination to further increase the mechanical and thermal stability. In addition, this facile strategy for nanostructured Pd catalyst synthesis based on surface-assembled viral templates could be readily extended to the synthesis of other metal nanocatalysts, such as platinum or gold, which can be applied for other catalytic reaction systems.

In chapter 3, the synthesis-structure-activity relationship of Pd-TMV chip catalysts for dichromate reduction was thoroughly examined, and it was found that Pd catalyzed dichromate reduction with formic acid shows size-dependent behavior, where larger Pd particles with more (111) planes would be more active for the formic acid oxidation. However, considering both catalytic activity and economic efficiency, Pd nanoparticles with small size and high catalytic activity is highly demanded. In chapter 6, the Pd nanoparticles formed by slow nucleation without additional reducing agents show both small size and high catalytic activity (per surface area). In future studies, further examination of the metal crystal structure, and chemical state changes of Pd nanoparticles are required to better understand the catalytic behavior.

In chapter 4, I presented two simple routes to modulate the nanostructured Pd catalyst loading for dichromate reduction by taking advantages of TMV's tunable and selective surface assembly on gold surfaces. In this study, I employed gold-patterned chips with millimeter dimensions fabricated via standard photolithography. The patterned assembly of biotemplates at sub-micrometer scale can be readily achieved by a wide variety of simple and economically viable patterning techniques, including soft-lithography of self-assembled monolayers (SAM)^{106,214}, direct printing techniques¹⁷⁹, inkjet printing²¹⁵⁻²¹⁷ and

nanolithographic techniques^{218,219} on practically any kind of surfaces as common and cost-efficient as glass slides.

In chapter 6, I presented the spontaneous formation of 1-2 nm Pd nanoparticles along TMV templates without adding reducing agent and the successful encapsulation of Pd-TMV complex inside PEG hydrogel microparticles fabricated by replica molding technique. Although Pd-TMV-PEG hydrogel microparticles show promising result of high catalytic activity, it is also important to consider the stability of the PEG-based microparticles with regard to the desired application. PEG is known for its hydrophilic, biocompatible, and non-fouling properties. These properties are beneficial for biosensing applications, yet PEG hydrogel may not be perfectly suitable for harsh chemical reactions with extreme temperature or pressure conditions. Therefore, alternative monomers or prepolymers that are known to withstand harsh environmental conditions can be examined as the stabilizer to encapsulate these highly active Pd-TMV bio-nano hybrid materials. Meanwhile, replica molding technique enables simple, robust and shape-controllable fabrication of microparticles containing readily exploitable Pd nanoparticles in a 3D format. In the future, the fabrication technique of Janus multifunctional particles containing both Pd-TMV catalysts and magnetic nanoparticles could be further explored. For making consistent, uniform Janus microparticles by RM technique, many different factors, including UV exposure

time, UV source intensity, the preparticle composition and the molecular weight of PEGDA prepolymer, should be carefully controlled and examined. Furthermore, instead of applying hydrogel microparticle encapsulation technique, sol-gel synthesis could be another way for the further stabilization of highly catalytically active nano-bio hybrid nanostructure to synthesize supported nanocatalysts. For example, the Pd-TMV complex could be further encapsulated inside either porous organic gel (such as carbon gels by polycondensation of hydroxylated benzene and aldehyde) or inorganic gel (such as SiO_2 , Al_2O_3 xerogel or aerogel). In this synthesis approach, TMV acts as biotemplates for the synthesis of uniform and well-dispersed Pd nanoparticles, while the organic or inorganic gels act as the highly porous supporting matrix. Since high porosity is a key property for an efficient heterogeneous catalyst, it is crucial to maintain such porosity as high as possible in the dried gel. Thus, the drying of wet gel will be a very important follow-up process step. In order to eliminate the liquid-vapor interface and the accompanying capillary pressure, supercritical drying and free crying are two powerful methods to keep the porous structure. I expect that the combination of both viral and porous polymeric materials would lead to the desired properties of novel catalysts, including high activity, high selectivity, chemical, thermal and mechanical stability, and rapid mass and heat transfers.

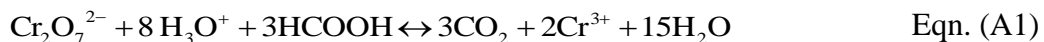
APPENDIX

A1. Derivation of Kinetics Model

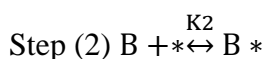
As mentioned in Section 3.2.7 and 3.4, the reaction kinetics of dichromate reduction reaction catalyzed by Pd-TMV chip catalysts are studied.

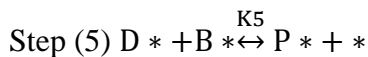
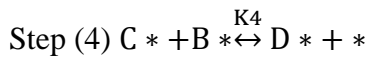
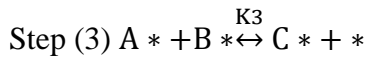
Different model equations are derived and the experimental data were fitted to the model equations to understand the reaction kinetics.

The overall reaction equation is shown below.



If the adsorption of both reactants exists, reaction rate expressions can be derived based on different rate determining step assumptions. For this, the elementary steps are written as below. $[\text{Cr}_2\text{O}_7^{2-}]$ is represented by [A], $[\text{COOH}^-]$ is represented by [B], $[\text{C}^*]$ and $[\text{D}^*]$ represent the reaction intermediates, and [P] represents the product (Cr(III) ion)





A1.1. Step (1) is the Rate Determining Step (RDS)

In this assumption, step (1) is the rate determining step (RDS), and the other steps are in equilibrium.

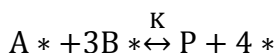
The overall reaction rate

$$r = k_1[\text{A}][*]$$

The adsorption of B on the Pd surface is in equilibrium

$$K_2 = \frac{[\text{B} *]}{[\text{B}][*]}$$

Because all other surface reaction steps (step (3)-(6)) are in equilibrium, they can be combined, as shown below.



$$K = \frac{[P][*]^4}{[A *][B *]^3}$$

Since step (1) is assumed to be the RDS, the rate of A* production is relatively slow compared to other steps. As a result, once A* is produced, it will be consumed rapidly in the following steps. Therefore, there is minimal amount of A* remaining on the catalyst surface. Instead, [B*] is the most abundant reaction intermediate (MARI).

The overall active sites [*]₀ are shown below.

$$[*]_0 = [*] + [B *]$$

$$= [*] + K_2[B][*]$$

$$[*] = \frac{[*]_0}{1 + K_2[B]}$$

$$r = k_1[*]_0 \frac{[A]}{1 + K_2[B]} \quad \text{Eqn. (A2)}$$

If the reaction kinetics follows this mechanism, r should be always proportional to [A] at any concentration of [B]. However, the experimental data in Figure 3.2(b) don't follow this mechanism.

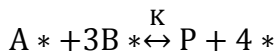
A1.2. Step (2) is the Rate Determining Step (RDS)

In this assumption, step (2) is the rate determining step (RDS), the overall reaction rate

$$r = k_2[B][*]$$

$$K_1 = \frac{[A^*]}{[A][*]}$$

Because all other equations are in equilibrium, step (3)-(6) can be combined, as shown below.



$$K = \frac{[P][*]^4}{[A^*][B^*]^3}$$

Similar to 2.1, $[B^*]$ is negligible, and $[A^*]$ is the MARI.

$$[*]_0 = [*] + [A^*] \quad ([B^*] \text{ is not included in this } [*]_0)$$

$$= [*] + K_1[A][*]$$

$$[*] = \frac{[*]_0}{1 + K_1[A]}$$

$$r = k_2[*]_0 \frac{[B]}{1+K_1[A]} \quad \text{Eqn. (A3)}$$

r should be proportional to $[B]$ at any concentration of $[A]$, but the experimental data shown in Figure 3.2(a) don't follow this mechanism.

A1.3. Step (3) is the Rate Determining Step (RDS)

In addition to the derivation described in Section 3.2.7, another derivation of overall rate expression including the reverse reaction rate r_{-3} is carried out based on the pseudo-steady-state hypothesis in this section, as shown below.

Since reaction step 3 is the rate determining step,

The overall reaction rate r is equal to the rate of elementary reaction step 3:

$$r = r_3 = k_3[A^*][B^*] - k_{-3}[C^*][*] \quad \text{Eqn. (A4)}$$

Assume C^* is a short-lived intermediate and apply the pseudo-steady-state hypothesis:

$$\begin{aligned} \frac{d[C^*]}{dt} &= r_3 - r_4 = k_3[A^*][B^*] - k_{-3}[C^*][*] - k_4[C^*][B^*] + k_{-4}[D^*][*] \\ &= 0 \end{aligned}$$

$$\text{So } [C^*] = \frac{k_3[A^*][B^*] + k_{-4}[D^*][*]}{k_{-3}[*] + k_4[B^*]}$$

Assume elementary reaction steps 1, 2, 5, 6 are fast and therefore instantaneously in equilibrium:

$$[A^*] = K_1[A][*]$$

$$[B^*] = K_2[B][*]$$

$$K_5[B^*][D^*] = [P^*]^2$$

$$[P^*]K_6 = [P][*]$$

$$\text{So } [P^*] = \frac{[P][*]}{K_6}$$

$$K_5[B^*][D^*] = K_5K_2[B][*][D^*] = \left(\frac{[P][*]}{K_6}\right)^2$$

$$\text{So } [D^*] = \frac{[P]^2[*]}{K_6^2 K_5 K_2[B]}$$

$$[C^*] = \frac{k_3 K_1[A][*] K_2[B][*] + k_{-4} \frac{[P]^2[*]}{K_6^2 K_5 K_2[B]} [*]}{k_{-3}[*] + k_4 K_2[B][*]}$$

$$= \frac{(k_3 K_1[A] K_2[B] + \frac{k_{-4}[P]^2}{K_6^2 K_5 K_2[B]})[*]}{k_{-3} + k_4 K_2[B]}$$

$$[*]_0 = [*] + [A^*] + [B^*] + [C^*] + [D^*] + [P^*]$$

$$= [*] + K_1[A][*] + K_2[B][*] + \frac{(k_3K_1[A]K_2[B] + \frac{k_{-4}[P]^2}{K_6^2K_5K_2[B]})[*]}{k_{-3} + k_4K_2[B]} \\ + \frac{[P]^2[*]}{K_6^2K_5K_2[B]} + \frac{[P][*]}{K_6}$$

$$\text{So } [*] = \frac{[*]_0}{1 + K_1[A] + K_2[B] + \frac{k_3K_1K_2[A][B] + \frac{k_{-4}[P]^2}{K_6^2K_5K_2[B]}}{k_{-3} + k_4K_2[B]} + \frac{[P]^2}{K_6^2K_5K_2[B]} + \frac{[P]}{K_6}}$$
Eqn. (A5)

In the initial reaction stage, the concentration of product P is nearly zero, i.e.

$$[P] \approx 0$$

Therefore, Eqn. (A5) can be simplified into

$$[*] = \frac{[*]_0}{1 + K_1[A] + K_2[B] + \frac{k_3K_1K_2[A][B]}{k_{-3} + k_4K_2[B]}}$$
Eqn. (A6)

Thus the overall reaction rate $r = r_3 = k_3[A^*][B^*] - k_{-3}[C^*][*]$

$$= (k_3K_1K_2[A][B] - \frac{k_{-3}(k_3K_1K_2[A][B] + \frac{k_{-4}[P]^2}{K_6^2K_5K_2[B]})}{k_{-3} + k_4K_2[B]}) [*]^2$$
Eqn. (A7)

At the initial reaction stage, $[P] \approx 0$, thus Eqn. (A7) can be simplified into:

$$r = r_3 = (k_3 K_1 K_2 [A][B] - \frac{k_{-3} k_3 K_1 K_2 [A][B]}{k_{-3} + k_4 K_2[B]})(\frac{[*]_0}{1 + K_1[A] + K_2[B] + \frac{k_3 K_1 K_2 [A][B]}{k_{-3} + k_4 K_2[B]}})^2$$

$$= (\frac{k_3 k_4 K_1 K_2 [A][B]^2}{k_{-3} + k_4 K_2[B]})(\frac{[*]_0}{1 + K_1[A] + K_2[B] + \frac{k_3 K_1 K_2 [A][B]}{k_{-3} + k_4 K_2[B]}})^2 \quad \text{Eqn. (A8)}$$

If $k_4 K_2[B] \gg k_{-3}$, Eqn. (A8) can be simplified into:

$$r = \frac{k_3 K_1 K_2 [*]_0^2 [A][B]}{[1 + K_1(1 + \frac{k_3}{k_4})[A] + K_2[B]]^2} = \frac{P1[A][B]}{(1 + P3[A] + P2[B])^2} \quad \text{Eqn. (A9)}$$

$$(P1 = k_3 K_1 K_2 [*]_0^2; P2 = K_2; P3 = K_1(1 + \frac{k_3}{k_4}))$$

Apparently, based on the assumption that the reversible reaction step 3 is negligible, the obtained rate expression in Equation (A9) is similar to the expression of Equation (3.6). As shown in Figure A1, the point symbols represent the experimental data, while the solid lines were derived based on using Equation (A9) and three unknown parameters (P1, P2 and P3) fit to the experimental data by Matlab and Polymath software. As shown in Table A1, obtained values of P1, P2 and P3 are 5600 L/(mol min), 1474.7 L/mol and 5.6 L/mol, respectively. The R^2 value of the overall fitting is as high as 0.975, which indicates a suitable model fitting compared to the fittings to other model equation.

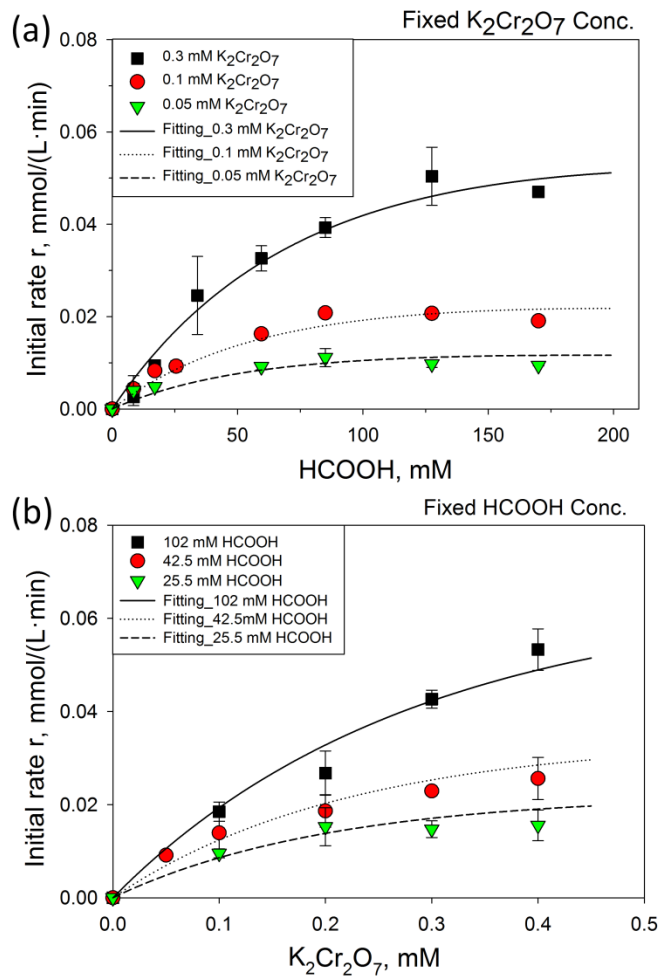


Figure A1. The Model Fitting of Dichromate Reduction.

(a). Dependence of the initial reaction rate r_0 on the initial concentration of NaCOOH with fixed $K_2Cr_2O_7$ concentration. (b) Dependence of the r_0 on the initial concentration of $K_2Cr_2O_7$ with fixed NaCOOH concentration. The catalyst synthesis condition: 0.25 mM Na_2PdCl_4 , 15 mM $NaPH_2O_2$, 20min metallization.

Table A1. Value of Three Parameters Obtained from Data Fitting

Variable	Value	95% confidence
P1	5600 L/(mol min)	6.17E-8
P2	1474.7 L/mol	3.69E-5
P3	5.6 L/mol	1.07E-7

A1.4. Step (4) is the Rate Determining Step (RDS)

In this assumption, step (4) is the rate determining step (RDS), Step (1), (2) and (3) are in equilibrium, so

$$K_1 = \frac{[A^*]}{[A][*]}$$

$$K_2 = \frac{[B^*]}{[B][*]}$$

$$K_3 = \frac{[C^*][*]}{[A^*][B^*]}$$

$$[C^*] = \frac{K_3[A^*][B^*]}{[*]} = [*]K_3 K_1 K_2 [A][B]$$

Combine step (5) and (6)



$$K = \frac{[P][*]^2}{[D *][B *]}$$

The overall active sites includes $[A^*]$, $[B^*]$ and $[C^*]$

$$[*]_0 = [*] + [A *] + [B *] + [C *]$$

$$= [*] + K_1[A][*] + K_2[B][*] + K_1K_2K_3[A][B][*]$$

$$[*] = \frac{[*]_0}{1 + K_1[A] + K_2[B] + K_1K_2K_3[A][B]}$$

$$r = k_4[C *][B *]$$

$$= k_4K_3 K_1K_2^2[A][B]^2[*]^2$$

$$r = k_4[*]_0^2 K_3 \frac{K_1[A]K_2^2[B]^2}{(1+K_1[A]+K_2[B]+K_1K_2K_3[A][B])^2} \quad \text{Eqn. (A10)}$$

From the data fitting, negative values for K_2 are obtained, which is unreasonable.

So this mechanism is not suitable.

Variable	Initial guess	Value	95% confidence
k	0.01	0.1051534	2.887E-05
K3	1.	10.13411	0.0036841

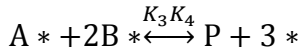
K1	1.	10.6792	0.0038826
K2	1.	-99.9295	127.8908

A1.5. Step (5) is the Rate Determining Step (RDS)

In this assumption, step (5) is the rate determining step (RDS), Step (1), (2), (3) and (4) are in equilibrium, so

$$r = k_5[D^*][B^*]$$

Combine (3) and (4)



$$\begin{aligned} [^*]_0 &= [*] + [A^*] + [B^*] + [C^*] + [D^*] \\ &= [*] + K_1[A][*] + K_2[B][*] + K_1 K_2 K_3[A][B][*] + K_1 K_2^2 K_3 K_4[A][B]^2[*] \end{aligned}$$

$$[*] = \frac{[^*]_0}{1 + K_1[A] + K_2[B] + K_1 K_2 K_3[A][B] + K_1 K_2^2 K_3 K_4[A][B]^2}$$

$$\text{So } r = k_5 K_2[B][*] \cdot K_3 K_4[A] K_1 K_2^2[B]^2[*]$$

$$= k_5 K_1 K_2^3 K_3 K_4[A][B]^3[*]^2$$

$$r = \frac{k_5 K_1 K_2^3 K_3 K_4 [A][B]^3 [*]_0^2}{(1+K_1[A]+K_2[B]+K_1 K_2 K_3[A][B]+K_1 K_2^2 K_3 K_4[A][B]^2)^2} \quad \text{Eqn. (A11)}$$

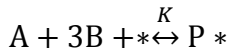
From the data fitting, negative values of parameters are obtained, as shown in the table below. Therefore, this mechanism is not suitable.

Variable	Initial guess	Value	95% confidence
k	0.01	0.2604758	0.0641907
K3	1.	-0.0212692	0.0406235
K4	1.	-0.8479221	1.580888
K1	1.	-2.374186	1.485264
K2	1.	-0.1864654	0.0878847

NOTE: Calculations exceeded the maximum number of iterations.

A1.6. Step (6) is the Rate Determining Step (RDS)

In this assumption, step (6) is the rate determining step (RDS), Step (1), (2), (3), (4) and (5) are in equilibrium, so step (1)-(5) can be combined, as shown below.



$$[P *] = K[A][B]^3[*]$$

In this case, $[P^*]$ is the MARI,

$$[*]_0 = [*] + [P^*]$$
$$[*] = \frac{[*]_0}{1 + K[A][B]^3}$$

The overall reaction rate

$$r = k_6[P^*]$$

$$= k_6[*]_0 \frac{K[A][B]^3}{1+K[A][B]^3} \quad \text{Eqn. (A12)}$$

The data fitting by using polymath shows the error below.

NOTE: Calculations exceeded the maximum number of iterations.

A2. The Calibration Curve of Potassium Dichromate

As shown in Figure A2, the concentration of $K_2Cr_2O_7$ is linearly related to characteristic absorbance of Cr(VI) ion at 350 nm wavelength. The R^2 value is as high as 0.9995. The correlation between the absorbance at 350nm and the concentration of $K_2Cr_2O_7$ is show as $A_{350\text{ nm}}=0.01 \times [K_2Cr_2O_7] + 0.001$.

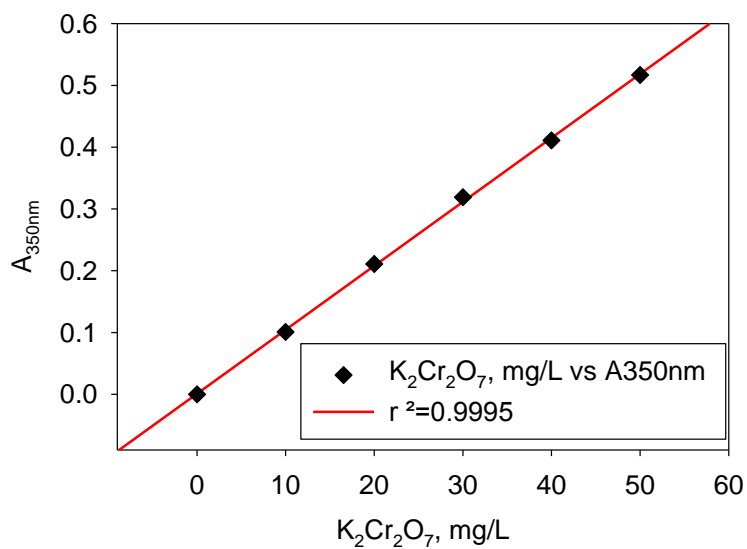


Figure A2. Calibration Curve of Potassium Dichromate Concentration Demination

A3. The Effect of Stirring Speed on the Dichromate Reduction Rate

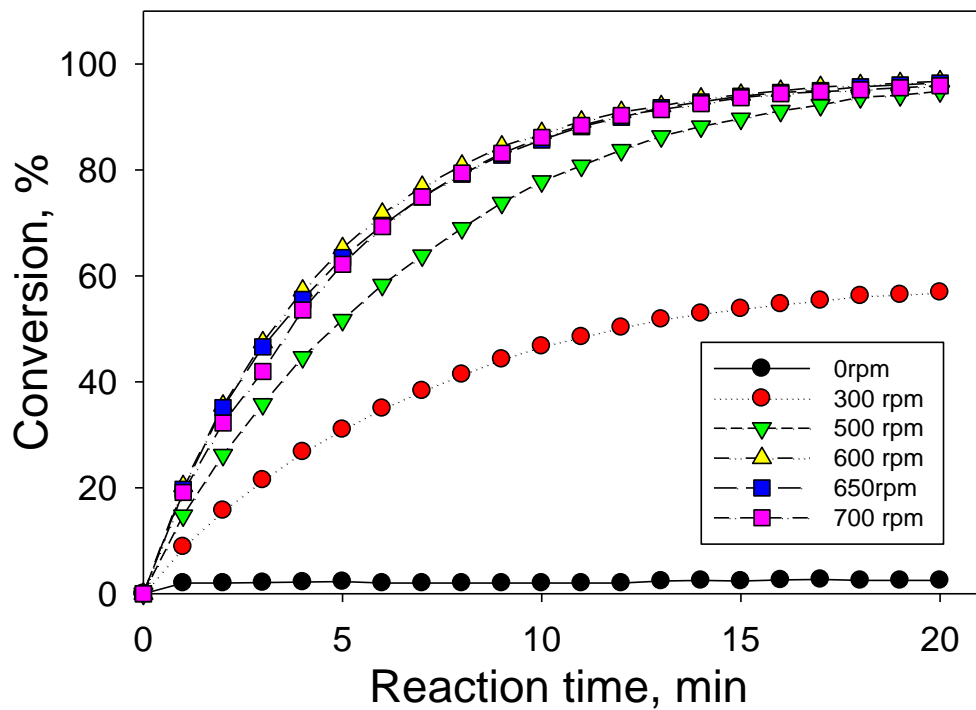


Figure A3. Effect of Stirring Speed on the Reaction Rate

As shown in Figure A3, dichromate reductions were carried out with different stirring speed (0 rpm, 300, 500, 600, 650 and 700 rpm) and the conversion rates were compared with each other. Clearly, the conversion rate increases with the increase of stirring speed in the range of 0-600 rpm. When the stirring speeds are

higher than 600 rpm, the conversion rates remain the same as that of 600 rpm. This result indicates that the possible external diffusion limitation can be eliminated at the condition of stirring speed higher than 600 rpm. Therefore, the stirring speed applied for the dichromate reduction throughout this thesis is 600 rpm.

References

- (1) Toebes, M. L.; van Dillen, J. A.; de Jong, K. P. *J. Mol. Catal. A: Chem.* **2001**, *173*, 75.
- (2) B. M. Bhanage, M. A. *Cat. Rev. - Sci. Eng.* **2001** *43*, 315.
- (3) Harm P. Dijkstra, G. P. M. v. K., Gerard van Koten. *Acc. Chem. Res.* **2002**, *35*, 798.
- (4) Miyaura, N.; Suzuki, A. *Chem. Rev.* **1995**, *95*, 2457.
- (5) Kim, S.-W.; Kim, M.; Lee, W. Y.; Hyeon, T. *J. Am. Chem. Soc.* **2002**, *124*, 7642.
- (6) Felpin, F. X.; Ayad, T.; Mitra, S. *Eur. J. Org. Chem.* **2006**, 2679.
- (7) Jiang, J.-Z.; Cai, C. *J. Dispersion Sci. Technol.* **2008**, *29*, 453
- (8) Carrettin, S.; McMorn, P.; Johnston, P.; Griffin, K.; Kiely, C. J.; Hutchings, G. J. *PCCP* **2003**, *5*, 1329.
- (9) Dimitratos, N.; Lopez-Sanchez, J.; Lennon, D.; Porta, F.; Prati, L.; Villa, A. *Catal. Lett.* **2006**, *108*, 147.
- (10) Omole, M. A.; K'Owino, I. O.; Sadik, O. A. *Appl. Catal., B* **2007**, *76*, 158.
- (11) K'Owino, I. O.; Omole, M. A.; Sadik, O. A. *J. Environ. Monitor.* **2007**, *9*, 657.
- (12) Michael O. Nutt, J. B. H., Michael S. Wong. *Environ. Sci. Technol.* **2005**, *39*, 1346.
- (13) Li, S.; Fang, Y.-L.; Romanczuk, C. D.; Jin, Z.; Li, T.; Wong, M. S. *Appl. Catal., B* **2012**, *125*, 95.
- (14) Fang, Y.-L.; Heck, K. N.; Alvarez, P. J. J.; Wong, M. S. *ACS Catalysis* **2011**, *1*, 128.

- (15) Regalbuto, J. *Catalyst preparation: science and engineering*; CRC Press, 2006.
- (16) Levenspiel, O. *The Chemical Reactor Omnibook*; Oregon St Univ Bookstores, 2002.
- (17) Astruc, D.; Lu, F.; Aranzaes, J. R. *Angew. Chem. Int. Ed.* **2005**, *44*, 7852.
- (18) Drelinkiewicza, A.; Waksmundzka, A.; Makowski, W.; Sobczak, J. W.; Król, A.; Zieba, A. *Catal. Lett.* **2004**, *94*, 143.
- (19) Crooks, R. M.; Zhao, M.; Sun, L.; Chechik, V.; Yeung, L. K. *Acc. Chem. Res.* **2001**, *34*, 181.
- (20) Nobre, S. M.; Monteiro, A. L. *J. Mol. Catal. A: Chem.* **2009**, *313*, 65.
- (21) Ramirez, E.; Jansat, S.; Philippot, K.; Lecante, P.; Gomez, M.; Masdeu-Bultó, A. M.; Chaudret, B. *J. Organomet. Chem.* **2004**, *689*, 4601.
- (22) Bhattacharya, S.; Srivastava, A.; Sengupta, S. *Tetrahedron Lett.* **2005**, *46*, 3557.
- (23) Paetzold, E.; Oehme, G. *J. Mol. Catal. A: Chem.* **2000**, *152*, 69.
- (24) Polshettiwar, V.; Len, C.; Fihri, A. *Coord. Chem. Rev.* **2009**, *253*, 2599.
- (25) Haack, L. P.; Otto, K. *Catal. Lett.* **1995**, *34*, 31.
- (26) Chen, H.; Shao, Y.; Xu, Z.; Wan, H.; Wan, Y.; Zheng, S.; Zhu, D. *Appl. Catal., B* **2011**, *105*, 255.
- (27) Sekizawa, K.; Widjaja, H.; Maeda, S.; Ozawa, Y.; Eguchi, K. *Catal. Today* **2000**, *59*, 69.
- (28) Zhang, Y.; Xiang, Q.; Xu, J.; Xu, P.; Pan, Q.; Li, F. *J. Mater. Chem.* **2009**, *19*, 4701.
- (29) Martinez, S.; Moreno-Manas, M.; Vallribera, A.; Schubert, U.; Roig, A.; Molins, E. *New J. Chem.* **2006**, *30*, 1093.

- (30) Pope, E. J. A.; Mackenzie, J. D. *J. Non-Cryst. Solids* **1986**, *87*, 185.
- (31) Das, D. D.; Sayari, A. *J. Catal.* **2007**, *246*, 60.
- (32) Koby, M. *Bioresource Technol.* **2004**, *91*, 317.
- (33) Chen, X.; Hou, Y.; Wang, H.; Cao, Y.; He, J. *J. Phys. Chem. C* **2008**, *112*, 8172.
- (34) Tessonniere, J.-P.; Pesant, L.; Ehret, G.; Ledoux, M. J.; Pham-Huu, C. *Appl. Catal., A* **2005**, *288*, 203.
- (35) Milić, N. B.; Bugarčić, Ž. D. *Transition Met. Chem.* **1984**, *9*, 173.
- (36) Agostini, G.; Groppo, E.; Piovano, A.; Pellegrini, R.; Leofanti, G.; Lamberti, C. *Langmuir* **2010**, *26*, 11204.
- (37) Harada, T.; Ikeda, S.; Miyazaki, M.; Sakata, T.; Mori, H.; Matsumura, M. *J. Mol. Catal. A: Chem.* **2007**, *268*, 59.
- (38) Klasovsky, F.; Claus, P.; Wolf, D. *Top. Catal.* **2009**, *52*, 412.
- (39) Elding, L. I. *Inorg. Chim. Acta* **1972**, *6*, 647.
- (40) Drew Tait, C.; Janecky, D. R.; Rogers, P. S. Z. *Geochim. Cosmochim. Acta* **1991**, *55*, 1253.
- (41) Djokic, S. S. *Plat. Surf. Finish.* **1999**, *86*, 104.
- (42) Lee, S.; Royston, E.; Culver, J. N.; Harris, M. T. *Nanotechnol.* **2005**, *16*, S435.
- (43) Nemamcha, A.; Rehspringer, J. L.; Khatmi, D. *J. Phys. Chem. B* **2006**, *110*, 383.
- (44) C.R.K. Rao, D. C. T. *Coord. Chem. Rev.* **2005**, *249*, 613.
- (45) Cho, J. K.; Najman, R.; Dean, T. W.; Ichihara, O.; Muller, C.; Bradley, M. *J. Am. Chem. Soc.* **2006**, *128*, 6276.
- (46) Pham-Huu, C.; Keller, N.; Ehret, G.; Charbonniere, L. c. J.; Ziessel, R.; Ledoux, M. J. *J. Mol. Catal. A: Chem.* **2001**, *170*, 155.

- (47) Lopez, T.; Asomoza, M.; Bosch, P.; Garcia-Figueroa, E.; Gomez, R. *J. Catal.* **1992**, *138*, 463.
- (48) Whitacre, D. M. *Reviews of environmental contamination and toxicology*; Springer-Verlag: New York, 2006; Vol. 191.
- (49) Alternatives, N. R. C. C. o. G. W. C. *Alternatives for Ground Water Cleanup*; National Academy Press: Washington DC, 1994.
- (50) J.L. Gardea-Torresdey, K. J. T., V. Armendariz, L. Bess-Oberto, R.R. Chianelli, J. Rios, J.G. Parsons, G. Gamez. *J. Hazard. Mater.* **2000**, *80*, 175.
- (51) Owlad, M.; Aroua, M.; Daud, W.; Baroutian, S. *Water, Air, Soil Pollut.* **2009**, *200*, 59.
- (52) Bagchi, D.; Stohs, S. J.; Downs, B. W.; Bagchi, M.; Preuss, H. G. *Toxicology* **2002**, *180*, 5.
- (53) Kimbrough, D. E.; Cohen, Y.; Winer, A. M.; Creelman, L.; Mabuni, C. *Crit. Rev. Env. Sci. Tech.* **1999**, *29*, 1.
- (54) Venitt, S.; Levy, L. S. *Nature* **1974**, *250*, 493.
- (55) Dakiky, M.; Khamis, M.; Manassra, A.; Mer'eb, M. *Adv. Environ. Res.* **2002**, *6*, 533.
- (56) Fiol, N.; Villaescusa, I.; Martínez, M.; Miralles, N.; Poch, J.; Serarols, J. *Environ. Chem. Lett.* **2003**, *1*, 135.
- (57) Dandapat, A.; Jana, D.; De, G. *Appl. Catal., A* **2011**, *396*, 34.
- (58) Dadong Shao, X. W., Qiaohui Fan. *Microporous Mesoporous Mater.* **2009**, *117* 243.
- (59) Sedlak, D. L.; Chan, P. G. *Geochim. Cosmochim. Acta* **1997**, *61*, 2185.
- (60) Ponder, S. M.; Darab, J. G.; Mallouk, T. E. *Environ. Sci. Technol.* **2000**, *34*, 2564.
- (61) BEUKES; #160; P., J.; PIENAAR; J., J.; LACHMANN; G.; GIESEKKE; W., E. *The reduction of hexavalent chromium by sulphite in*

wastewater; Water Research Commision: Pretoria, AFRIQUE DU SUD, 1999; Vol. 25.

- (62) Qin, G.; McGuire, M. J.; Blute, N. K.; Seidel, C.; Fong, L. *Environ. Sci. Technol.* **2005**, 39, 6321.
- (63) Deng, B.; Stone, A. T. *Environ. Sci. Technol.* **1996**, 30, 2484.
- (64) Deng, B.; Stone, A. T. *Environ. Sci. Technol.* **1996**, 30, 463.
- (65) Kim, C. S.; Lan, Y. Q.; Deng, B. L. *Geochem. J.* **2007**, 41, 397.
- (66) Rivero-Huguet, M.; Marshall, W. D. *J. Hazard. Mater.* **2009**, 169, 1081.
- (67) Huang, Y.; Ma, H.; Wang, S.; Shen, M.; Guo, R.; Cao, X.; Zhu, M.; Shi, X. *ACS Appl. Mater. Interfaces* **2012**, 4, 3054.
- (68) Phan, N. T. S.; Van Der Sluys, M.; Jones, C. W. *Adv. Synth. Catal.* **2006**, 348, 609.
- (69) Astruc, D. *Inorg. Chem.* **2007**, 46, 1884.
- (70) Tao, B.; Boykin, D. W. *J. Org. Chem.* **2004**, 69, 4330.
- (71) Barder, T. E.; Walker, S. D.; Martinelli, J. R.; Buchwald, S. L. *J. Am. Chem. Soc.* **2005**, 127, 4685.
- (72) Yi, S. S.; Lee, D. H.; Sin, E.; Lee, Y. S. *Tetrahedron Lett.* **2007**, 48, 6771.
- (73) Qiu, H.; Sarkar, S. M.; Lee, D.-H.; Jin, M.-J. *Green Chem.* **2008**, 10, 37.
- (74) Artok, L.; Bulut, H. *Tetrahedron Lett.* **2004**, 45, 3881.
- (75) Köhler, K.; Heidenreich, R. G.; Soomro, S. S.; Pröckl, S. S. *Adv. Synth. Catal.* **2008**, 350, 2930.
- (76) Tamami, B.; Farjadian, F. *J. Iran. Chem. Soc.* **2011**, 8, S77.
- (77) Aktoudianakis, E.; Chan, E.; Edward, A. R.; Jarosz, I.; Lee, V.; Mui, L.; Thatipamala, S. S.; Dicks, A. P. *J. Chem. Educ.* **2008**, 85, 555.

- (78) Durand, J.; Teuma, E.; Gómez, M. *Eur. J. Inorg. Chem.* **2008**, *2008*, 3577.
- (79) Odian, G. *Principles of Polymerization*; John Wiley & Sons, 2004.
- (80) Decker, C. *Prog. Polym. Sci.* **1996**, *21*, 593.
- (81) Kim, D.-N.; Lee, W.; Koh, W.-G. *J. Chem. Technol. Biotechnol.* **2009**, *84*, 279.
- (82) Butun, S.; Sahiner, N. *Polymer* **2011**, *52*, 4834.
- (83) Yuet, K. P.; Hwang, D. K.; Haghgoie, R.; Doyle, P. S. *Langmuir* **2009**, *26*, 4281.
- (84) Klem, M. T.; Young, M.; Douglas, T. *J. Mater. Chem.* **2008**, *18*, 3821.
- (85) Ozay, O.; Ekici, S.; Baran, Y.; Kubilay, S.; Aktas, N.; Sahiner, N. *Desalination* **2010**, *260*, 57.
- (86) Qiu, Y.; Park, K. *Adv. Drug Delivery Rev.* **2001**, *53*, 321.
- (87) Gerlach, G.; Arndt, K.-F. *Hydrogel Sensors and Actuators*, 2010; Vol. 6.
- (88) Mohan, Y. M.; Premkumar, T.; Lee, K.; Geckeler, K. E. *Macromol. Rapid Commun.* **2006**, *27*, 1346.
- (89) Léger, B.; Menuel, S.; Ponchel, A.; Hapiot, F.; Monflier, E. *Adv. Synth. Catal.* **2012**, *354*, 1269.
- (90) Sahiner, N.; Ozay, H.; Ozay, O.; Aktas, N. *Appl. Catal., A* **2010**, *385*, 201.
- (91) Lu, Y.; Spyra, P.; Mei, Y.; Ballauff, M.; Pich, A. *Macromol. Chem. Phys.* **2007**, *208*, 254.
- (92) Russell, R. J.; Pishko, M. V.; Gefrides, C. C.; McShane, M. J.; Coté, G. L. *Anal. Chem.* **1999**, *71*, 3126.

- (93) Peppas, N. A.; Keys, K. B.; Torres-Lugo, M.; Lowman, A. M. *J. Controlled Release* **1999**, *62*, 81.
- (94) Drury, J. L.; Mooney, D. J. *Biomater.* **2003**, *24*, 4337.
- (95) Campelo, J. M.; Luna, D.; Luque, R.; Marinas, J. M.; Romero, A. A. *ChemSusChem* **2009**, *2*, 18.
- (96) Hou, Z.; Theyssen, N.; Brinkmann, A.; Leitner, W. *Angew. Chem. Int. Ed.* **2005**, *117*, 1370.
- (97) Hou, Z.; Theyssen, N.; Leitner, W. *Green Chem.* **2007**, *9*, 127.
- (98) Harraz, F. A.; El-Hout, S. E.; Killal, H. M.; Ibrahim, I. A. *J. Catal.* **2012**, *286*, 184.
- (99) Huang, T. S.; Wang, Y. H.; Jiang, J. Y.; Jin, Z. L. *Chin. Chem. Lett.* **2008**, *19*, 102.
- (100) Luo, C.; Zhang, Y.; Wang, Y. *J. Mol. Catal. A: Chem.* **2005**, *229*, 7.
- (101) Lewis, C. L.; Lin, Y.; Yang, C.; Manocchi, A. K.; Yuet, K. P.; Doyle, P. S.; Yi, H. *Langmuir* **2010**, *26*, 13436.
- (102) Choi, C.-H.; Lee, J.; Yoon, K.; Tripathi, A.; Stone, H. A.; Weitz, D. A.; Lee, C.-S. *Angew. Chem. Int. Ed.* **2010**, *49*, 7748.
- (103) Zhao, X.-M.; Xia, Y.; Whitesides, G. M. *J. Mater. Chem.* **1997**, *7*, 1069.
- (104) Dhananjay, D.; Patrick, S. D. *Adv. Mater.* **2009**, *21*, 4071.
- (105) Xia, Y.; Kim, E.; Zhao, X.-M.; Rogers, J. A.; Prentiss, M.; Whitesides, G. M. *Science* **1996**, *273*, 347.
- (106) Xia, Y.; Whitesides, G. M. *Annu. Rev. Mater. Sci.* **1998**, *28*, 153.
- (107) Qin, D.; Xia, Y.; Whitesides, G. M. *Nat. Protocols* **2010**, *5*, 491.
- (108) Braun, E.; Eichen, Y.; Sivan, U.; Ben-Yoseph, G. *Nature* **1998**, *391*, 775.

- (109) S. Y. Park, A. K. L.-J., B. Lee, S. Weigand, G. C. Schatz, C. A. Mirkin. *Nature* **2008**, *451*, 553.
- (110) M. Reches, E. G. *Science* **2003**, *300*, 625.
- (111) Scheibel, T.; Parthasarathy, R.; Sawicki, G.; Lin, X.; Jaeger, H.; Lindquist, S. L. *Proc. Nat. Acad. Sci. U.S.A.* **2003**, *100*, 4527.
- (112) Fiona C. Meldrum, V. J. W., Duncan L. Nimmo, Brigid R. Heywood, Stephen Mann. *Nature* **1991**, *349*, 684.
- (113) Klaus, T.; Joerger, R.; Olsson, E.; Granqvist, C. G. *Proc. Nat. Acad. Sci. U.S.A.* **1999**, *96*, 13611.
- (114) Zhang, H.; Li, Q.; Lu, Y.; Sun, D.; Lin, X.; Deng, X.; He, N.; Zheng, S. *J. Chem. Technol. Biotechnol.* **2005**, *80*, 285.
- (115) Koudelka, K. J.; Manchester, M. *Curr. Opin. Chem. Biol.* **2010**, *14*, 810.
- (116) Lee, Y. J.; Yi, H.; Kim, W. J.; Kang, K.; Yun, D. S.; Strano, M. S.; Ceder, G.; Belcher, A. M. *Science* **2009**, *324*, 1051.
- (117) Plascencia-Villa, G.; Saniger, J. M.; Ascencio, J. A.; Palomares, L. A.; Ramírez, O. T. *Biotechnol. Bioeng.* **2009**, *104*, 871.
- (118) Steinmetz, N. F.; Shah, S. N.; Barclay, J. E.; Rallapalli, G.; Lomonossoff, G. P.; Evans, D. J. *Small* **2009**, *5*, 813.
- (119) Douglas, T.; Young, M. *Nature* **1998**, *393*, 152.
- (120) Sidhu, S. S. *Biomol. Eng.* **2001**, *18*, 57.
- (121) Whaley, S. R.; English, D. S.; Hu, E. L.; Barbara, P. F.; Belcher, A. M. *Nature* **2000**, *405*, 665.
- (122) Mao, C.; Flynn, C. E.; Hayhurst, A.; Sweeney, R.; Qi, J.; Georgiou, G.; Iverson, B.; Belcher, A. M. *Proc Natl Acad Sci U S A* **2003**, *100*, 6946.
- (123) Mao, C.; Solis, D. J.; Reiss, B. D.; Kottmann, S. T.; Sweeney, R. Y.; Hayhurst, A.; Georgiou, G.; Iverson, B.; Belcher, A. M. *Science* **2004**, *303*, 213.

- (124) Nam, Y. S.; Magyar, A. P.; Lee, D.; Kim, J.-W.; Yun, D. S.; Park, H.; Pollom, T. S.; Weitz, D. A.; Belcher, A. M. *Nat. Nanotechnol.* **2010**, *5*, 340.
- (125) Avery, K. N.; Schaak, J. E.; Schaak, R. E. *Chem. Mater.* **2009**, *21*, 2176.
- (126) Scholthof, K. G. *Annu. Rev. Phytopathol.* **2004**, *42*, 13.
- (127) Shaw, J. G. *Philos. Trans. R. Soc. Lond. B Biol. Sci.* **1999**, *354*, 603.
- (128) Beachy, R. N. *Philos. Trans. R. Soc. Lond. B Biol. Sci.* **1999**, *354*, 659.
- (129) Culver, J. N. *Annu. Rev. Phytopathol.* **2002**, *40*, 287.
- (130) Stubbs, G. *Semin. Virol.* **1990**, *1*, 405.
- (131) Namba, K.; Stubbs, G. *Science* **1986**, *231*, 1401.
- (132) Zaitlin, M. *AAB Descriptions of Plant Viruses* **2000**, 370.
- (133) R. N. Perham, T. M. W. *Virology* **1978**, *84*, 293.
- (134) Turpen, T. H.; Reinl, S. J.; Charoenvit, Y.; Hoffman, S. L.; Fallarme, V.; Grill, L. K. *Biotechnol.* **1995**, *13*, 53.
- (135) W. O. Dawson, D. L. B., D. A. Knorr, G. L. Grantham *Proc. Nat. Acad. Sci. U.S.A.* **1986**, *83*, 1832.
- (136) W.O. Dawson, P. B., G.L. Grantham. *Phytopathology* **1988**, *78*, 783.
- (137) Carl M. Deom, M. J. O., Rogern N. Beachy. *Science* **1987**, *237*, 389.
- (138) Schlick, T. L.; Ding, Z.; Kovacs, E. W.; Francis, M. B. *J. Am. Chem. Soc.* **2005**, *127*, 3718.
- (139) Miller, R. A.; Presley, A. D.; Francis, M. B. *J. Am. Chem. Soc.* **2007**, *129*, 3104.

- (140) Knez, M.; Bittner, A. M.; Boes, F.; Wege, C.; Jeske, H.; Maiß, E.; Kern, K. *Nano Lett.* **2003**, *3* 1079.
- (141) Dujardin, E.; Peet, C.; Stubbs, G.; Culver, J. N.; Mann, S. *Nano Lett.* **2003**, *3*, 413.
- (142) Tseng, R. J.; Tsai, C.; Ma, L.; Ouyang, J.; Ozkan, C. S.; Yang, Y. *Nat. Nanotechnol.* **2006**, *1*, 72.
- (143) Knez, M.; Sumser, M.; Bittner, A. M.; Wege, C.; Jeske, H.; Martin, T. P.; Kern, K. *Adv. Funct. Mater.* **2004**, *14* 116.
- (144) Shenton, W.; Douglas, T.; Young, M.; Stubbs, G.; Mann, S. *Adv. Mater.* **1999**, *11*, 253.
- (145) Lee, B.; Lo, C.; Thiagarajan, P.; Winans, R. E.; Li, X.; Niu, Z.; Wang, Q. *Langmuir* **2007**, *23*, 11157.
- (146) Britt, D. W.; Buijs, J.; Hlady, V. *Thin Solid Films* **1998**, *327-329*, 824.
- (147) Knez, M.; Sumser, M. P.; Bittner, A. M.; Wege, C.; Jeske, H.; Hoffmann, D. M. P.; Kuhnke, K.; Kern, K. *Langmuir* **2003**, *20*, 441.
- (148) He, J.; Niu, Z.; Tangirala, R.; Wang, J.-Y.; Wei, X.; Kaur, G.; Wang, Q.; Jutz, G.; Bker, A.; Lee, B.; Pingali, S. V.; Thiagarajan, P.; Emrick, T.; Russell, T. P. *Langmuir* **2009**, *25*, 4979.
- (149) Wargacki, S. P.; Pate, B.; Vaia, R. A. *Langmuir* **2008**, *24*, 5439.
- (150) Yang, L.; Wang, S.; Fukuto, M.; Checco, A.; Niu, Z.; Wang, Q. *Soft Matter* **2009**, *5*, 4951.
- (151) Lin, Y.; Su, Z.; Xiao, G.; Balizan, E.; Kaur, G.; Niu, Z.; Wang, Q. *Langmuir* **2011**, *27*, 1398.
- (152) Lin, Y.; Balizan, E.; Lee, L. A.; Niu, Z.; Wang, Q. *Angew. Chem. Int. Ed.* **2010**, *49*, 868.
- (153) Niu, Z.; Liu, J.; Lee, L. A.; Bruckman, M. A.; Zhao, D.; Koley, G.; Wang, Q. *Nano Lett.* **2007**, *7*, 3729.

- (154) Bruckman, M.; Niu, Z.; Li, S.; Lee, L.; Nelson, T.; Lavigne, J.; Wang, Q.; Varazo, K. *NanoBioTechnol.* **2007**, *3*, 31.
- (155) Balci, S.; Bittner, A. M.; Hahn, K.; Scheu, C.; Knez, M.; Kadri, A.; Wege, C.; Jeske, H.; Kern, K. *Electrochim. Acta* **2006**, *51*, 6251.
- (156) Lim, J.-S.; Kim, S.-M.; Lee, S.-Y.; Stach, E. A.; Culver, J. N.; Harris, M. T. *J. Colloid Interface Sci.* **2010**, *342*, 455.
- (157) Lee, S. Y.; Choi, J.; Royston, E.; B.Janes, D.; N.Culver, J.; Harris, M. T. *J. Nanosci. Nanotechnol.* **2006**, *6*, 974.
- (158) Manocchi, A. K.; Horelik, N. E.; Lee, B.; Yi, H. *Langmuir* **2010**, *26*, 3670.
- (159) Lim, J.-S.; Kim, S.-M.; Lee, S.-Y.; Stach, E. A.; Culver, J. N.; Harris, M. T. *Nano Lett.* **2010**, *10*, 3863.
- (160) Manocchi, A. K.; Seifert, S.; Lee, B.; Yi, H. *Langmuir* **2010**, *26*, 7516.
- (161) Royston, E.; Lee, S.-Y.; Culver, J. N.; Harris, M. T. *J. Colloid Interface Sci.* **2006**, *298*, 706.
- (162) Royston, E. S.; Brown, A. D.; Harris, M. T.; Culver, J. N. *J. Colloid Interface Sci.* **2009**, *332*, 402.
- (163) Z. Varpness, J. W. P., M. Young, T. Douglas. *Nano Lett.* **2005**, *5*, 2306.
- (164) Neltner, B.; Peddie, B.; Xu, A.; Doenlen, W.; Durand, K.; Yun, D. S.; Speakman, S.; Peterson, A.; Belcher, A. *ACS Nano* **2010**, *4*, 3227.
- (165) Paul R. Wittbrodt, C. D. P. *Eur. J. Soil Sci.* **1996**, *47*, 151.
- (166) Armor, J. N. *Appl. Catal., B* **1992**, *1*, 221.
- (167) Pirkanniemi, K.; Sillanpää, M. *Chemosphere* **2002**, *48*, 1047.
- (168) Wang, L. K.; Hung, Y. T.; Lo, H. H.; Yapijakis, C. *Waste Treatment in the Process Industries*; CRC press, 2006.

- (169) Centi, G. *J. Mol. Catal. A: Chem.* **2001**, *173*, 287.
- (170) Yin Li, M. A. E.-S. *J. Phys. Chem. B* **2001**, *105* 8938.
- (171) H. Hirai, H. W., M. Komiyama. *Chem. Lett.* **1983**, *12*, 1047.
- (172) Young, M.; Willits, D.; Uchida, M.; Douglas, T. *Annu. Rev. Phytopathol.* **2008**, *46* 361.
- (173) Huang, Y.; Chiang, C. Y.; Lee, S. K.; Gao, Y.; Hu, v. L.; Yoreo, J. D.; Belcher, A. M. *Nano Lett.* **2005**, *5*, 1429.
- (174) Blum, A. S.; Soto, C. M.; Wilson, C. D.; Cole, J. D.; Kim, M.; Gnade, B.; Chatterji, A.; Ochoa, W. F.; Lin, T.; Johnson, J. E.; Ratna, B. R. *Nano Lett.* **2004**, *4*, 867.
- (175) Douglas, T.; Strable, E.; Willits, D.; Aitouchen, A.; Libera, M.; Young, M. *Adv. Mater.* **2002**, *14*, 415.
- (176) P. Jonathan, G. B. *J. Gen. Virol.* **1984**, *65*, 253.
- (177) Hwang, D. J.; Roberts, I. M.; Wilson, T. M. *Proc. Nat. Acad. Sci. U.S.A.* **1994** *91*, 9067.
- (178) Yi, H.; Nisar, S.; Lee, S.; Powers, M. A.; Bentley, W. E.; Payne, G. F.; Ghodssi, R.; Rubloff, G. W.; Harris, M. T.; Culver, J. N. *Nano Lett.* **2005**, *5* 1931.
- (179) Yi, H.; Rubloff, G. W.; Culver, J. N. *Langmuir* **2007**, *23*, 2663.
- (180) Tan, W.; Lewis, C. L.; Horelik, N. E.; Pregibon, D. C.; Doyle, P. S.; Yi, H. *Langmuir* **2008**, *24*, 12483.
- (181) E F Pettersen, T. D. G., C C Huang, G S Couch, D M Greenblatt, E C Meng, T E Ferrin. *J. Comput. Chem.* **2004**, *25*, 1605.
- (182) K. Namba, R. P., G. Stubbs. *J. Molec. Biol.* **1989**, *208*, 307.
- (183) T. N. Bhat, P. B., Z. Feng, G. Gilliland, S. Jain, V. Ravichandran, B. Schneider, K. Schneider, N. Thanki, H. Weissig, J. Westbrook, H. M. Berman. *Nucleic Acids Res.* **2001**, *29*, 214.

- (184) Vincent, T.; Guibal, E. *Ind. Eng. Chem. Res.* **2002**, *41*, 5158.
- (185) Drygin, Y. F.; Bordunova, O. A.; Gallyamov, M. O.; Yaminsky, I. V. *FEBS Lett.* **1998**, *425*, 217.
- (186) Guinier, A.; Fournet, G. *Small Angle Scattering of X-rays*; John Wiley and Sons: New York, 1955.
- (187) Roe, R. J. *Methods of X-ray and neutron scattering in polymer science*; Oxford University: New York, 2000.
- (188) Jemian, P. R.; Weertman, J. R.; Long, G. G.; Spal, R. D. *Acta Metall. Mater.* **1991**, *39*, 2477.
- (189) Venezia, A. M.; Liotta, L. F.; Pantaleo, G.; La Parola, V.; Deganello, G.; Beck, A.; Koppány, Z.; Frey, K.; Horváth, D.; Guczi, L. *Appl. Catal., A* **2003**, *251*, 359.
- (190) Lee, B.; Lo, C.; Thiagarajan, P.; Lee, D. R.; Niu, Z.; Wang, Q. J. *Appl. Crystallogr.* **2008**, *41*, 134.
- (191) Levenspiel, O. *Chemical Reaction Engineering*; Wiley; 3 edition, 1998.
- (192) Ruthven, D. M.; Upadhye, R. S. *J. Catal.* **1971**, *21*, 39.
- (193) Xu, C.; Goodman, D. W. *J. Phys. Chem.* **1996**, *100*, 245.
- (194) Tedsree, K.; Li, T.; Jones, S.; Chan, C. W. A.; Yu, K. M. K.; Bagot, P. A. J.; Marquis, E. A.; Smith, G. D. W.; Tsang, S. C. E. *Nat. Nanotechnol.* **2011**, *6*, 302.
- (195) Larsen, R.; Ha, S.; Zakzeski, J.; Masel, R. I. *J. Power Sources* **2006**, *157*, 78.
- (196) Daneshvar, N.; Salari, D.; Aber, S. *J. Hazard. Mater.* **2002**, *94*, 49.
- (197) Kieber, R. J.; Xianliang, Z.; Mopper, K. *Limnol. Oceanogr.* **1990**, *35*, 1503.
- (198) Xu, X.-R.; Li, H.-B.; Gu, J.-D.; Li, X.-Y. *Environ. Toxicol. Chem.* **2005**, *24*, 1310.

- (199) Wittbrodt, P. R.; Palmer, C. D. *Environ. Sci. Technol.* **1996**, *30*, 2470.
- (200) Wittbrodt, P. R.; Palmer, C. D. *Environ. Sci. Technol.* **1995**, *29*, 255.
- (201) Geng, B.; Jin, Z.; Li, T.; Qi, X. *Chemosphere* **2009**, *75*, 825.
- (202) Yang, C.; Yi, H. *Biochem. Eng. J.* **2010**, *52*, 160.
- (203) Yang, C.; Manocchi, A. K.; Lee, B.; Yi, H. *Appl. Catal., B* **2010**, *93*, 282.
- (204) Zhou, W.; Lee, J. Y. *J. Phys. Chem. C* **2008**, *112*, 3789.
- (205) Zhou, W. P.; Lewera, A.; Larsen, R.; Masel, R. I.; Bagus, P. S.; Wieckowski, A. *J. Phys. Chem. B* **2006**, *110*, 13393.
- (206) Hoshi, N.; Kida, K.; Nakamura, M.; Nakada, M.; Osada, K. *J. Phys. Chem. B* **2006**, *110*, 12480.
- (207) Silvestre-Albero, J.; Rupprechter, G.; Freund, H.-J. *J. Catal.* **2006**, *240*, 58.
- (208) Jung, G. Y.; Stephanopoulos, G. *Science* **2004**, *304*, 428.
- (209) Lewandowski, A. T.; Bentley, W. E.; Yi, H.; Rubloff, G. W.; Payne, G. F.; Ghodssi, R. *Biotechnol. Progr.* **2008**, *24*, 1042.
- (210) Sahoo, H. R.; Kralj, J. G.; Jensen, K. F. *Angew. Chem. Int. Ed.* **2007**, *46*, 5704.
- (211) Hwang, S.; Kwon, O. J.; Kim, J. J. *Appl. Catal., A* **2007**, *316*, 83.
- (212) Kim, T.; Kwon, S. *J. Micromech. Microeng.* **2006**, *16*, 1760.
- (213) Yi, H.; Wu, L.; Ghodssi, R.; Rubloff, G. W.; Payne, G. F.; Bentley, W. E. *Anal. Chem.* **2004**, *76*, 365.
- (214) Kane, R. S.; Takayama, S.; Ostuni, E.; Ingber, D. E.; Whitesides, G. M. *Biomater.* **1999**, *20*, 2363.
- (215) Calvert, P. *Chem. Mater.* **2001**, *13*, 3299.

- (216) Sirringhaus, H.; Kawase, T.; Friend, R. H.; Shimoda, T.; Inbasekaran, M.; Wu, W.; Woo, E. P. *Science* **2000**, *290*, 2123.
- (217) Ago, H.; Murata, K.; Yumura, M.; Yotani, J.; Uemura, S. *Appl. Phys. Lett.* **2003**, *82*, 811.
- (218) Piner, R. D.; Zhu, J.; Xu, F.; Hong, S.; Mirkin, C. A. *Science* **1999**, *283*, 661.
- (219) Lee, K. B.; Park, S. J.; Mirkin, C. A.; Smith, J. C.; Mrksich, M. *Science* **2002**, *295*, 1702.
- (220) Reetz, M. T.; Westermann, E. *Angew. Chem. Int. Ed.* **2000**, *39*, 165.
- (221) Sakurai, H.; Tsukuda, T.; Hirao, T. *J. Org. Chem.* **2002**, *67*, 2721.
- (222) LeBlond, C. R.; Andrews, A. T.; Sun, Y.; Sowa, J. R. *Org. Lett.* **2001**, *3*, 1555.
- (223) Xu, Z.; Mao, J.; Zhang, Y. *Catal. Commun.* **2008**, *9*, 97.
- (224) Lakmini, H.; Ciofini, I.; Jutand, A.; Amatore, C.; Adamo, C. *J. Phys. Chem. A* **2008**, *112*, 12896.
- (225) Carrettin, S.; Guzman, J.; Corma, A. *Angew. Chem. Int. Ed.* **2005**, *44*, 2242.
- (226) Littke, A. F.; Fu, G. C. *Angew. Chem. Int. Ed.* **2002**, *41*, 4176.
- (227) Leadbeater, N. E.; Williams, V. A.; Barnard, T. M.; Collins, M. J. *Org. Process Res. Dev.* **2006**, *10*, 833.
- (228) Arvela, R. K.; Leadbeater, N. E.; Sangi, M. S.; Williams, V. A.; Granados, P.; Singer, R. D. *J. Org. Chem.* **2004**, *70*, 161.
- (229) Conlon, D.; Pipik, B.; Ferdinand, S.; LeBlond, C.; Sowa, J.; Izzo, B.; Collins, P.; Ho, G. J.; Williams, J.; Shi, Y. J.; Sun, Y. *Adv. Synth. Catal.* **2003**, *345*, 931.
- (230) Gaikwad, A.; Holuigue, A.; Thathagar, M.; Elshof, J.; Rothenberg, G. *Chem. Eur. J.* **2007**, *13*, 6908.

- (231) Simeone, J. P.; Sowa Jr, J. R. *Tetrahedron* **2007**, *63*, 12646.
- (232) Hutchings, G. J. *Chem. Commun.* **2008**, *10*, 1148.
- (233) Zhang, W. *J. Nanopart. Res.* **2003**, *5*, 323.
- (234) Kramer, R. M.; Li, C.; Carter, D. C.; Stone, M. O.; Naik, R. R. *J. Am. Chem. Soc.* **2004**, *126*, 13282.
- (235) Douglas, T.; Stark, V. T. *Inorg. Chem.* **2000**, *39*, 1828.
- (236) Manocchi, A. K.; Seifert, S.; Lee, B.; Yi, H. *Langmuir* **2011**, *27*, 7052.
- (237) Lim, J. S.; Kim, S. M.; Lee, S. Y.; Stach, E. A.; Culver, J. N.; Harris, M. T. *J. Nanomater.* **2010**, doi:10.1155/2010/620505.
- (238) Yang, C.; Manocchi, A. K.; Lee, B.; Yi, H. *J. Mater. Chem.* **2011**, *21*, 187.
- (239) Lim, J.-S.; Kim, S.-M.; Lee, S.-Y.; Stach, E. A.; Culver, J. N.; Harris, M. T. *J. Colloid Interface Sci.* **2011**, *356*, 31.
- (240) Shakeri, M.; Tai, C. W.; Gothelid, E.; Oscarsson, S.; Backvall, J. E. *Chemistry* **2011**, *17*, 13269.
- (241) Wang, Y.; Yan, R.; Zhang, J.; Zhang, W. *J. Mol. Catal. A: Chem.* **2010**, *317*, 81.
- (242) Cruise, G. M.; Scharp, D. S.; Hubbell, J. A. *Biomater.* **1998**, *19*, 1287.
- (243) Tong, L.; Righini, M.; Gonzalez, M. U.; Quidant, R.; Kall, M. *Lab Chip* **2009**, *9*, 193.
- (244) Wang, H.-F.; Kaden, W. E.; Dowler, R.; Sterrer, M.; Freund, H.-J. *PCCP* **2012**, *14*, 11525.
- (245) Lewis, C. L.; Choi, C.-H.; Lin, Y.; Lee, C.-S.; Yi, H. *Anal. Chem.* **2010**, *82*, 5851.

- (246) Perry, J. L.; Herlihy, K. P.; Napier, M. E.; Desimone, J. M. *Acc. Chem. Res.* **2011**, *44*, 990.
- (247) Xu, S.; Nie, Z.; Seo, M.; Lewis, P.; Kumacheva, E.; Stone, H. A.; Garstecki, P.; Weibel, D. B.; Gitlin, I.; Whitesides, G. M. *Angew. Chem. Int. Ed.* **2005**, *44*, 724.
- (248) Wu, Y.; Joseph, S.; Aluru, N. R. *J. Phys. Chem. B* **2009**, *113*, 3512.
- (249) Amsden, B. *Macromolecules* **1998**, *31*, 8382.
- (250) Engberg, K.; Frank, C. W. *Biomed. Mater.* **2011**, *6*, 26.
- (251) Lee, W.; Cho, N.-J.; Xiong, A.; Glenn, J. S.; Frank, C. W. *Proc. Nat. Acad. Sci. U.S.A.* **2010**, *107*, 20709.